



University of
Nottingham
UK | CHINA | MALAYSIA

The Cosmic Chemical Evolution Histories of Spiral Galaxies

Michael John Greener



Thesis submitted to the University of Nottingham
for the degree of Doctor of Philosophy

June 2022

*To win is not important.
To be successful is not even important.
How to plan and prepare is crucial.
When you prepare very well – when you plan very well –
then success can come your way.
Then winning can come your way.*

– Eliud Kipchoge, during his address to the Oxford Union Society in 2017.

Supervisors: Prof. Alfonso Aragón-Salamanca
Prof. Michael Merrifield

Examiners: Dr. Anne-Marie Weijmans (University of St Andrews)
Dr. Simon Dye (University of Nottingham)

Submitted: 15 June 2022
Examined: 7 July 2022
Final version: 27 July 2022

Contents

Abstract	v
Acknowledgements	vii
Published Work	ix
1 Introduction	1
1.1 Galaxies	1
1.1.1 A Brief History of Galaxy Morphology	2
1.1.2 Spiral Galaxies	4
1.2 Baryonic Components of Spiral Galaxies	7
1.2.1 Stars	7
1.2.2 Interstellar Gas	9
1.2.3 Interstellar Dust	11
1.3 Chemical Compositions of Galaxies	15
1.3.1 Metallicities	15
1.3.2 Linking Metallicities with other Physical Properties	17
1.3.3 The Astrophysics of Chemical Evolution	21
1.4 Structure of this Thesis	24
2 Observational Data and Technical Analysis	25
2.1 SDSS-IV MaNGA	25
2.1.1 Instrumentation	26
2.1.1.1 The Sloan Telescope at APO	27
2.1.1.2 The BOSS Optical Spectrographs	28

2.1.1.3	The MaNGA IFU Fibre Feed System	28
2.1.2	The Complete MaNGA Sample	30
2.1.3	The Data Reduction Pipeline	33
2.1.3.1	Sky Subtraction	33
2.1.3.2	Spectrophotometric Calibration	34
2.1.3.3	DRP Datacubes	35
2.1.4	The Data Analysis Pipeline	36
2.2	Sample Selection of MaNGA Galaxies	37
2.2.1	Galaxy Zoo 2	38
2.2.2	Galaxy Zoo: 3D	39
2.3	Full-Spectrum Stellar Population Fitting	41
2.3.1	Why STARLIGHT?	41
2.3.2	Spectral Fitting with STARLIGHT	42
2.3.3	Tests and Improvements	45
2.4	Applications of MaNGA Data in this Work	47
3	Spatially Resolved Dust Attenuation in Spiral Galaxies	48
3.1	Introduction	48
3.2	Sample Selection	51
3.3	Measures of Dust Attenuation	51
3.3.1	Emission Line Ratios	51
3.3.1.1	BPT Diagrams	52
3.3.1.2	Utilising the Balmer Decrement	53
3.3.2	Stellar Population Modelling	54
3.4	Categorising Galaxies by Global Properties	56
3.5	Global Dust Attenuation Measurements	59
3.6	Spatially Resolved Dust Attenuation	63
3.6.1	Spiral Arm and Inter-Arm Regions	63
3.6.2	Radial Dependence on Stellar Mass	64
3.6.3	Radial Dependence on Relative Global sSFR	67
3.6.4	Investigating Local Variations in Dust Attenuation	69

3.7	The Geometry of Dust in Star-Forming Spiral Galaxies	73
3.8	Conclusions	76
4	The “G-Dwarf Problem” Revisited	78
4.1	Introduction	78
4.2	Sample Selection	81
4.3	Spectral Fitting	81
4.4	Results and Discussion	82
5	The Chemical Co-Evolution of Gas and Stars in Spiral Galaxies	85
5.1	Introduction	85
5.2	Sample Selection	88
5.3	Metallicities	88
5.3.1	Stellar Metallicities	88
5.3.2	Gas Metallicities	92
5.3.2.1	Emission Lines	92
5.3.2.2	The Fundamental Metallicity Relation	94
5.4	Results and Discussion	96
5.4.1	Evolution of the Mass–Metallicity Relations	96
5.4.2	How does Stellar Mass Affect Metallicity Evolution?	100
5.5	Conclusions	103
6	Conclusions and Future Work	105
6.1	Dust Attenuation in Spiral Galaxies	105
6.2	Chemical Evolution of Galaxies	107
6.2.1	Resolving the G-Dwarf Problem Outside the Milky Way	107
6.2.2	The Evolution of Chemical Compositions with Cosmic Time	108
6.3	Future Work	109
	Bibliography	112

Abstract

Spiral galaxies have always been of particular interest to astronomers ever since it was discovered that our own galaxy, the Milky Way, is itself a spiral. Although long-slit spectroscopy of galaxies has been available for over half a century, the recent advent of large-scale integral field unit surveys such as SDSS-IV MaNGA means that spatially resolved spectroscopic observations are now available for thousands of nearby spiral galaxies. In this thesis, we will use data from the MaNGA survey to investigate the fundamental properties and the chemical evolution of spiral galaxies.

We begin with an investigation into the spatially resolved dust attenuation of a well-defined sample of star-forming spiral galaxies observed by MaNGA. By making use of software which allows the integrated spectrum of a galaxy to be decomposed into stellar population spectra of single ages and stellar metallicities, we are able to obtain spatially resolved measures of the dust attenuation affecting the stellar populations of the spirals. We compare these measurements with those obtained for the dust attenuation in the gas for the same galaxies, which we derive from analysing emission lines in the galactic spectra. Analysis of the radial profiles of the two dust attenuation measures suggests that there is a disproportionately high concentration of giant molecular clouds (incorporating gas, young stars and clumpy dust) nearer to the centres of star-forming spiral galaxies.

We then turn our attention to the main question that this thesis aims to answer: How do the chemical compositions of spiral galaxies change over cosmic time? In order to address this question, we first analyse the stellar metallicity distributions of a large sample of MaNGA galaxies, with a view to addressing the “G-dwarf problem”, which essentially states that the small number of low-metallicity G-dwarf stars observed in the Milky Way is inconsistent with the simplest picture of the Galaxy forming from a “closed box” of gas. We can resolve the G-dwarf problem by treating the Galaxy as an open system that accretes gas throughout its life. This observation has classically only been made in the Milky Way, but the availability of high-quality spectral data from MaNGA and the development of new analysis techniques mean that we can now make equivalent measurements for a large sample of spiral galaxies. Our analysis shows that high-mass spirals generically show a similar deficit of low-metallicity stars, implying that the Milky Way’s history of gas accretion is common. By contrast, low-mass spirals show little sign of a G-dwarf problem, presenting the metallicity distribution that would be expected if such systems evolved as pretty much closed boxes.

Following on from this research, we investigate archaeologically how the metallicity in both stellar and gaseous components of a similar sample of spiral galaxies of differing masses evolve with time. In particular, we analyse how the metallicity of these systems has changed over the last 10 billion years since “cosmic noon”. We find that the chemical evolution of a given galaxy depends on its stel-

lar mass: low-mass galaxies, which behave as pretty much closed boxes, are found to steadily increase both their stellar and gas metallicities over cosmic time; however, in high-mass galaxies, which behave as accreting boxes, the gas metallicity is found to increase over cosmic time (albeit less dramatically than in their low-mass counterparts), but we find that the metallicity of the stars may actually be lower at later times. Such disjoint behaviour is what we might expect if these more massive systems have accreted significant amounts of largely pristine gas over their lifetimes, and this material has not been well mixed into the galaxies.

While we do ultimately answer the question posed at the beginning of this thesis, further considerations can of course be taken into account that we do not address in this work. At any rate, the studies presented in this thesis illustrate the strengths of large-scale integral field unit surveys, which have provided us with new and powerful tools for studying the chemical evolution of galaxies.

Acknowledgements

None of this work would have been remotely possible without the help and patience of a great number of people.

I am incredibly grateful to both Alfonso and Mike. You have been patient, encouraging, and understanding since my very first day in CAPT, and have never let any of these qualities waver throughout my PhD. It was so nice to be able to drop into both of your offices to talk through something I might be stuck on, discuss the interpretation of a result that I had found, or just to eagerly show you an exciting plot that simply couldn't wait until our Friday meeting. In particular, I must thank Alfonso for his incredible dedication to ensure that I passed my MPAGS resit with flying colours. I am still, frankly, in awe of the depth of your knowledge in so many disparate fields, and your willingness to share that knowledge with others.

I was in a very fortunate position to have not just two, but effectively four supervisors when I joined Nottingham. Tom and Amelia, you will never know how many hours you saved me at the start of my PhD getting to grips with MaNGA data. You turned what might have been a long and frustrating start to research be genuinely enjoyable, and I can't thank you enough for that. Thanks also for fielding endless questions I considered too dumb to take to Alfonso and Mike, thanks for proof-reading and contributing to my papers, thanks for helping me with conference talks, and thanks above all for being genuinely lovely people to work and spend time with. I have missed you tremendously since you have both moved on to bigger and better things.

I would be remiss at this point if I did not acknowledge the co-founders of the Dunkirk Arms (DA): Jacob, Roan, and Liza. What can I say except thanks for putting up with me for three years. While I question your choice in housemates, I wouldn't change our friendships for anything and I can't quite explain how much better you have made what could otherwise have been a very average last three years. Tonight on Bo'om Gear: I thank **B**aresca, for being able to make me laugh only via the power of horbly blongers; I thank **R**oan, for screeching with me at all hours of the day; and I thank **L**iza, for normalising not working and playing Hospital Hospital while I watched the Euros. Seriously, I'm going to miss you all.

Thanks to everyone in Nottingham who came to see me, went running with me, or came to the DA for a massive party when things were getting a bit too boring. Adam, Alex, Ben (the goodest boi), Brossingtons, Cha, Chetan, Dan, Emma, Finlay, Fitzgerald, Harrison, Helena, Ieuan (and Logan and Misty), Jack (rest in piece good boi), Jéssica, Karel, Kellie de Boss, Leo (my vegan prince <3), Lizzie, Marcus, Matt, Max, Meg, Mei, Rowann, Sam "Defender of Beeston" Booth, Shaun, Simon Fearn, Simon Woodward, Steph, Sunny, Sukhi (m'memelord), Svenja, Tom Clarke, Tomáš, Ulli, Will, Yolande, Zac, and especially BOB. You all mean more to me than I can possibly say, and I'm lucky to have all of you as friends.

Thank you especially to Mum, Dad, Naomi, Joe, Nana, Grandad, Mama Cat (MC), and Pepper. You are the best family anyone could wish for. Thanks for always taking an interest in my work (which is admittedly not always the most interesting!), for keeping me constantly entertained (both over WhatsApp and in real life), and for always believing in me. This thesis is for you, fam.

Finally, thank you CB. You mean the world to me and I could not have done this without you. You'll always need someone to annoy you when you visit another planet, after all.

Published Works

Almost all of the content in this thesis has already been published in the following three works:

- I **Greener M. J.**, Aragón-Salamanca A., Merrifield M. R., Peterken T. G., Fraser-McKelvie A., Masters K. L., Krawczyk C. M., Boardman N. F., Boquien M., Andrews B. H., Brinkmann J., Drory N., 2020. *SDSS-IV MaNGA: spatially resolved dust attenuation in spiral galaxies*. Monthly Notices of the Royal Astronomical Society, 495, 2, 2305–2320.
- II **Greener M. J.**, Merrifield M., Aragón-Salamanca A., Peterken T., Andrews B., Lane R. R., 2021. *SDSS-IV MaNGA: the “G-dwarf problem” revisited*. Monthly Notices of the Royal Astronomical Society, 502, 1, L95–L98.
- III **Greener M. J.**, Aragón-Salamanca A., Merrifield M., Peterken T., Sazonova E., Haggard R., Bizyaev D., Brownstein J. R., Lane R. R., Pan K., 2022. *SDSS-IV MaNGA: the chemical co-evolution of gas and stars in spiral galaxies*. Monthly Notices of the Royal Astronomical Society, *submitted*.

Chapter 3 is based on material published in Paper I, Chapter 4 is based on Paper II, and Chapter 5 is based on Paper III.

The vast majority of the work presented in this thesis was carried out by the author, with supplementary advice from various co-authors listed above. In any instances where the work includes the product of larger collaborations, this is explicitly mentioned in the relevant Chapter.

Chapter 1

Introduction

The ultimate aim of this thesis is to try and better understand the chemical evolution histories of spiral galaxies. Specifically, we wish to answer the question of how the chemical compositions of spiral galaxies change over cosmic time. Therefore, we need to first identify what exactly we mean by spiral galaxies, as well as understanding the interplay between the gas, stars, and dust that comprise these systems. Only after laying down this groundwork can we properly investigate their chemical compositions, and, in turn, their chemical evolution histories.

This Section is hence structured as follows. Section 1.1 gives a brief overview of galaxies in general, and spiral galaxies in particular. In Section 1.2, we review the three baryonic components of spiral galaxies that we are interested in studying – i.e, stars, interstellar gas and interstellar dust. In Section 1.3 we discuss the chemical compositions of galaxies, which will be salient for the work we carry out in Chapters 4 and 5. Finally, Section 1.4 outlines the overall structure of this thesis.

1.1 Galaxies

It is crucial for astronomers to understand galaxies in general before we further investigate how these systems – and the stars, gas, and interstellar dust that they contain – evolve with cosmic time. In the words of Beatrice Tinsley:

‘Essentially everything of astronomical interest is either part of a galaxy, or from a galaxy, or otherwise relevant to the origin or evolution of galaxies.’

– Tinsley (1980).

Apart from a handful of systems visible to the naked eye (such as the Andromeda Galaxy, the Large and Small Magellanic Clouds, and the Triangulum Galaxy), genuine observations of extragalactic astronomical objects were not made until Charles Messier published his catalogue of nebulae (Messier, 1781). However, it would not be conclusively proved that some of these catalogued “nebulae” were in fact galaxies – similar to, but outside of – our own Milky Way until over a century later. Thanks to Doppler shift measurements made of these nebulae by Slipher (1913) – in conjunction with the crucial distance measurements to Cepheid variable stars in both the Milky Way and the Small Magellanic Cloud made by Leavitt (1908, 1912) – Hubble (1925, 1926) was able to definitively prove that these nebulae could not be Galactic in origin; instead, they were galaxies of their own, external to the Milky Way. Thus the field of extragalactic astronomy was born.

Immediate research on the subject involved classifying galaxies into distinct morphological types; we give an overview of these efforts in Section 1.1.1. However, since in this thesis our investigations extend only to the subclass of galaxies known as “spirals”, we give a detailed description of the structure and compositions of such systems in Section 1.1.2.

1.1.1 A Brief History of Galaxy Morphology

Morphological differences between nebulae had been noted long before it was known that such objects were extragalactic in origin. The Third Earl of Rosse was the first to remark that certain nebulae, such as the Messier object M51, exhibited a spiral structure (Parsons, 1850). Subsequent efforts to classify galaxies into distinct categories based on their morphologies (in particular by Wolf, 1908 and Lundmark, 1926) were eventually formalised by Hubble (1936) in his now famous “tuning fork” diagram (see also the later revisions made by Sandage, 1961). The so-called Hubble sequence (a more modern form of which is shown in Figure 1.1; Kormendy & Bender, 1996), consists of two main morphological classes: elliptical and spiral galaxies.

Elliptical galaxies exhibit smooth, featureless distributions of redder stars and show few signs of internal structure, although globular clusters may be resolved in nearby ellipticals. Hubble (1936) arranged such galaxies in a sequence from E0 (which have almost completely spherical morphologies) to E7 galaxies (which are highly ellipsoidal in shape).

Spiral galaxies earn their names from the twisting arms which emanate from a central nuclear bulge. Young, blue stars, gas, and dust are prevalent in their spiral arms – indicating that star formation is ongoing in these features – whereas the bulges of spirals are redder in colour and more akin to elliptical galaxies. In the Hubble sequence, spirals are subdivided into two further categories, depending

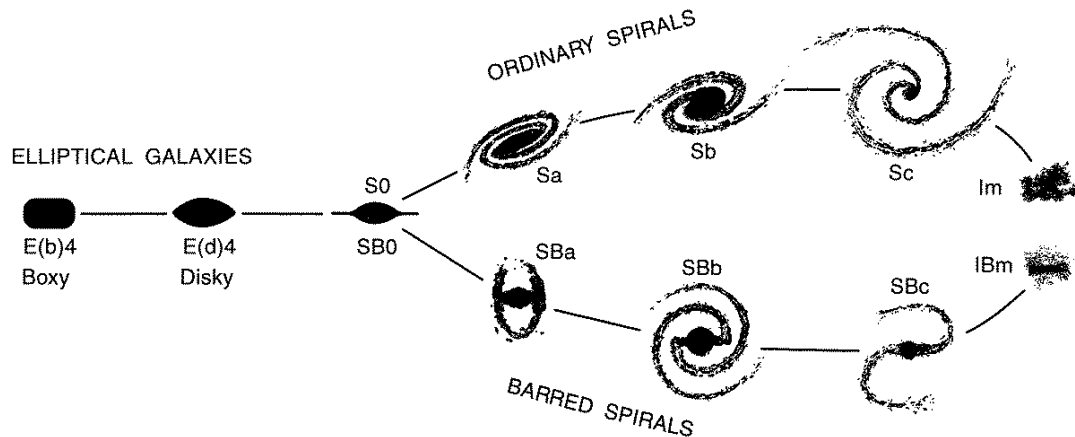


Figure 1.1: A more modern form of the tuning fork diagram, originally proposed by Hubble (1936), used to classify galaxies into different morphological types. Im galaxies are a subclass of Irr I galaxies without any spiral structure; they are distinct from “Magellanic irregular” or IBm galaxies, which exhibit some bar structure. Figure taken from Kormendy & Bender (1996, Figure 1).

on whether or not these galaxies exhibit a bar at their centres (as seen in Figure 1.1; Kormendy & Bender, 1996). Both ordinary and barred spirals range from S(B)a (with large bulges and tightly wound arms) to S(B)c galaxies (which have small bulges and open arms). Spiral galaxies will be discussed in greater detail in Section 1.1.2.

At the juncture between elliptical and spiral galaxies, Hubble (1936) placed the lenticular (S0) galaxies. While lenticular galaxies exhibit disk structure and a bright central bulge, they lack the spiral arms (and the associated young stars and gas) of their spiral counterparts. They may, however, still contain significant quantities of dust in their otherwise barren disks.

Systems which do not fall into any of the above categories of the Hubble sequence are classified as irregular galaxies. Like spiral galaxies, they often contain large proportions of young, blue stars, gas, and dust. However, they are devoid of any regular morphological structure. Hubble (1936) proposed two subclasses of irregular galaxies. Irr I galaxies exhibit some structure (though not quite enough to place these systems on the Hubble sequence), while Irr II galaxies do not exhibit any discernible structure whatsoever.

Though still in frequent use today, the Hubble sequence has various shortcomings due to the subjective nature of classifying galaxies in this manner (e.g. Mihalas & Binney, 1981; Naim et al., 1995). The orientation of an elliptical galaxy may well determine whether it is classified as E0 or E7, for instance. Similarly, an edge-on lenticular galaxy is almost indistinguishable from an edge-on spiral

galaxy. Recently, major issues have arisen in particular with the classification of spirals, since there is little or no correlation between the tightness of arm winding in spiral galaxies and the size of their nuclear bulges (e.g. Hart et al., 2017a, 2018; Masters et al., 2019).

As a result, improvements upon the original Hubble sequence, as well as entirely different classification schemes, have since been proposed by several authors. Most famously, revisions to the Hubble sequence have been made by de Vaucouleurs (1959, 1963), as well as by Kormendy & Bender (1996, 2012). More specifically, de Vaucouleurs (1959, 1963) added a third dimension to the Hubble sequence by distinguishing between “s” galaxies (whose spiral arms emanate from their centres) and “r” galaxies (whose arms sprout at a tangent to an inner ring). Subsequently, Kormendy & Bender (1996, 2012) suggested re-ordering elliptical galaxies in the Hubble sequence by how “boxy” or “disky” such galaxies appear, rather than by how ellipsoidal they appear (cf. Figure 1.1; Kormendy & Bender, 1996). Alternative classification systems have also been suggested. For instance, the trident-shaped scheme of van den Bergh (1960, 1976) splits disk galaxies into three distinct branches of lenticular, “anaemic”, and spiral galaxies; Elmegreen & Elmegreen (1987) classify spirals into 12 different types according to the number and length of their spiral arms; and the comb diagram of Cappellari et al. (2011a) considers whether elliptical and lenticular galaxies are either slow or fast rotators.

Nevertheless, since in this thesis we are only interested in studying the chemical evolution histories of spiral galaxies, it is sufficient for this work to use the classifications originally suggested by Hubble (1936) in order to define and study these galaxies. The natures and compositions of spiral galaxies will now be discussed in greater detail below.

1.1.2 Spiral Galaxies

The spiral structure of galaxies was first observed in the 19th century by Parsons (1850). Spiral galaxies were later divided into two subclasses, as discussed in Section 1.1.1: barred spirals were determined by Hubble (1936) to be morphologically distinct from ordinary spirals. Spiral galaxies of all kinds have always been of great intrigue and importance to astronomers, especially because it has been known for over a century that our own galaxy, the Milky Way, is itself a spiral galaxy (Easton, 1913). Exactly which subclass of spiral the Milky Way should be classified as has been the subject of intense debate; currently, it is thought to be a barred spiral galaxy (e.g. Oort et al., 1958; de Vaucouleurs, 1964; Benjamin et al., 2005). Nevertheless, the Milky Way has historically proved to be an excellent laboratory for testing general theories of spiral structure and evolution. Historical analyses of the chemical compositions of stars in the Milky Way are, for instance, crucial for the work that we undertake in Chapter 4.



Figure 1.2: The nearby spiral galaxy M74. Clearly visible is the yellowish nuclear bulge of older stars. The strikingly beautiful spiral structure is also apparent, within which we find clusters of younger blue stars, reddish H II regions, and dark dust lanes. *Image Credit: NASA, ESA, and the Hubble Heritage (STScI/AURA)-ESA/Hubble Collaboration.*

Spirals – like any other galaxy – are composed of four principal ingredients: stars, interstellar gas and dust, and dark matter. An exquisite example of the spiral galaxy M74 can be seen in Figure 1.2; in addition to the spiral structure, each of the three baryonic components (stars, gas, and dust) are clearly visible. The relative masses of these constituents play an integral role in the evolution of spiral galaxies. The overwhelming majority of any galaxy’s mass is due to the dark matter component: for instance, McMillan (2017) finds that only $\sim 4\%$ of the Milky Way’s mass is due to its stars. However, we do not investigate the dark matter component of spiral galaxies in this work. As such, any masses for galaxies quoted in this thesis will always refer only to stellar masses, unless otherwise stated. A general summary of the baryonic components of spiral galaxies (i.e. their stars, gas, and dust) is given in Section 1.2.

The simplest model for a spiral galaxy involves just two key structural components:

1. The disks of spiral galaxies are host to the most striking features of these systems. Young stars, gas, and dust extend outwards from the centres of these galaxies as pinwheel spiral arms. The arms of spiral galaxies are also typified by their bluer colours, indicative of younger stellar populations, as well as hot gas necessary to fuel star formation in these regions. As a result, the spiral arms of galaxies are associated with local regions of high star formation rates (SFRs; e.g. Toomre, 1977; Calzetti et al., 2005; González Delgado et al., 2017). Studies of nearby spirals – such as M31 (Walterbos & Kennicutt, 1988; Tempel et al., 2009), M33 (Humphreys & Sandage, 1980; Hippelein et al., 2003; Xilouris et al., 2012), M51 (Mathewson et al., 1972; Rix & Rieke, 1993; De Looze et al., 2014), M83 (Ondrechen, 1985; Foyle et al., 2012), and M101 (Israel et al., 1975; Suzuki et al., 2007) – show that long dust lanes are also associated with the spiral arms for each of these galaxies. The arms themselves are not believed to be physical structures, but density waves of the stars, gas, and dust that comprise the spiral arms (e.g. Mathewson et al., 1972; Rots, 1975; Tamburro et al., 2008; Egusa et al., 2009; Peterken et al., 2019b; Vallée, 2020).
2. The bulges of spiral galaxies, by contrast, more closely resemble elliptical galaxies and are dominated by older, redder stellar populations (e.g. Kormendy & Kennicutt, 2004; Minniti & Zoccali, 2008). Some authors, for instance Renzini (1999) and Kormendy & Kennicutt (2004), argue that the nuclear bulges of spiral galaxies may be directly modelled as elliptical galaxies, such is the similarity between the two objects.

Spiral galaxies may also be host to bars, which are protrusions from galactic bulges that are distinct from the spiral arms. It is thought that a majority of spiral galaxies exhibit bars (e.g. de Vaucouleurs, 1963; Sellwood & Wilkinson, 1993; Masters et al., 2011); these structures may both suppress and enhance star formation at the centres of their host galaxies (see, for instance, Fraser-McKelvie et al., 2020a). On the one hand, bars funnel gas away from the nuclear bulges of galaxies, starving the centres of these galaxies of fuel required for star formation, and enhancing the SFRs within the bars themselves (e.g. Sellwood & Wilkinson, 1993); on the other hand, greater SFRs have also been discovered in the centres of barred galaxies (e.g. Heckman, 1980; Knapen et al., 1995).

The complex interplay between the various features of spiral galaxies makes studying their baryonic ingredients (i.e. their stars, gas, and dust), and the chemical evolution of these components, a worthwhile pursuit. We shall now discuss each of these baryonic ingredients in greater detail. Finally, the importance of the Milky Way as a testing ground for theories of chemical evolution in other spiral galaxies cannot be emphasised enough; we shall revisit this laboratory in Chapter 4.

1.2 Baryonic Components of Spiral Galaxies

As mentioned in Section 1.1.2, there are three main baryonic components which comprise the overwhelming majority of (visible) material in spiral galaxies: stars, interstellar gas, and interstellar dust. A summary of each of these constituents, and their evolution over cosmic time, is given in turn in the following subsections.

1.2.1 Stars

The defining feature of any galaxy is, arguably, its stars. Thanks to observations made by Galileo in 1609, astronomers have long since known that there are many more stars present in the Milky Way than can be resolved by the naked eye. Over a century later in 1755, philosopher Immanuel Kant proposed the concept of ‘island Universes’, suggesting that some of the myriad fuzzy nebulae visible in the night sky may, in fact, be comprised of vast collections of individual stars. Subsequent observations, made by the likes of Herschel (1785) and Parsons (1850), would later confirm the validity of this theory. The study of stars in order to better understand the nature of the galaxies that they comprise has therefore been an important discipline ever since these observations were performed.

An excellent review of the formation and evolution of stars, and the consequences that these processes have upon the evolution of galaxies, is given by Tinsley (1980). A brief overview of some salient points will be provided here.

The evolution of stars is most easily understood with the aid of the Hertzsprung–Russell (HR) diagram (see Figure 1.3; Bertelli et al., 2008). Stars spend the majority ($\sim 90\%$) of their lifetimes on the main sequence fusing (or “burning”) hydrogen in their cores (e.g. Tinsley, 1980); their evolution off the main sequence is determined by their mass. We explore the post-main sequence evolution of stars – and the important influence that stellar mass has upon their fates – in greater detail below. A star’s mass also ultimately governs its main sequence lifetime, its spectral type, and its colour: high-mass stars are generally young and blue, while low-mass stars are, by contrast, usually older and redder. The colours of galaxies are determined in no small part by the colours of the populations they contain, meaning that spiral and irregular galaxies, which are typically gas-rich, generally contain a greater proportion of young, blue stars than their elliptical and lenticular counterparts, since such galaxies are typically gas-poor.

Since so many different stellar properties depend upon the mass of the star, a good understanding of the distribution of the initial masses of a population is of paramount importance if we wish to unravel the chemical evolution of galaxies. To this end, we turn to the initial mass function (IMF), $\xi(m)$, which allows the number of stars formed in the mass interval $(m, m + dm)$ and in the time interval

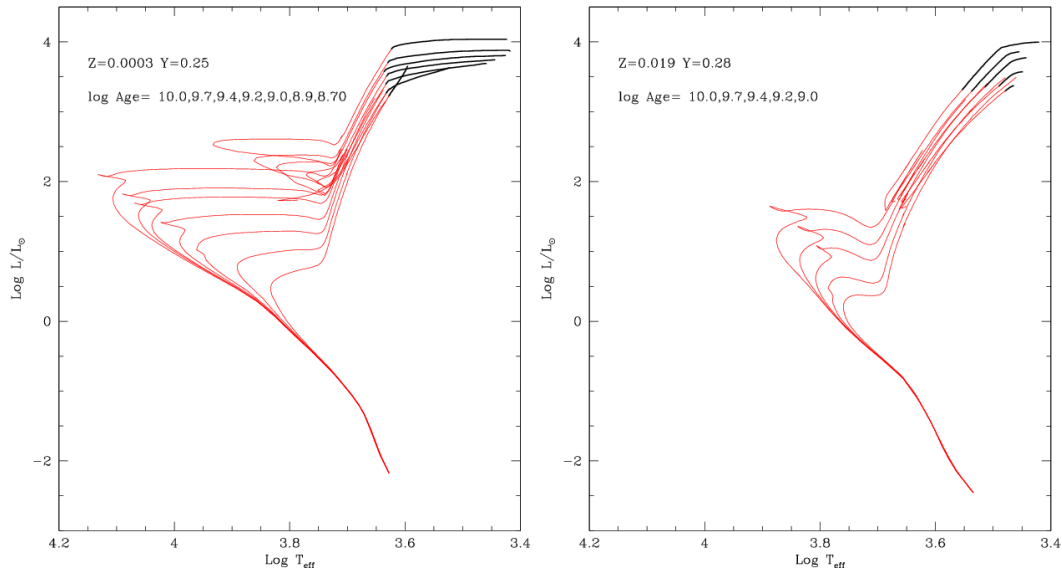


Figure 1.3: Theoretical HR diagrams showing evolutionary tracks (“isochrones”) for (left-hand plot) metal-poor stars and (right-hand plot) stars with approximately Solar composition at a range of different main sequence lifetimes (and therefore different masses) between (left) $10^{8.7}$ yr and $10^{10.0}$ yr; and (right) $10^{9.0}$ yr and $10^{10.0}$ yr. More massive stars peel off the main sequence at higher effective temperatures and luminosities. Figures taken from Bertelli et al. (2008, Figures 4 and 5).

($t, t + dt$) to be estimated, if the star-formation rate (SFR), $\psi(t)$, is also known (Schmidt, 1959, 1963). Various forms for the IMF have been proposed over the years: originally, Salpeter (1955) suggested that the IMF was a power law of the form $\xi(m) \propto m^{-\alpha}$, where α is a constant known as the slope of the IMF; however, subsequent authors have found that either a broken power law (e.g. Miller & Scalo, 1979; Kroupa, 2001) or a log-normal function (e.g. Chabrier, 2003) better fit the data for the distribution of stellar masses in the Milky Way. Observational evidence indicating that there are fewer low-mass stars in the Milky Way than are predicted by the Salpeter (1955) IMF came first in the form of star counts in the vicinity of the Sun provided by Gliese (1969), and subsequently by photographic surveys undertaken by Reid & Gilmore (1982), the goal of which was to locate low-mass stars throughout the Galaxy (see Kroupa, 2002 for a review).

The SFR of a galaxy can be readily estimated if the luminosity of the galaxy’s $H\alpha$ flux at some time t , $L_{H\alpha}(t)$, is known, using the simple relation derived by Kennicutt (1998); that is, $\psi(t) \propto L_{H\alpha}(t)$. The SFR depends strongly on time; in general, the SFRs of star-forming galaxies initially steadily increased over time, reached a peak – referred to as “cosmic noon” – at a redshift of $z \sim 1.5$, and have been declining ever since (Madau et al., 1998; Madau & Dickinson, 2014).

Accurate estimations for both the IMF and SFR of a galaxy allow us to obtain

a better understanding of the position of its stars on the main sequence. However, it is equally important for the work we undertake in this thesis to consider the evolution of stars off the main sequence, since we are interested in studying the chemical evolution of galaxies. Since almost all of a galaxy’s metals¹ are synthesised by stars only after they have left the main sequence, we also need to consider this stage of evolution in a star’s lifetime (again, see for instance Tinsley, 1980).

The fate of a star after it leaves the main sequence is ultimately determined by its mass. A low-mass star ($M_* \lesssim 8 M_\odot$) will leave the main sequence when it begins to “burn” hydrogen in a shell around its helium core. It then ascends the red-giant branch of the HR diagram, increasing in luminosity until the helium in its core ignites and is converted to carbon and oxygen. This causes its luminosity to fall rapidly, where it briefly joins the horizontal branch before ascending the giant branch a second time – this time along the asymptotic giant branch where the star burns both hydrogen and helium in concentric shells. Upon exhausting its nuclear fuel for the final time, the star ejects its outer hydrogen and helium envelopes as a planetary nebula, leaving behind a degenerate carbon–oxygen white dwarf.

A high-mass star ($M_* \gtrsim 8 M_\odot$) evolves in a fairly similar way, except that it has a core temperature high enough to synthesise elements heavier than carbon and oxygen in its concentric shell burning stage; these nuclear burning shells will ultimately enclose a degenerate iron core. When its nuclear fuel has been expended, the star explodes catastrophically as a Type II supernova, leaving behind either a degenerate neutron star or a black hole (e.g. Weiler & Sramek, 1988)². The metal-laden outer layers of the star are ejected outwards and into the ISM by the shockwave produced by the supernova. As a result, high-mass stars (and the supernovae that they become) are instrumental in polluting and enriching the ISM of their host galaxies with metals. Subsequent generations of stars which later form from this enriched gas will therefore have a higher metal content than their predecessors. The composition and evolution of gas in galaxies is discussed in the next subsection.

1.2.2 Interstellar Gas

The gaseous ISM represents a very large proportion of a galaxy’s total baryonic budget. The nebulae within galaxies have been known to be comprised of tenuous

¹The astrophysical definition of a “metal” refers to any element heavier than helium.

²Another class of supernovae, known as Type Ia, do not form via core collapse, but instead from the evolution of a binary star system in which one of the stars is a white dwarf which accretes material from its companion star. The white dwarf accretes material until it reaches a critical mass of $\sim 1.4 M_\odot$ (Chandrasekhar, 1931); at higher masses, electron degeneracy pressure is insufficient to prevent against further gravitational collapse and the white dwarf explodes as a Type Ia supernova (see, for instance, Branch & Tammann, 1992 for a review).

gaseous material since the pioneering work of Huggins & Miller (1864), who studied the spectra of several extended and planetary nebulae originally catalogued by William Herschel. Gaseous nebulae are observed as extended objects (e.g. Osterbrock & Ferland, 2005) that are important components within a galaxy’s ISM: it has been estimated that roughly 10% of a galaxy’s total mass (including dark matter) is in its cold ISM gas component (Naab & Ostriker, 2017).

Overwhelmingly, the ISM of a galaxy is dominated by monatomic neutral hydrogen gas (H I; e.g. Herbst, 1995; Ferrière, 2001): in the Milky Way, the fractional abundance of hydrogen is roughly 90%; the second most abundant element, helium, accounts for $\sim 10\%$ of the fractional abundance, and there are only trace amounts of heavier “metallic” elements (see Herbst, 1995 and Ferrière, 2001 for reviews of chemical abundances in the ISM of the Galaxy). ISMs do not only incorporate monatomic, neutral elements: they also contain large amounts of singly ionised hydrogen (H II) and helium, as well as molecules of hydrogen (H_2) and heavier elements. The abundance of molecular hydrogen is behind only that of atomic hydrogen, helium, and their ions (see Shull & Beckwith, 1982 for a review). Regions of singly ionised hydrogen within ISMs, known as H II regions, are of particular importance to this work, and so they will be discussed in greater detail below; Peimbert (1975) and Shields (1990) give detailed reviews on H II regions outside the Milky Way. Another important component within the ISMs of galaxies is interstellar dust; despite only making up $\sim 1\%$ of the total Milky Way ISM mass (Herbst, 1995), dust is interesting enough and of sufficient importance to this work that it deserves a separate discussion in Section 1.2.3.

Clouds of gas within ISMs are categorised as either diffuse or dense, depending on their densities (e.g. Herbst, 1995), as shown in Figure 1.4 (Charlot & Fall, 2000). About half of a galaxy’s total interstellar matter comprises the diffuse component of its ISM; this diffuse material is very tenuous, and may extend throughout the disk of the host galaxy, concentrating in the galactic plane and in the spiral arms (Ferrière, 2001). The diffuse ISM component generally also exhibits a radial density gradient, and is found to increase in concentration towards the centres of galaxies (e.g. Bigiel et al., 2008; Wild et al., 2011; Bolatto et al., 2017; Colombo et al., 2017; Lin et al., 2017). The other half of the ISM matter is concentrated into dense clouds, the largest of which are referred to as giant molecular clouds (GMCs). The high densities and low temperatures within these GMCs are conducive to the creation of new stars; as a consequence, GMCs represent sites of ongoing star formation within galaxies (e.g. Shields, 1990).

While all stars are born within GMCs, stellar migration means that only the youngest, hottest and most massive O and B stars remain in close proximity to their birth clouds, since such stars have comparatively brief lifetimes and as such do not live long enough to move away from their birth sites (e.g. Walborn et al., 1999; Sellwood & Binney, 2002; Roškar et al., 2008; Minchev & Famaey, 2010; Loebman et al., 2010; Frankel et al., 2018; Minchev et al., 2018; Feltzing et al.,

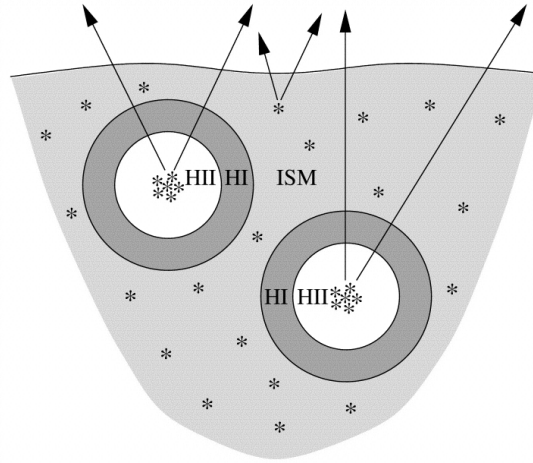


Figure 1.4: Schematic diagram showing the two main components of gas and dust within the ISMs of star-forming galaxies. The positions of stellar birth clouds (which incorporate large amounts of molecular hydrogen gas) are denoted by clusters of stars within Strömgen spheres of ionised H II (white circles). These H II regions produce both ionising line photons and non-ionising continuum photons (black arrows), and are surrounded by unionised H I envelopes (dark grey rings). Both the H II and H I regions may contain dust. The diffuse, ambient ISM component of gas and dust (light grey) is also depicted. Figure taken from Charlot & Fall (2000, Figure 1).

2020). The photons produced by these nascent stars ionise the molecular (and neutral) hydrogen gas in the GMCs, which forms a Strömgen sphere of ionised H II around the stars, as depicted in Figure 1.4 (Charlot & Fall, 2000).

GMCs, and the H II regions that they encompass, are naturally associated with prodigious local rates of star formation (e.g. Kennicutt, 1998; Kennicutt & Evans, 2012). Moreover, molecular gas is strongly associated with active sites of star formation in galaxies, as has been demonstrated by studies of the most luminous tracer of this gas, carbon monoxide (e.g. Daddi et al., 2010; Leroy et al., 2013; Santini et al., 2014; Lin et al., 2017). The dust contents of galaxies are also correlated with their SFRs (e.g. da Cunha et al., 2010; Cortese et al., 2014; Santini et al., 2014); furthermore, regions of galactic ISMs which exhibit high gas densities are also found to have high densities of interstellar dust (e.g. Heckman et al., 1998; Boissier et al., 2004; Leroy et al., 2013; Santini et al., 2014). We now therefore address this final major baryonic component of spiral galaxies.

1.2.3 Interstellar Dust

Observational evidence for the apparent absence of stars in certain locations within our own galaxy has existed since the 18th century, and can be traced back to

William Herschel, who describes an ‘opening, or hole’ within the constellation Scorpius (Herschel, 1785). Long after his death, memoirs of Herschel’s sister and fellow astronomer, Caroline, were published which clarified the meaning of his words: ‘*Hier ist wahrhaftig ein Loch im Himmel!*’ (here, truly, is a hole in the sky; Herschel, 1876).

The first instance of interstellar reddening, however, was not documented until over a century later by Trumpler (1930) during a study of open clusters in the Milky Way. He found that light within the Milky Way was selectively absorbed; moreover, this absorption was only detected in a thin layer along the plane of the Galaxy (Trumpler, 1930). The absorption (and subsequent re-radiation and reddening) of starlight was first attributed to small dust grains by Henyey & Greenstein (1941). Some of these grains are simple carbonaceous and silicate structures (e.g. Mathis et al., 1977; Draine & Lee, 1984; Weingartner & Draine, 2001); other grains may be composed of complex molecular structures such as polycyclic aromatic hydrocarbons (e.g. Mathis, 1996; Calzetti, 2001; Weingartner & Draine, 2001). Whatever their composition, dust grains typically have a range of sizes comparable to the wavelength range of optical light (Weingartner & Draine, 2001; see also Mathis et al., 1977); this means that they are prolific at both absorbing and scattering photons at wavelengths in the range $\sim 5\text{--}8000\text{ \AA}$. Optical photons absorbed by dust grains are then reprocessed into photons with infrared wavelengths, which are re-emitted in random directions. Since (as discussed below) ultraviolet–blue light is preferentially absorbed and scattered by these dust grains, starlight from galaxies is ultimately reduced and reddened by the presence of dust between the emission source and the observer (e.g. Calzetti, 2001; Salim & Narayanan, 2020). This phenomenon of absorption and scattering of light at optical wavelengths is known as dust attenuation (see reviews by Calzetti, 2001 and Salim & Narayanan, 2020).

Dust grains also exhibit a distribution in their temperatures. Typically, dust emission at far-infrared wavelengths ($\lambda \gtrsim 50\text{ }\mu\text{m}$) is attributed to grains with two temperature ranges: warm dust grains, with temperatures of $T \sim 30\text{--}70\text{ K}$, and cool dust grains, with temperatures of $T \sim 15\text{--}30\text{ K}$ (e.g. Calzetti et al., 2000; da Cunha et al., 2008). The distinction between these two dust temperatures is usually understood to be that warm dust is heated by massive, ionising stars, whereas cool dust is heated by non-ionising stars (e.g. Helou, 1986; Lonsdale Persson & Helou, 1987; Rowan-Robinson & Crawford, 1989; Calzetti et al., 2000). Both of these components are in thermal equilibrium with their environments; dust grains at shorter wavelengths ($\lambda \lesssim 50\text{ }\mu\text{m}$) are not in thermal equilibrium and may be heated to temperatures as high as $T \sim 1000\text{ K}$ (e.g. Sellgren, 1984; Draine & Anderson, 1985; Calzetti et al., 2000).

The reason that ultraviolet–blue light is preferentially absorbed by dust is because there is a greater number density of smaller grains than larger grains, as demonstrated by authors who have constructed dust attenuation curves for both

the Milky Way (e.g. Cardelli et al., 1989; O’Donnell, 1994; Fitzpatrick, 1999; see Calzetti, 2001 for a review) and in external starburst galaxies (e.g. Calzetti et al., 1994, 2000). In the attenuation curves of the Milky Way, an “ultraviolet bump” of increased dust attenuation is also found at 2175 Å (e.g. Cardelli et al., 1989; Fitzpatrick, 1999). This feature is thought to arise due to the presence of small carbonaceous dust grains (e.g. Draine, 1989; Weingartner & Draine, 2001). Attenuation curves for the Milky Way, the Small and Large Magellanic Clouds, and starburst galaxies are shown in Figure 1.5 (Calzetti, 2001).

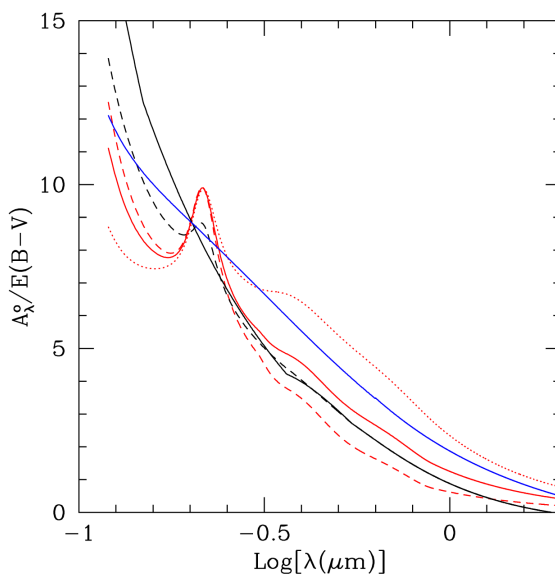


Figure 1.5: Dust attenuation curves for various different galaxies. Ultraviolet–blue light suffers significantly more dust attenuation than red–infrared light. Red lines: three different attenuation curves for the Milky Way, using data from Cardelli et al. (1989) and Fitzpatrick (1999). The line style denotes that different R_V values (see Section 3.3.1.2) are used: the solid red line shows $R_V = 3.1$; the dashed red line shows $R_V = 5.0$; the dotted red line shows $R_V = 2.0$. In all three cases, the ultraviolet bump at 2175 Å is clearly visible. Solid and dashed black lines: attenuation curves for the Small and Large Magellanic Clouds, using data from Gordon & Clayton (1998) and Misselt et al. (1999), respectively. Blue line: attenuation curve for starburst galaxies (Calzetti et al., 2000). Figure taken from Calzetti (2001, Figure 1).

Dust grains are predominately located within the ISMs of galaxies. Their distribution within a given galaxy is also similar to that of the interstellar gas: dust within the galaxy may be either diffuse or dense, and there are significant differences between the two components. The diffuse dust component exhibits a radial gradient similar to that shown by the gas (e.g. Peletier et al., 1995; Boissier et al., 2004; Muñoz-Mateos et al., 2009; Wild et al., 2011; González Delgado et al., 2015; Goddard et al., 2016), whereas the dust associated with stellar birth clouds

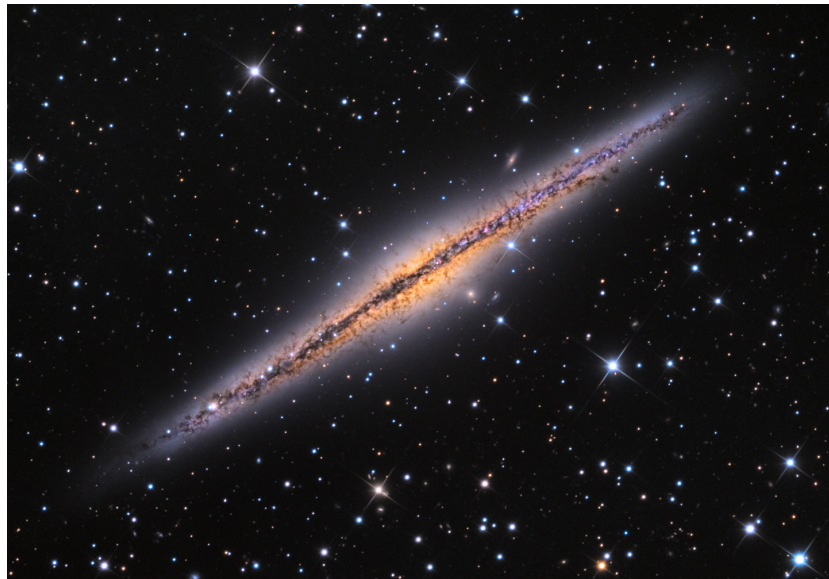


Figure 1.6: The nearby edge-on spiral galaxy NGC 891. Light at optical wavelengths, produced by stars within the galactic disk, is clearly seen to be both reddened and to suffer significant attenuation by dust in the ISM of the galaxy. *Image Credit: Adam Block, Mt. Lemmon SkyCenter, University of Arizona.*

is more concentrated, clumpier, and optically thicker than the surrounding ISM (e.g. Lonsdale Persson & Helou, 1987; Charlot & Fall, 2000; Calzetti, 2001; Wild et al., 2011; Wuyts et al., 2013; Price et al., 2014). These two different dust components are shown schematically in Figure 1.4 (Charlot & Fall, 2000), and both components will be discussed in greater detail as part of our analysis of dust in spiral galaxies that we undertake in Chapter 3.

Interstellar dust is therefore of particular importance to any serious investigation of spiral galaxies. It is well known that the opacity of dust is greater in spiral arms than in the inter-arm regions of such galaxies (e.g. White & Keel, 1992; White et al., 2000; Holwerda et al., 2005). As discussed in Section 1.1.2 (and references therein), long dust lanes are found to be intimately linked with the spiral arms for many nearby galaxies. These dust lanes are also ubiquitous in edge-on galaxies (e.g. Dalcanton et al., 2004; Galliano et al., 2017; Holwerda et al., 2019), if the galaxy has a stellar mass above $\sim 10^9 M_{\odot}$ (Dalcanton et al., 2004; Holwerda et al., 2019). Dust (in both edge-on and face-on spiral galaxies) is also found to be optically thick at all radii (White et al., 2000). Figure 1.6 highlights an exquisite example of dust attenuation in the disk of the edge-on spiral galaxy NGC 891; the light produced by stars in edge-on spirals suffers much more attenuation and more reddening than that produced by stars in their face-on counterparts (cf. Figure 1.2).

Having discussed the building blocks of galaxies – the stars and the ISMs (and

the gas and dust from which the ISMs are formed) – we now turn our attention to the chemical compositions of these two components in the following Section.

1.3 Chemical Compositions of Galaxies

An understanding of the chemical compositions of galaxies is fundamental in order to learn more about their stellar populations and nebular gas. Studying the evolution of the chemical properties of both the stars and the gas in galaxies over cosmic time can unlock crucial information about the processes driving galactic formation and evolution. Before we can study the chemical evolution of galaxies, however, we first need to know the methods by which the levels of heavy elements in the stars and gas within these galaxies can be measured. We therefore give a brief outline of these tools in Section 1.3.1. We discuss the relationship between metallicities and other important galactic properties, such as stellar masses and star formation rates, in Section 1.3.2. Finally, we provide a short review of the chemical evolution of galaxies, and summarise the astrophysical concepts discussed throughout this introductory Chapter, in Section 1.3.3.

1.3.1 Metallicities

Typically, the chemical compositions of galaxies are quantified by determining the levels of elements heavier than helium – the “metallicities” – of the stars and gas within these galaxies. Recent reviews by Kewley et al. (2019) and Maiolino & Mannucci (2019) comprehensively discuss galactic gas metallicities, and Madau & Dickinson (2014) and Maiolino & Mannucci (2019) review metallicities of the stellar populations within galaxies.

The metallicity Z of an astrophysical object is simply defined as the mass of metals relative to the total mass of baryons – i.e. $Z \equiv M_{\text{metals}}/M_{\text{baryons}}$ (see for instance Maiolino & Mannucci, 2019). Often, we want to know the relative abundance of two arbitrary chemical elements A and B. We can express these in terms of the relative number densities N , relative to the Solar value:

$$[A/B] \equiv \log(N_A/N_B) - \log(N_A/N_B)_\odot. \quad (1.1)$$

Henceforth, square brackets will be used to indicate that a given abundance ratio is the logarithm of the ratio relative to its Solar value, as in Equation (1.1). Using Equation (1.1), we can express the relative abundance ratio of the total metal content, M , to hydrogen of an astrophysical object – denoted $[M/H]$ – only in terms of the metal fraction Z and the hydrogen fraction X of the object (if the

Solar values of these quantities are known) as follows:

$$[M/H] = \log(Z/X) - \log(Z/X)_{\odot} = \log(Z/Z_{\odot}) - \log(X/X_{\odot}). \quad (1.2)$$

Here, $Z_{\odot} = 0.0142$ is the Solar metallicity and $X_{\odot} = 0.7154$ is the Solar mass fraction of hydrogen (Asplund et al., 2009). Since the Universe is overwhelmingly dominated by hydrogen (and helium), $Z \ll X$ for any given astronomical object; $\log(Z/Z_{\odot})$ hence shows a much greater variation than $\log(X/X_{\odot})$. We can therefore ignore the $\log(X/X_{\odot})$ term and write an approximate expression for Equation (1.2) as simply:

$$[M/H] \simeq \log(Z/Z_{\odot}). \quad (1.3)$$

Note that the approximation we make here that $Z \ll X$ is a very good one simply because the Universe contains so much hydrogen: for instance, the ratio of the Solar values of X and Z quoted earlier, $X_{\odot}/Z_{\odot} \sim 50$ (Asplund et al., 2009). We shall therefore use the expression for $[M/H]$ in Equation (1.3) when quoting both stellar and gas metallicities in Chapters 4 and 5 of this thesis.

It is often difficult in practice to directly determine metallicities; instead, certain abundance ratios are commonly used as metallicity proxies. For instance, stellar “metallicities” are often quoted as the abundance ratio of iron to hydrogen in the atmosphere of the star – i.e. $[\text{Fe}/\text{H}]$ – since iron absorption lines are generally readily identifiable in stellar spectra (e.g. Tinsley, 1980; Wheeler et al., 1989). The iron to hydrogen abundance ratio is, from Equation (1.1):

$$[\text{Fe}/\text{H}] \equiv \log(N_{\text{Fe}}/N_{\text{H}}) - \log(N_{\text{Fe}}/N_{\text{H}})_{\odot}. \quad (1.4)$$

While absorption lines of iron are easily observed in stellar spectra, the most common metal in the ISMs of galaxies, by contrast, is oxygen (e.g. Tinsley, 1980; Asplund et al., 2009). It is therefore commonplace to express gas metallicities in terms of their oxygen abundance, since not only is oxygen copious, but it also produces very strong emission lines (e.g. Maiolino & Mannucci, 2019). The oxygen abundance of the ISM of a galaxy is conventionally written in the form:

$$12 + \log(\text{O}/\text{H}) \equiv 12 + \log(N_{\text{O}}/N_{\text{H}}), \quad (1.5)$$

where $12 + \log(\text{O}/\text{H})_{\odot} = 8.69$ (Asplund et al., 2009). This notation will be used in certain instances to express gas metallicities in Chapter 5.

In the next subsection, we explore how and why the metallicities of both the stars and gas within galaxies evolve over cosmic time.

1.3.2 Linking Metallicities with other Physical Properties

As discussed in Section 1.2.1, high-mass ($\gtrsim 8M_{\odot}$) stars (and accreting white-dwarf binary stars) end their lives violently as supernovae; as they die, they expel the products of their nucleosynthesis into the surrounding ISM, thus enriching the surrounding gas with metals (see, for instance, Tinsley, 1980). The upshot of this process of ISM “pollution” is that subsequent generations of stars will form from this enhanced material. High-mass stars will repeat this cycle of ISM pollution, whereas low-mass stars will lock up some of the enriched ISM material in their degenerate cores. The metallicities – of both the stars and the gas – of galaxies must, therefore, be intimately linked with other important physical properties, such as their stellar masses and star formation rates; additionally, the evolution of metallicities must also be intertwined with the evolution of these quantities over cosmic time. The interplay between stellar metallicity, gas metallicity, stellar mass, and SFR is reviewed at low and high redshifts by Sánchez (2020) and Förster Schreiber & Wuyts (2020), respectively; we discuss the main points relevant to this work below.

The first data release of the Sloan Digital Sky Survey (York et al., 2000), which made publicly available photometric and spectroscopic data for $\sim 150\,000$ galaxies (Abazajian et al., 2003), precipitated a new era of large-scale data analysis for the field of galaxy evolution. The veritable treasure trove of available data revolutionised our understanding of galaxies. In particular, several of the four aforementioned properties of galaxies were conclusively found to be closely linked with one another. Firstly, Brinchmann et al. (2004) demonstrated the existence of a fundamental relationship showing that increased stellar masses lead to increased SFRs in star-forming galaxies; later authors, who verified this result, subsequently dubbed this relation the “star-formation main sequence” (SFMS; e.g. Noeske et al., 2007; Elbaz et al., 2007; Daddi et al., 2007; Peng et al., 2010; Whitaker et al., 2012). The SFMS of Whitaker et al. (2012) is shown in Figure 1.7. In the very same year, building on the seminal work of Lequeux et al. (1979), a stellar mass–gas metallicity relation (MZ_{gR}) was also reported (Tremonti et al., 2004; see also, for instance, Mannucci et al., 2010; Zahid et al., 2013b; Maiolino & Mannucci, 2019); the year after, Gallazzi et al. (2005) found, for the same sample of galaxies, a corresponding stellar mass–stellar metallicity relation ($MZ_{\text{*R}}$; see also, for instance, Panter et al., 2008; Vale Asari et al., 2009; González Delgado et al., 2014)³. Both the MZ_{gR} of Tremonti et al. (2004) and the $MZ_{\text{*R}}$ of Panter et al. (2008) are shown in Figure 1.8. Reviews of the SFMS are given by Sánchez (2020) and Förster Schreiber & Wuyts (2020); reviews of both of the MZ_{gR} and the $MZ_{\text{*R}}$ can be found in Maiolino & Mannucci (2019) and Sánchez (2020).

³Note that there is no such thing as the stellar metallicity of a galaxy; in practice what is actually meant here is some average value of the *distribution* of metallicities for the stars in a given galaxy.

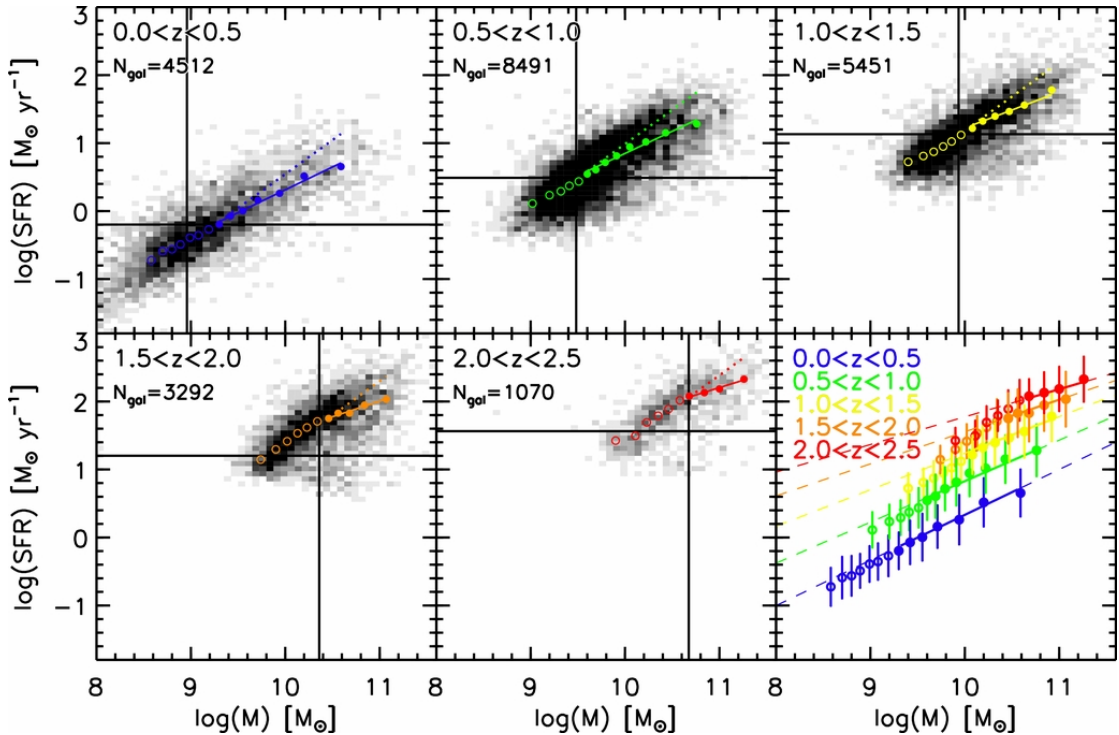


Figure 1.7: SFR versus mass (the SFMS) plotted at a range of different redshifts between $0.0 < z < 2.5$ for star-forming galaxies. Figure taken from Whitaker et al. (2012, Figure 1).

Each of these three relations – the SFMS, the MZ_gR , and the MZ_*R – is known to evolve with cosmic time. The zeropoint evolution of the SFMS, as documented by, for instance, Noeske et al. (2007), Whitaker et al. (2012), and Speagle et al. (2014), mirrors the general decline in cosmic star formation activity between “cosmic noon” ($z \sim 1.5$) and the present epoch (e.g. Madau et al., 1996; Madau & Dickinson, 2014). The MZ_gR has, by contrast, been found to increase to values of higher gas metallicity over cosmic time (e.g. Maiolino et al., 2008; Moustakas et al., 2011; Zahid et al., 2013a, 2014b; Lian et al., 2018a,b; Yates et al., 2021). This evolution is to be anticipated within the simple model for the pollution of galactic ISMs described above, since each generation of star formation raises the metallicity of the gas in its immediate vicinity. Over cosmic time, therefore, we should expect the average gas metallicities of galaxies to steadily increase (e.g. Maiolino & Mannucci, 2019). The MZ_*R has been shown to evolve in a very similar way to the MZ_gR , whereby stellar metallicity gradually increases over cosmic time, with high-mass galaxies found to evolve faster than low-mass ones (e.g. Camps-Fariña et al., 2021, 2022; Fontanot et al., 2021; Yates et al., 2021; Kashino et al., 2022).

It is perhaps not surprising that there is likely to be an underlying relation between the stellar masses, gas metallicities, and SFRs of galaxies. The exist-

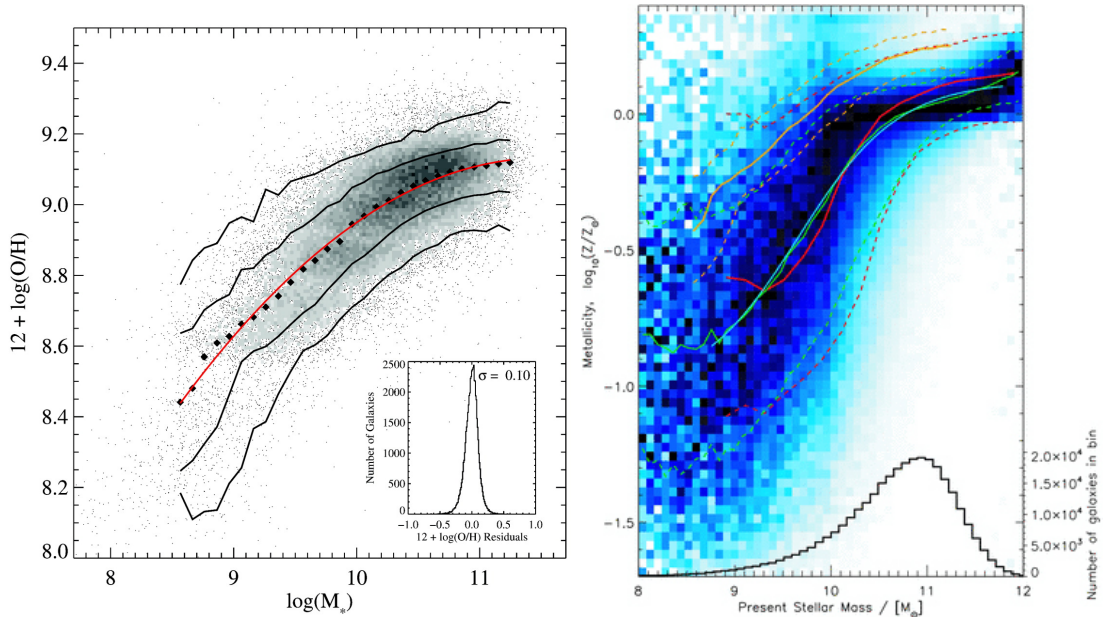


Figure 1.8: Left: the MZ_{gR} (Figure taken from Tremonti et al., 2004, Figure 6). Right: the MZ_{*R} (Figure taken from Panter et al., 2008, Figure 6); orange and red lines show fits to the data of Tremonti et al. (2004, i.e., the left-hand plot) and Gallazzi et al. (2005), respectively. Both Tremonti et al. (2004) and Panter et al. (2008) used similar samples of low-redshift SDSS galaxies to produce these plots.

tence of a “fundamental (gas) metallicity relation” (FMR) has been posited by several authors, including Mannucci et al. (2010), Lara-López et al. (2010), Yates et al. (2012), Sanders et al. (2018, 2021), and Curti et al. (2020)⁴. The FMR of Mannucci et al. (2010) is shown in Figure 1.9. Essentially, the FMR is a tight, three-dimensional relation between stellar mass, gas metallicity, and SFR; an extensive review of the FMR – and its origin – is given by Maiolino & Mannucci (2019). Interestingly – and unlike either the SFMS or the MZ_{gR} – the FMR does not seem to evolve with redshift out to at least $z \sim 2.5$ (Mannucci et al., 2010), and possibly even $z \sim 3.3$ (Sanders et al., 2021).

Unfortunately, there appears to have been very little research undertaken on whether there exists a similar FMR for the stellar metallicities of galaxies. Since relevant papers seem to be few and far between, conclusions on the existence of a corresponding three-dimensional stellar mass–stellar metallicity–SFR plane are rather tentative. Nevertheless, simulations performed by Martel et al. (2018)

⁴Some authors do dispute the validity of such a relation (see, for instance, Kashino et al., 2016, who claim that the strength of the SFR dependence in the FMR is influenced strongly by the choice of metallicity calibrator; see also Telford et al., 2016 and Cresci et al., 2019, who find that the FMR may be weaker than reported by Mannucci et al., 2010 and Lara-López et al., 2010). For the purposes of this thesis, however, we assume the existence of such an FMR, in line with various of its proponents referenced above.

and Matthee & Schaye (2018) do seem to suggest that $[\text{Fe}/\text{H}]$ (stellar) metallicities exhibit similar behaviour in this three-dimensional plane to their $[\text{O}/\text{H}]$ (gas) metallicity counterparts, albeit the relationship between these quantities is found to be rather weak.

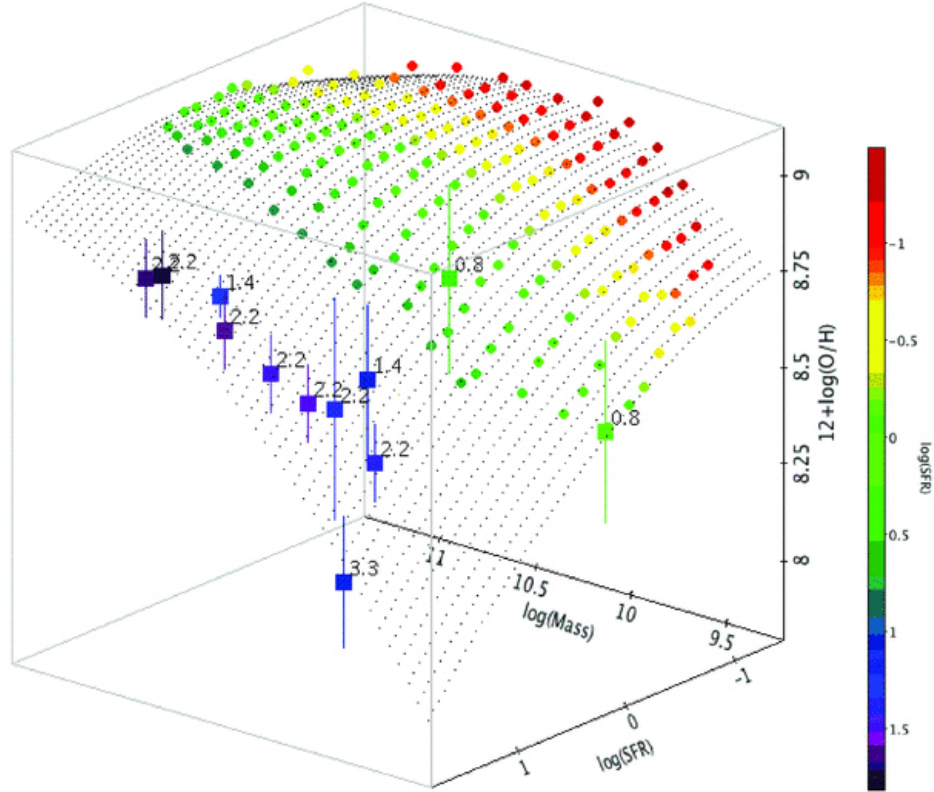


Figure 1.9: A projection of the FMR of Mannucci et al. (2010) in stellar mass–SFR–gas metallicity parameter space. Circles, coloured by SFR, denote the median gas metallicities of local SDSS galaxies in bins of M_* and SFR. The black dots represent a second-order fit to these SDSS data (Equation 5.4). Labeled squares denote the redshifts and positions in this parameter space of specific high-redshift ($0.8 \leq z \leq 3.3$) galaxies. Figure taken from Mannucci et al. (2010, Figure 2).

We shall now conclude this Section by introducing the final crucial components required for this work: models for the chemical evolution of galaxies. We shall also bring together all of the topics previously discussed in this introductory Chapter, and explain how they will aid us in our ultimate goal of determining the cosmic chemical evolution histories of spiral galaxies.

1.3.3 The Astrophysics of Chemical Evolution

The ultimate goal of this thesis is to better understand how the chemical compositions of the stars, gas, and dust within spiral galaxies evolve with cosmic time. In order to achieve this, we shall make use of chemical evolution models. We therefore give a brief overview of these models below.

Models for the chemical evolution of galaxies were originally developed and formalised from observations made of stars in the Solar neighbourhood⁵. Early efforts to model the chemical evolution of the stars within this local region, beginning with the work of Schmidt (1959, 1963), are reviewed by Pagel & Patchett (1975), Trimble (1975), Audouze & Tinsley (1976), and Tinsley (1980).

The simplest, and perhaps the most intuitive, model to explain chemical evolution in the Solar neighbourhood would be to assume that the Milky Way formed from a single initial cloud of completely pristine gas, and that no gas flowed into, or out of, the system over the course of its life (e.g. Trimble, 1975; Tinsley, 1980). To simplify the model further, the IMF is assumed to be constant, and the gas is assumed to be chemically homogenous at any time (e.g. Trimble, 1975; Tinsley, 1980). Such a model, borne out of work originally undertaken by Schmidt (1959, 1963), is nowadays referred to as a “closed box” model of galaxy evolution; however, when first formalised by Talbot & Arnett (1971), it was commonly called a “one-zone, homogeneous” model.

Unfortunately, problems begin to arise if the Solar neighbourhood is modelled as a simple closed box. The most serious of these issues is the “G-dwarf problem”, which was originally documented in the Solar neighbourhood by van den Bergh (1962) and Schmidt (1963). In a nutshell, the closed box model hugely over-predicts the number of low-metallicity G dwarfs in the Solar neighbourhood when compared with the metallicity distributions constructed from actual observations of the stellar populations (see reviews by Pagel & Patchett, 1975, Audouze & Tinsley, 1976, and Tinsley, 1980). Figure 1.10 (Rocha-Pinto & Maciel, 1996) shows the nature of this problem for stars in the Solar neighbourhood. The G-dwarf problem is prevalent not just in the vicinity of the Sun, but throughout the

⁵The Solar neighbourhood is defined (by, for instance, Tinsley, 1974) as a region in the Galactic plane, shaped like a cylindrical shell encircling the Galactic centre at the Sun’s galactocentric distance. The ring-shaped cylindrical shell has a thickness of ~ 1 kpc, with a radius that extends to the Galactic centre, and it extends ~ 1 kpc out of the Galactic plane.

entire Milky Way (e.g. Chiappini et al., 2001; Hayden et al., 2015).

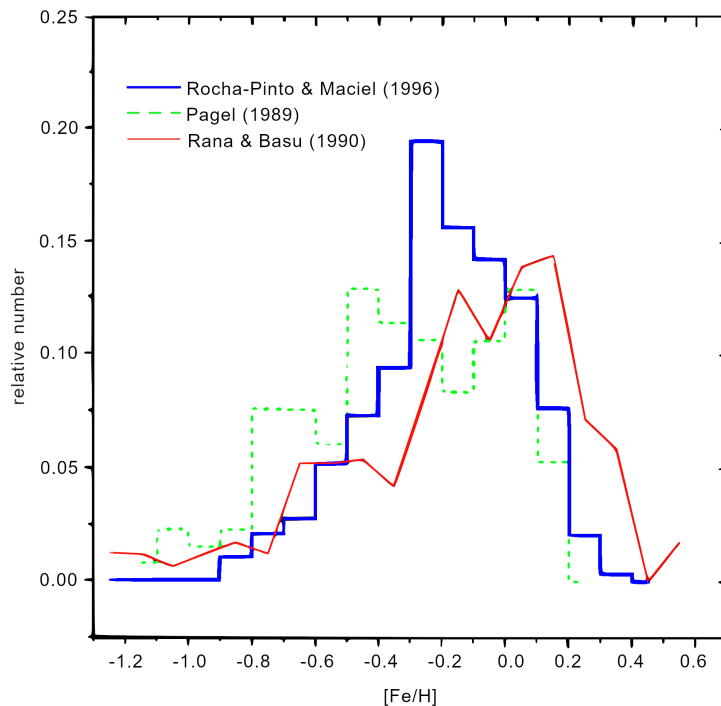


Figure 1.10: Metallicity distributions of stars in the Solar neighbourhood, using data from Pagel (1989, dashed green line); Rana & Basu (1990, red line); and Rocha-Pinto & Maciel (1996, blue line). These distributions show that surprisingly few metal-poor stars are observed in the Solar neighbourhood, confirming the existence of the G-dwarf problem in this region. A greyscale version of this Figure can be seen in Rocha-Pinto & Maciel (1996, Figure 4); this colour version has been kindly provided by Helio Rocha-Pinto (*private communication*).

In order to address issues such as the G-dwarf problem in the Solar neighbourhood, more sophisticated chemical evolution models were subsequently proposed that dropped either some or all of the assumptions for the closed box model mentioned above (see, for instance, Tinsley, 1974; Trimble, 1975). These included models which allow for inflows (the “accreting box” model; see Larson, 1972, 1976) and for outflows (the “leaky box” model; see Hartwick, 1976) of gas into and out of the Galaxy, respectively. We refer the reader to Binney & Merrifield (1998) for comprehensive discussions on each of these three models. More complex models, such as “bathtub models” (see for instance Finlator & Davé, 2008, Lilly et al., 2013, and Belfiore et al., 2019a) which allow for the simultaneous treatment of gas inflows and outflows in galaxies, are beyond the scope of this thesis.

It was ultimately found that the accreting box model largely solved the G-dwarf problem in the Solar neighbourhood: by continually feeding pristine gas into the Galaxy, there is sufficient fuel available for increased star formation at later times,

which means that a greater proportion high-metallicity stars will be produced (e.g. Tinsley, 1974, 1975; Tinsley & Larson, 1978). However, the question of whether such a model could accurately model the metallicity distribution of stars in galaxies other than our own still remained. We therefore revisit, and propose a universal solution to, the G-dwarf problem in Chapter 4.

Chemical evolution models, such as the ones described above, fundamentally help us to understand how the stars, gas and dust within galaxies evolve over cosmic time by placing constraints on the stellar masses, SFRs, and metallicities of these galaxies. Consequently, these models can in turn be used to understand how the relations between these quantities (i.e. the SFMS and the mass–metallicity relations – see Section 1.3.2) evolve. In order to investigate the chemical evolution of spiral galaxies, we must, therefore, do the following.

1. Firstly, we need to find out whether the accreting box model presents a universal solution to the G-dwarf problem, or whether its success is limited to the Milky Way. In the latter case, then we additionally need to present a solution to the G-dwarf problem in galaxies other than our own. We undertake this investigation in Chapter 4, in which we test how the stellar metallicity distribution of a galaxy is influenced by its stellar mass. The goal of this work will be to acquire a general model for the chemical evolution of spiral galaxies.
2. We can then investigate the evolution histories of the stellar and gas metallicities within these same galaxies. This work is presented in Chapter 5. Understanding how the metallicities of both the stars and the gas evolve will finally allow us to address the original question posed by this thesis: how do the chemical compositions of spiral galaxies change over cosmic time?

However, to illustrate the wealth of information that we have at our disposal, we also undertake an investigation of the distribution of dust within spiral galaxies, as well as how the concentration of this dust depends upon stellar mass. This work is presented in Chapter 3. This work will in some sense link in with subsequent Chapters, since higher mass galaxies exhibit higher gas metallicities which in turn leads to increased dust attenuation, since more metals are locked into dust grains (these grains are, by definition, metals; for a discussion of this process see for instance Heckman et al., 1998 or Boissier et al., 2004). As an auxiliary benefit, the work undertaken in Chapter 3 will ensure that we have the necessary framework in place to correct for the presence of dust attenuation when deriving SFRs and gas metallicities throughout this thesis. Ultimately, however, we undertake the research in Chapter 3 because it is interesting in its own right, and because there is simply a wealth of data with which we can play, as we shall see in Chapter 2.

The final Section of this introductory Chapter will explain how this thesis will be presented in order to achieve the goals laid out above.

1.4 Structure of this Thesis

This thesis is structured as follows. In Chapter 2, we describe the methods by which the raw data used in this thesis were acquired. We also discuss the processes by which the samples of spiral galaxies were selected, as well as technical details of the stellar population synthesis methods used in this work. Chapter 3 presents our investigation of spatially resolved dust attenuation in spiral galaxies; this analysis includes both the dust attenuation affecting the stellar populations as well as that in the gas of the same galaxies. We explore the radial dependence of dust attenuation upon important galactic properties such as stellar mass and SFR, and use our findings to determine the distribution and concentration of dust in these galaxies. In Chapter 4 we revisit the G-dwarf problem and produce stellar metallicity distributions for a large number of spiral galaxies. We demonstrate that different chemical evolution models must be considered for galaxies of differing stellar masses. In Chapter 5 we build on the research presented in Chapter 4 and investigate how the stellar and gas metallicities of spiral galaxies evolve with cosmic time. Finally, the conclusions of this thesis, as well as potential future work that could be undertaken, are discussed in Chapter 6.

Throughout this thesis, we employ a Chabrier (2003) initial mass function (IMF), and use the solar metallicity value of $Z_{\odot} = 0.0142$ determined by Asplund et al. (2009). We assume a Λ CDM cosmology with $\Omega_M = 0.3$, $\Omega_{\Lambda} = 0.7$, and $H_0 = 70 \text{ km s}^{-1} \text{ Mpc}^{-1}$.

Chapter 2

Observational Data and Technical Analysis

This Chapter describes in detail the observational data employed in this thesis. Firstly, and most importantly for this work, we discuss the technical details, the sample selection procedure, and the data reduction processes of the MaNGA galaxy survey in Section 2.1. Section 2.2 details the criteria we use to draw subsamples of galaxies that we ultimately use for data analysis in this work from the full MaNGA sample. Section 2.3 describes the software **STARLIGHT** that is used throughout this work to perform spectral fitting upon the subsamples of MaNGA galaxies, and finally Section 2.4 summarises the data described in this Chapter and explains how we intend to analyse these data products in subsequent Chapters.

2.1 SDSS-IV MaNGA

The fourth generation of the Sloan Digital Sky Survey (SDSS-IV; Blanton et al., 2017) encompassed three major astronomical surveys: the Apache Point Observatory Galactic Evolution Experiment 2 (APOGEE-2; Majewski & The APOGEE and APOGEE-2 Teams, 2016); the extended Baryon Oscillation Spectroscopic Survey (eBOSS; Dawson et al., 2016); and the Mapping Nearby Galaxies at Apache Point Observatory (MaNGA; Bundy et al., 2015) galaxy survey. This thesis uses only data from MaNGA. Observations for the MaNGA survey officially began at the Apache Point Observatory (APO) in Sunspot, New Mexico, USA in August 2014; observations concluded in August 2020. Over the course of these six years, MaNGA obtained high-quality spectra for a total of 10145 galaxies, of which 10010 were unique observations. As a result, MaNGA represents the largest integral field unit (IFU) galaxy survey of its kind. The full sample of reduced data has recently been made publicly available as part of the seventeenth (and final) SDSS-IV data release (DR17; Abdurro'uf et al., 2022).

In a nutshell, the basic principle of IFU spectroscopy involves combining the detailed wavelength resolution afforded by single-slit spectroscopy with the spatial information of traditional two-dimensional imaging. Integral field spectroscopy thus allows many spectra to be obtained at multiple different spatial locations across the face of a given astronomical target. Although this concept has been around since the 1980s (e.g. Bacon et al., 1988, 1995; Barden & Wade, 1988; Arribas et al., 1998), large-scale IFU surveys, such as SDSS-IV MaNGA, are a fairly recent phenomenon. The first of these major surveys was SAURON (de Zeeuw et al., 2002), whose success precipitated a flurry of subsequent observations and ushered in the golden era of IFU surveys with the likes of the ATLAS^{3D} project (Cappellari et al., 2011b), the Calar Alto Legacy Integral Field Area (CALIFA; Sánchez et al., 2012) survey, the Sydney-AAO (Australian Astronomical Observatory) Multi-object Integral field spectrograph (SAMI; Croom et al., 2012) galaxy survey, the SAGES (Study of the Astrophysics of Globular Clusters in Extragalactic Systems) Legacy Unifying Globulars and Galaxies Survey (SLUGGS; Brodie et al., 2014), and, of course, the MaNGA (Bundy et al., 2015) galaxy survey itself.

The future of IFU observations looks bright, with part of the fifth generation of the Sloan Digital Sky Survey (SDSS-V; Kollmeier et al., 2017) devoted to continuing integral field spectroscopy with the Local Volume Mapper (LVM; Konidaris et al., 2020). With the advent of new facilities such as the Dark Energy Spectroscopic Instrument (DESI; Levi et al., 2019), the Multi Object Optical and Near-infrared Spectrograph for the Very Large Telescope (MOONS; Cirasuolo et al., 2020), and the High Angular Resolution Monolithic Optical and Near-infrared Integral field spectrograph for the Extremely Large Telescope (HARMONI; Laurent et al., 2018), the next generation of IFU surveys will surely provide fertile fields of research for many years yet to come.

We now turn our attention back to the MaNGA galaxy survey. The following subsections outline, in turn, the instrumentation required to carry out MaNGA observations (Section 2.1.1), the sample of galaxies observed by MaNGA (Section 2.1.2), and finally the data reduction (Section 2.1.3) and data analysis (Section 2.1.4) pipelines implemented to process the raw MaNGA data.

2.1.1 Instrumentation

In the following subsections, we outline technical details of the various instruments that actually performed the observations and obtained the raw data integral to this work.

2.1.1.1 The Sloan Telescope at APO

MaNGA made use of observations obtained by the SDSS telescope at APO (Figure 2.1; Gunn et al., 2006). The telescope used was a modified Ritchey-Chrétien alt-azimuth reflector (York et al., 2000; Gunn et al., 2006). The diameters of the primary and secondary mirrors are 2.5 m and 1.08 m, respectively, and the telescope has a focal ratio of $f/5$ (York et al., 2000; Gunn et al., 2006). Ritchey-Chrétien telescopes are similar in design to Cassegrain telescopes, which contain a parabolic primary mirror and a hyperbolic secondary mirror that reflects the light back through a hole in the primary mirror. However, Ritchey-Chrétien variants instead employ two hyperbolic mirrors, rather than using a parabolic primary mirror. In addition to eliminating spherical aberration within the primary mirror, this design also affords the Sloan telescope a very wide (3°) field of view (York et al., 2000; Gunn et al., 2006), which made it the ideal telescope to carry out a survey such as MaNGA.

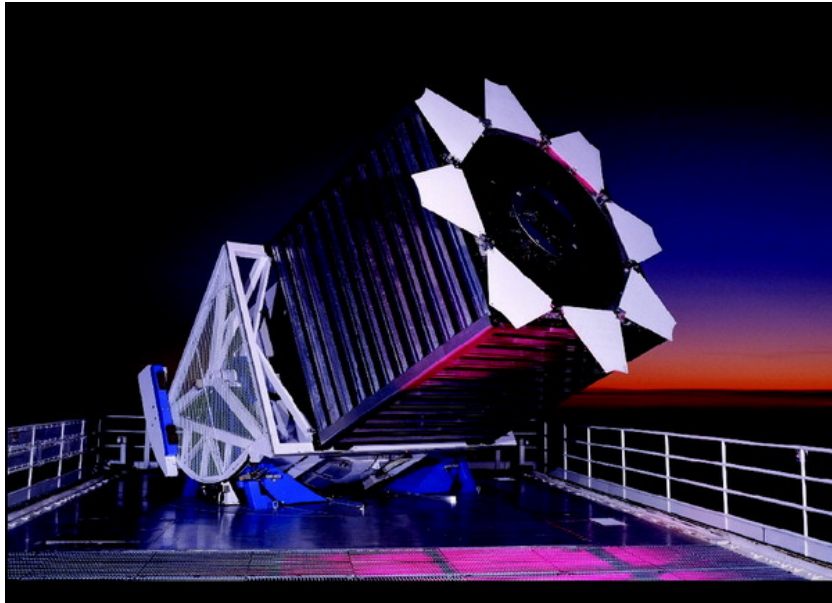


Figure 2.1: The SDSS telescope at APO, ready to commence observations. Figure taken from Gunn et al. (2006, Figure 2).

The telescope officially began observations on 10 May 1998 after the photometric camera was constructed (Gunn et al., 1998). The design of the telescope allows for high-quality photometric (Gunn et al., 1998; York et al., 2000) and spectroscopic (York et al., 2000; Gunn et al., 2006) observations, both of which were critical to the success of IFU surveys like MaNGA. Furthermore, geometric distortions over the wavelength range $3000 - 10600 \text{ \AA}$ are very small (Gunn et al., 2006), which again was particularly salient to the success of MaNGA as an IFU survey.

2.1.1.2 The BOSS Optical Spectrographs

Two identical spectrographs, mounted on the Sloan telescope at APO, were used to obtain spectrographic observations of the MaNGA galaxies. The original twin spectrographs installed at the telescope (Uomoto et al., 1999) were subsequently upgraded in preparation for the Baryon Oscillation Spectroscopic Survey (BOSS; Schlegel et al., 2009; Dawson et al., 2013), as well as its successor, eBOSS (Dawson et al., 2016). The BOSS spectrographs are described in detail in Smee et al. (2013).

It is relevant for this work to note that the BOSS spectrographs’ wavelength ranges entirely span the optical spectrum from 3600 – 10300 Å (Smee et al., 2013). Furthermore, the spectrographs have a resolving power, R , of $R \sim 2000$ (Smee et al., 2013). Resolving power is defined as wavelength, λ , divided by the full width at half-maximum (FWHM) of the one-dimensional line spread function of the spectrograph – i.e., $R = \lambda/\text{FWHM}$. The resolving power of the spectrographs is not constant; it varies with wavelength, falling to $R \sim 1500$ at $\lambda < 4000$ Å, and reaching a peak value of $R \sim 2500$ at a wavelength of $\lambda \sim 9000$ Å (see Figure 2.2; Smee et al., 2013). The corresponding range of velocity dispersions able to be resolved by the BOSS spectrographs is $\sim 100 - 200 \text{ km s}^{-1}$ (Smee et al., 2013).

2.1.1.3 The MaNGA IFU Fibre Feed System

Like all IFU surveys, the fundamental goal of MaNGA was to provide spatially resolved spectroscopy of its targets. MaNGA acquired high-quality spatial and spectroscopic observations via the use of its fibre feed system, described fully by Drory et al. (2015), which connected the BOSS spectrographs to the Sloan telescope at APO.

Hexagonal arrangements of IFU fibres were used to obtain spatial coverage of the MaNGA galaxies. Although hexagonal fibre bundles have a lower filling factor¹ than an equivalent number of fibres arranged in a circle, the iconic hexagonal formation of MaNGA had myriad advantages. Not only did such a geometry allow fibres to be regularly spaced within each IFU, fibre throughput was also improved, and fibres were additionally less likely to suffer breakages (Law et al., 2015). MaNGA employed five different IFU sizes (see Figure 2.3; Drory et al., 2015; Bundy et al., 2015): bundles of 19, 37, 61, 91, and 127 individual fibres were utilised (Bundy et al., 2015; Drory et al., 2015; Wake et al., 2017). The corresponding fields of view of these bundle sizes ranged from 12" in diameter for the 19 fibre bundle, up to 32" in diameter for the largest bundle of 127 fibres (Drory et al., 2015).

Each IFU fibre bundle had to be plugged by hand into purpose-drilled alu-

¹The filling factor of an IFU is simply the area on the sky actually seen by the combined IFU fibres divided by the total IFU “footprint”. Circular arrangements of fibres can be more densely packed, and therefore have higher filling factors, than the same fibres in a hexagonal formation.

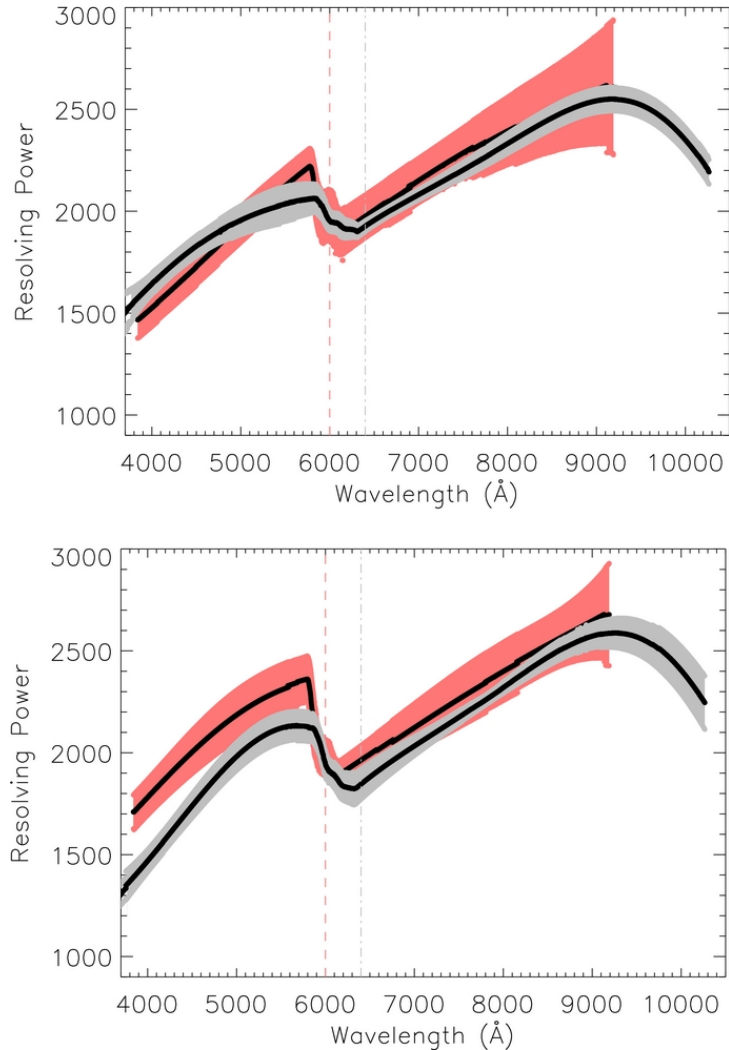


Figure 2.2: Mean resolving power as a function of wavelength for the twin SDSS (red) and upgraded BOSS (grey) spectrographs for a random sample of 100 plates. The upper plot depicts data from one of the SDSS and one of the BOSS spectrographs; the lower plot shows the corresponding data from both of these spectrographs' respective twins. The shaded regions show the 1σ uncertainty on the data. For the SDSS spectrographs, a dichroic beamsplitter ensures that light blueward of 6000 Å (dashed red line) is reflected into the blue channel, and that light redward of this threshold is transmitted into the red channel; for the upgraded BOSS spectrographs, the beamsplitter threshold is 6400 Å (dashed grey line). Each function shows a general increase with wavelength; this increase, however, is not monotonic despite the fact that resolving power is directly proportional to wavelength. The decreases seen at ~ 6000 Å occur because both of the given spectrograph's two channels contribute to this region, each with different dispersive elements (Smee et al., 2013). Figure taken from Smee et al. (2013, Figure 35).

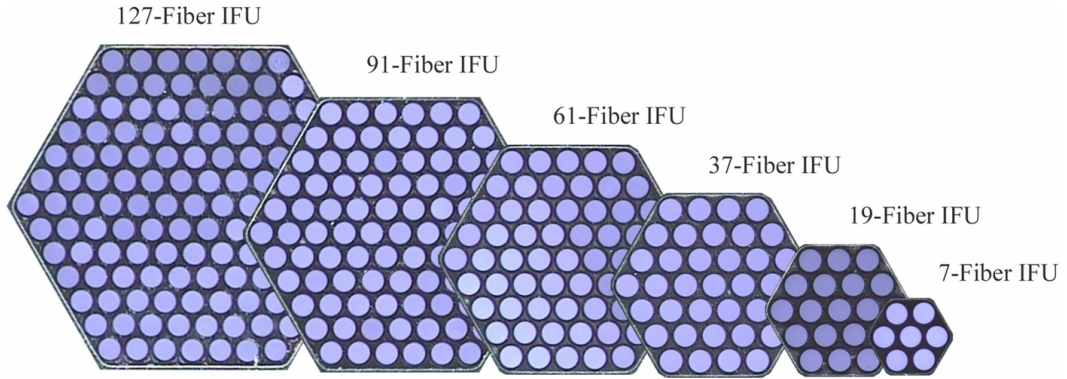


Figure 2.3: Real images of the various IFU bundle sizes employed by MaNGA. Bundles are arranged in characteristic hexagonal formations. Note that the smallest bundle in this image, containing just 7 fibres, was used only for flux calibration and did not contribute to the sample of MaNGA galaxies (Bundy et al., 2015). Figure taken from Bundy et al. (2015, Figure 4).

minium plates, each of which was unique to a given target field (Bundy et al., 2015; Drory et al., 2015). Plates were assigned a unique four or five digit number; IFU bundles were also assigned a unique four or five digit number, the first digits of which indicate the number of fibres in the bundle. For instance, the MaNGA galaxy with the plate-IFU designation 7495-12704 was observed using the fourth 127-fibre IFU bundle, the fibres of which were plugged into plate 7495.

2.1.2 The Complete MaNGA Sample

The full sample of galaxies observed by the MaNGA survey comprises 10010 unique, detailed observations of candidate galaxies which were originally selected from an extended version of the NASA Sloan Atlas (NSA; Blanton et al., 2005, 2011) catalogue. The NSA catalogue is comprised of nearby ($z < 0.055$) galaxies from the SDSS DR7 MAIN galaxy sample (Abazajian et al., 2009); however, the requirements of MaNGA necessitated the extension of the base catalogue to include galaxies out to $z < 0.15$ (Wake et al., 2017). The criteria by which galaxies were chosen are introduced by Yan et al. (2016a), and are explained fully by Wake et al. (2017).

Two main factors were considered when constructing the MaNGA sample. Firstly, a roughly flat stellar mass distribution was desired from the sample galaxies² (Yan et al., 2016a; Wake et al., 2017); this ensured that the MaNGA sample

²In practice, the sample was actually selected to adhere to a flat distribution in the absolute i -band magnitude, since this quantity is a good proxy for stellar mass (Yan et al., 2016a; Wake et al., 2017). This was done in order to avoid model dependencies in stellar mass measurements. Absolute i -band magnitudes underwent K -corrections through the use of the software `kcorrect` (Blanton & Roweis, 2007) prior to the construction of the MaNGA sample.

comprised a sufficient number of high-mass galaxies in addition to their more numerous low-mass counterparts, which is an important consideration for those investigating mass-dependent trends (Wake et al., 2017). Secondly, spatial resolution was maximised while still capturing most of the light from the galaxies out to a certain radius (Yan et al., 2016a; Wake et al., 2017). In order to satisfy the latter criterion, a minimum redshift threshold was enforced in order to ensure that the angular size of $> 80\%$ of the sample galaxies did not exceed the footprint of the largest available IFU bundle (Wake et al., 2017; see below for more details). However, since (at a fixed distance) the luminosity of a galaxy is roughly proportional to the square of its angular size, it was necessary to raise the minimum redshift for target galaxies with higher K -corrected (Blanton & Roweis, 2007) absolute i -band magnitudes (Yan et al., 2016a). Accordingly, a maximum redshift threshold was also enforced in order to keep the number of galaxies in each redshift bin roughly constant (Yan et al., 2016a).

As a consequence, the MaNGA sample was inherently mass-biased: high-mass galaxies were over-represented and low-mass galaxies were under-represented by comparison to a standard volume-limited sample. Fortunately, this issue was easily remedied by assigning each of the sample galaxies a weight, the allocation of which allowed the sample to be statistically converted into a volume-limited, mass-complete one (Wake et al., 2017). High-mass galaxies were assigned small sample weights, and low-mass galaxies large sample weights.

We refer to this correction throughout this work as “volume-weighting”. In certain circumstances, such as when we wish to calculate average global quantities for the sample galaxies, it is necessary to correct for this mass bias to ensure that the sample is representative of the Universe as a whole.

The main MaNGA sample was split into three distinct subsamples, each of which is described below. Each of these subsamples are also shown on the luminosity–redshift plot of Figure 2.4 (Yan et al., 2016a).

1. *The Primary Sample:* This sample was designed to maintain uniform spatial coverage to 1.5 times the elliptical semi-major effective radius, R_e , for $> 80\%$ of the targets (Bundy et al., 2015). This effective radius threshold allowed most of the light from each system to be captured. The mean redshift of the Primary sample is $\langle z \rangle = 0.03$ (Bundy et al., 2015). 45.1% of the total observations made by MaNGA were used to build this sample of galaxies (Yan et al., 2016a).
2. *The Secondary Sample:* This sample was designed to maintain uniform spatial coverage to $2.5 R_e$ for $> 80\%$ of the targets, with a mean redshift of $\langle z \rangle = 0.045$ (Bundy et al., 2015). The Secondary sample comprised 35.7% of the total MaNGA galaxies (Yan et al., 2016a).

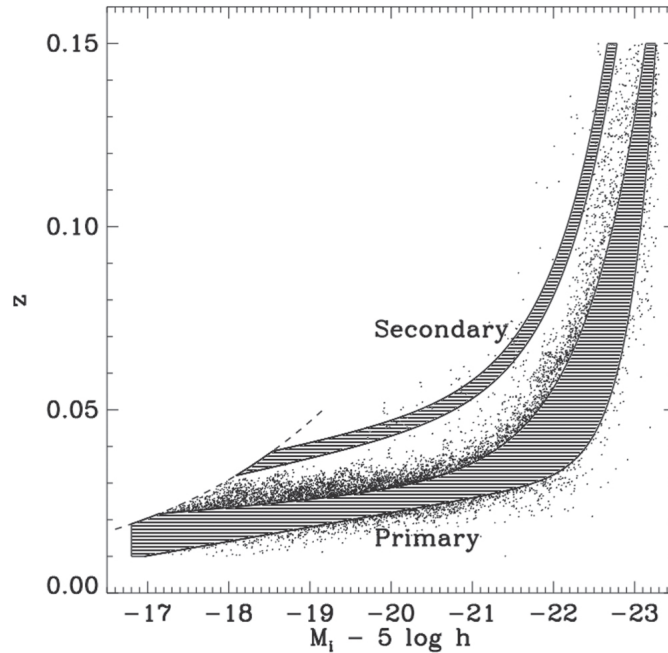


Figure 2.4: The three MaNGA subsamples (Primary, Secondary, and Colour-Enhanced) depicted on a plot of redshift versus luminosity. The two labelled shaded regions denote the general areas of the Primary and Secondary samples, and the dots indicate the individual galaxies which comprise the Colour-Enhanced sample. Figure taken from Yan et al. (2016a, Figure 1).

3. *The Colour-Enhanced Sample*: A further 15% of the target galaxies were selected for observation because they resided in sparsely populated regions of the colour–magnitude plane. These targets were predominantly “green valley” galaxies – i.e. mostly faint, red galaxies or bright, blue galaxies (Wake et al., 2017); such galaxies helped to balance the colour distribution at fixed stellar mass (Bundy et al., 2015). The Colour-Enhanced sample acquired coverage out to an effective radius of $1.5 R_e$. When combined with the base Primary sample, this sample formed the Primary+ sample.

The 4.2% of galaxies observed which do not belong to any of these three samples do not comprise the final MaNGA sample. These were either repeat observations of galaxies already in the MaNGA sample, or galaxies observed for ancillary projects unrelated to MaNGA. Almost all of the 10010 unique galaxies which comprised the MaNGA survey therefore only belonged to one of the Primary, Secondary, or Colour-Enhanced subsamples; these 10010 galaxies still, however, include a small number of galaxies observed in ancillary programmes.

The Primary+ sample comprised roughly twice as many galaxies as the Secondary sample. This was by design: covering galaxies to $2.5 R_e$ means that the Secondary sample contained higher redshift, but lower spatial resolution galaxies

than the Primary+ sample (see Figure 2.4; Yan et al., 2016a). Therefore, in order to balance the lower signal-to-noise ratio (S/N) and poorer spatial resolution associated with Secondary sample galaxies with the desire to capture a greater number of high-quality emission line spectra at larger radii, it was decided that the size of the Secondary sample should only constitute about one-third of the total observations made by MaNGA; the other two-thirds formed the Primary+ sample (Bundy et al., 2015; Yan et al., 2016a).

2.1.3 The Data Reduction Pipeline

Prior to analysis, the raw data produced by MaNGA had to be calibrated and reduced. This was done by the MaNGA Data Reduction Pipeline (DRP; Law et al., 2016), which performed both sky subtraction and spectrophotometric calibration, and finally reduced the data into a more usable format. Essentially, the DRP took all of the sky-subtracted, spectrophotometrically calibrated spectra obtained by each IFU fibre, and then reduced and combined these spectra into a single three-dimensional datacube. The key steps in the DRP framework are described in the subsections below.

2.1.3.1 Sky Subtraction

The first major DRP step was to subtract the residual sky flux from the raw spectra observed by MaNGA. Since the Secondary MaNGA sample obtained coverage of galaxies out to $2.5 R_e$, sky subtraction was particularly important: the flux in the outskirts of such galaxies was very likely to be on par with the sky background (Law et al., 2016). Furthermore, because it was likely necessary to stack spectra in order to observe faint emission and absorption lines in these regions, it was therefore critical to reach the level at which spectra were dominated by Poisson noise, as otherwise the stacked spectra would be limited by systematic sky subtraction uncertainties (Law et al., 2016). Poisson-limited performance was desired in the wavelength range $4000 - 10000 \text{ \AA}$.

To accomplish this, 92 dedicated, individually pluggable sky fibres were plugged into each observing plate in regions identified during the plate design process as being devoid of astronomical objects (see Figure 2.5; Law et al., 2016). This allowed a well-sampled model background sky to be constructed, which could then be subtracted from the spectra obtained by each of the science fibres (Law et al., 2016). Ultimately, almost Poisson-limited sky subtraction of the raw MaNGA spectra was achieved for wavelengths in the range $\lambda \lesssim 8500 \text{ \AA}$ (Law et al., 2016).

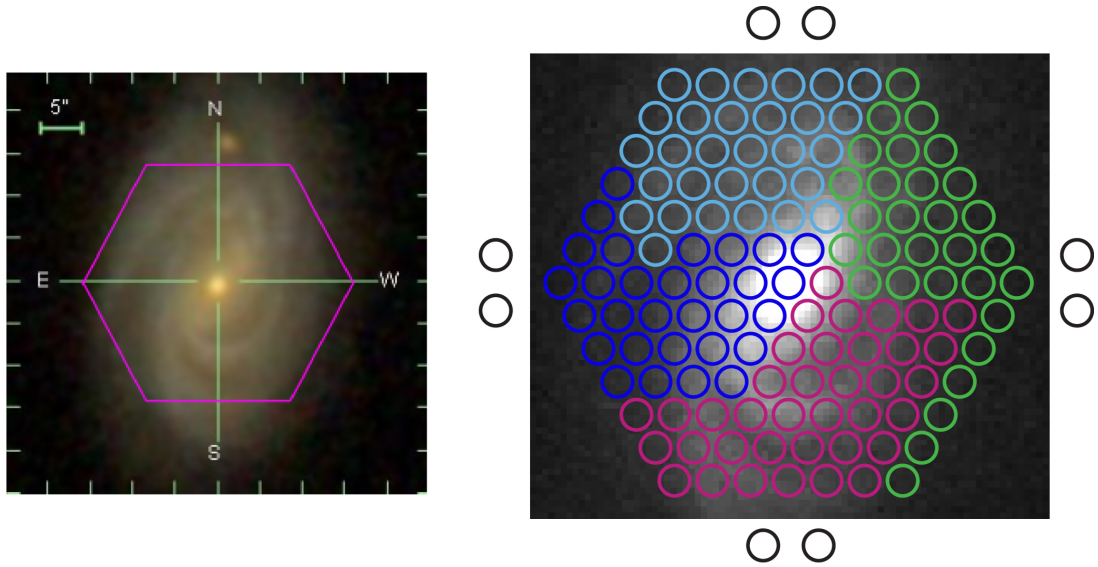


Figure 2.5: Left: 3-colour SDSS image of galaxy 7495-12704. Right: g -band image of the same galaxy. The coloured circles show the hexagonal arrangement of the 127 optical science fibres; the black circles indicate the positions of the 8 sky fibres. Figure taken from Law et al. (2016, Figure 1).

2.1.3.2 Spectrophotometric Calibration

Raw data obtained by MaNGA also had to be calibrated via spectral surface photometry at every spatial location sampled by each of the IFU fibres (Yan et al., 2016b). This calibration corrected the flux loss due to atmospheric throughput, as well as that lost due to instrument response (Yan et al., 2016b).

Importantly for this work, Yan et al. (2016b) set out to ensure that uncertainties arising from the spectrophotometric calibration processes were not the dominant source of error in important derived quantities, such as SFRs and gas metallicities. The proxy for gas metallicity that these authors chose to test the flux calibration of was the N2O2 ratio of Kewley & Dopita (2002). The N2O2 ratio is defined as $[\text{N II}] \lambda 6584 / [\text{O II}] \lambda \lambda 3727, 3729$ (Kewley & Dopita, 2002), and, conveniently, we shall also employ the N2O2 ratio as a gas metallicity proxy in Chapter 5 of this thesis. Yan et al. (2016b) evaluated the relative calibration accuracy of the $[\text{N II}] \lambda 6584$ and the $[\text{O II}] \lambda \lambda 3727, 3729$ emission lines, and found a root mean square (rms) fractional error of 4.7% on the relative calibration between these two emission lines.

Yan et al. (2016b) additionally measured the relative calibration accuracy of the ratio of the $\text{H}\alpha$ emission line to the $\text{H}\beta$ line. This is another emission line ratio whose accurate measurement is invaluable to this work, particularly when obtaining emission line dust attenuation measurements, and, in turn, when deriving dust-corrected SFRs of galaxies – as we endeavour to do in Chapter 3. The

rms fractional error on the relative calibration between $H\alpha$ and $H\beta$ was found to be just 1.7% (Yan et al., 2016b).

The level of precision in the relative calibrations in these two wavelength ratios guaranteed that flux calibration errors were not the dominant source of uncertainty on the derived quantities of gas metallicities and dust-corrected SFRs, respectively (Yan et al., 2016b). Finally, Yan et al. (2016b) determined that the absolute flux calibration on the raw spectrum from each IFU fibre had an rms fractional uncertainty of $< 5\%$ for 89% of the MaNGA wavelength range, which they identified as adequate for the science goals of MaNGA.

2.1.3.3 DRP Datacubes

The final major step of the DRP was to combine the individual spectra from each IFU fibre into a more usable format. The ultimate products of the sky subtraction (Section 2.1.3.1) and spectrophotometric calibration (Section 2.1.3.2) stages of the DRP were FITS files which contained the two-dimensional array of row-stacked spectra (RSS) for each of the MaNGA IFU fibres (Law et al., 2016). Each row in the RSS therefore corresponded to an individual spectrum. Upon completion of a certain number of exposures, the two-dimensional RSS for each IFU on a given plate were assembled into a master three-dimensional row-stacked datacube which contained all of the spectral information for a given MaNGA target (Law et al., 2016).

It was also important for the on-sky position of each IFU fibre to be calculated. This was done via the use of the DRP basic astrometry module (Law et al., 2016), which was able to generate arrays detailing the x and y fibre positions relative to the centre of the IFU. These arrays could then be utilised to determine effective on-sky locations for any wavelength and for any fibre. This astrometric information was used to combine individual fibre spectra into a rectified, rectilinearly gridded cube for each IFU (Law et al., 2016).

The flux maps at each wavelength channel were then reassembled into a single three-dimensional datacube per MaNGA target. Datacubes were constructed by combining image slices individually using a very similar method to that proposed by Shepard (1968). Each datacube stored the flux from the spectra obtained at every spatial pixel (or “spaxel”) for each of the MaNGA galaxies; the DRP datacubes thus possessed two spatial dimensions and one wavelength dimension. Corresponding datacubes of the inverse variance in flux, as well as mask datacubes (which denoted the positions of pixels for which data reduction failed), and broadband g , r , i , and z image cubes, were also produced for each galaxy (Law et al., 2016).

Law et al. (2016) noted that the redistribution of flux intensity measurements from individual fibres into the datacubes – as described above – resulted in signifi-

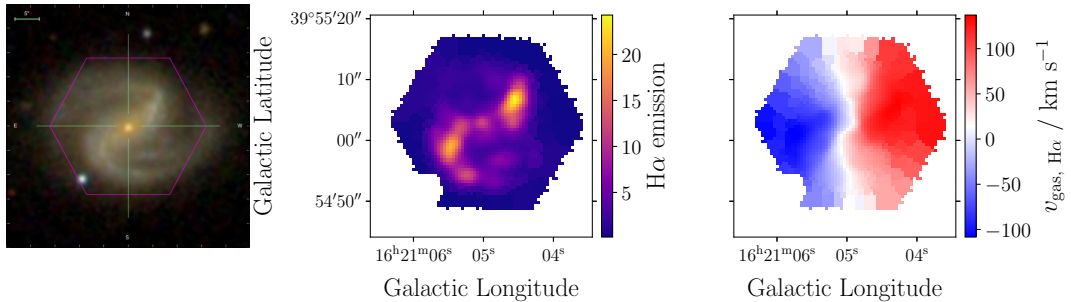


Figure 2.6: 3-colour SDSS image (left), map of $H\alpha$ emission line flux produced by the DAP (centre), and map of $H\alpha$ emission line gas velocity, $v_{\text{gas}, H\alpha}$, also produced by the DAP (right) for galaxy 8312-12702.

cant covariance among neighbouring pixels at each wavelength slice (see also Pace et al., 2019 and Law et al., 2021). Since this covariance had knock-on ramifications for the subsequent analysis of DRP datacubes, uncertainties due to covariance in individual spectra were propagated through to the final flux datacubes (Law et al., 2016). The full spatial covariance matrices were also included as part of the final DRP datacubes (Law et al., 2021).

2.1.4 The Data Analysis Pipeline

The MaNGA Data Analysis Pipeline (DAP; Westfall et al., 2019; Belfiore et al., 2019b) was conceived as a way to easily access the wealth of data in the products provided by the DRP. The DAP provided readily accessible, high-level, user-friendly maps of various analysis products, as illustrated in Figure 2.6. Such maps included stellar kinematics (velocities and velocity dispersions), emission-line properties (kinematics, fluxes, and equivalent widths), and spectral indices of the MaNGA galaxies (Westfall et al., 2019; Belfiore et al., 2019b). DAP maps could also be accessed, inspected, and downloaded using the Python package and web application **Marvin** (Cherinka et al., 2018).

DAP data products were constructed via the use of the penalized pixel-fitting (**pPXF**) routine (Cappellari & Emsellem, 2004; Cappellari, 2017). **pPXF** uses stellar template spectra from the Medium-resolution Isaac Newton Telescope Library of Empirical Spectra (MILES; Sánchez-Blázquez et al., 2006; Falcón-Barroso et al., 2011) to fit the continuum and stellar absorption lines; emission line spectra were fit using a series of Gaussian profiles (Westfall et al., 2019; Belfiore et al., 2019b).

The most relevant and crucial DAP products to this work are the various emission line maps of MaNGA galaxies. It is therefore important to note that prior to any analysis that we undertake in this work, the DAP had already subtracted

the stellar spectrum from the emission lines of each MaNGA spaxel (Westfall et al., 2019; Belfiore et al., 2019b). This process corrected each spectrum for stellar absorption, and thus ensured that we analysed purely the emission due to the gas in this work. Milky Way reddening is also already accounted for; the DAP employed the Fitzpatrick (1999) reddening law for this purpose (Westfall et al., 2019; Belfiore et al., 2019b)³.

2.2 Sample Selection of MaNGA Galaxies

Although a variety of different galaxy morphologies are surveyed by MaNGA, this work focuses exclusively on the properties and evolution of spiral galaxies. This is done for several reasons. Firstly, selecting a sample of galaxies based purely on their SFRs or colours could in reality mean that we end up building a sample of very different physical systems. However, studying only disk galaxies and excluding irregular galaxies from our analysis means that the distribution of stars, gas and dust within the galaxies is more regular, with a clearly defined disk and spiral arms. Selecting a sample of spiral galaxies is important for the work presented in Chapter 3, in which we want to test whether dust attenuation properties between the spiral arm and inter-arm regions of the galaxies exhibit any differences. Before undertaking this investigation, we must, therefore, also ensure that we exclude any lenticular (S0) galaxies from our sample. Moreover, in Chapter 4 our ultimate goal is to place the distribution of stellar metallicity of the Milky Way metallicity data in context; therefore, we need to select a sample of comparable spiral galaxies from the full MaNGA data set.

It is therefore imperative to select a representative sample of unequivocally spiral galaxies from the full MaNGA sample. In order to do so, we make use of classifications provided by the citizen science project Galaxy Zoo 2 (GZ2; Masters et al., 2011; Willett et al., 2013). The process that we follow is outlined in Peterken et al. (2020); we describe the selection criteria in full in Section 2.2.1. In order to analyse differences between the spiral arm and inter-arm regions of the galaxies, we additionally make use of data from Galaxy Zoo: 3D (GZ:3D; Masters et al., 2021); we therefore devote Section 2.2.2 to an explanation of this project and how the use of GZ:3D data affects our sample selection.

One final important point to note is that MaNGA was still observing galaxies when this work commenced. Therefore, the base MaNGA galaxy samples from which we draw upon are different in each of Chapters 3, 4, and 5. The internal release of data to the MaNGA collaboration was referred to as a ‘‘MaNGA Product Launch’’ (MPL); each successive MPL contained completed observations for a progressively larger number of galaxies. Chapter 3 uses data from MPL-8 (6293

³Prior to the release of MaNGA Product Launch 8, the reddening law of O’Donnell (1994) was used by the DAP. However, we do not employ pre-MPL-8 DAP products in this work.

galaxies; Law et al., 2021); Chapter 4 uses data from MPL-9 (7823 galaxies; Law et al., 2021); and Chapter 5 uses data from the final data release, MPL-11 (10010 galaxies). The full MPL-11 sample is now publicly available thanks to SDSS DR17 (Abdurro’uf et al., 2022). Fortunately, since MaNGA carried out observations in a largely random order, and because the subsamples used in this work are large, it is worth noting that none of the results in the rest of this thesis depends sensitively on the MPL used.

2.2.1 Galaxy Zoo 2

Launched in July 2007, Galaxy Zoo (GZ; Lintott et al., 2008, 2011) was a project that provided visual morphological classifications for hundreds of thousands of SDSS galaxies. Volunteer “citizen scientists” were invited to visually inspect and classify individual galaxies via the internet. The result was a robust consensus on various morphological properties of these galaxies. The second iteration of this project, GZ2 (Masters et al., 2011; Willett et al., 2013), provided more detailed visual classifications than its predecessor by asking volunteers additional questions about a subsample of the original GZ galaxies. The galaxies classified by GZ2 were taken from SDSS DR7 (Abazajian et al., 2009).

Unlike the original GZ project, GZ2 employed a multi-step decision tree of questions in order to classify galaxies, which allowed a greater depth of morphological information to be gleaned about the galaxies (Willett et al., 2013). Each individual step in the tree asked of the volunteer a multiple-choice question, upon which the user was required to “vote”. Each user completed one decision tree per galaxy. Previous authors have already exploited the wealth of information provided by GZ2, using classifications to study particular morphological features of spiral galaxies, such as their bars (e.g. Masters et al., 2011; Cheung et al., 2013; Fraser-McKelvie et al., 2019, 2020a); their bulges (e.g. Simmons et al., 2013; Hart et al., 2018; Tabor et al., 2019); and, most pertinent to this work, their spiral arms (e.g. Willett et al., 2015; Hart et al., 2017a,b, 2018; Peterken et al., 2020).

We now discuss the process by which subsamples were constructed in this work using GZ2 classifications. The numbers below pertain only to the final MPL-11 data set (used for data analysis in Chapter 5); however, the exact same procedure is used to draw subsamples from the MPL-8 and MPL-9 data sets employed in Chapters 3 and 4, respectively. The reasoning behind the method adopted here is described in more detail by Willett et al. (2013) and Hart et al. (2016).

Of the 10010 total observations in MPL-11, GZ2 classifications are available for 9315 galaxies. These classifications were made publicly available in a Value Added Catalogue (VAC) with the release of SDSS DR15 (Aguado et al., 2019). The first step is to remove from this sample 81 galaxies which are obscured by a star or other artifact. Then, to ensure we are only selecting spiral galaxies, we choose only those

for which $> 43\%$ of $N \geq 20$ respondents observed either spiral features or a disk in the galaxy (as recommended by Willett et al., 2013). This cut reduces the sample to 6727 candidates that may be spiral galaxies. Since we wish our sample to be comprised of unequivocally spiral galaxies, we also want to select only those that are oriented reasonably face-on. In addition to requiring that $> 80\%$ of $N \geq 20$ respondents determine that each galaxy is not edge-on (Willett et al., 2013), we also select only those galaxies which have a photometric axis ratio of $\frac{b}{a} \geq 0.5$ (corresponding to an inclination of $i \geq 60^\circ$). The photometric axis ratios of the sample galaxies are taken directly from the NSA catalogue (Blanton et al., 2005, 2011), and are derived from r -band elliptical Petrosian aperture measurements. This constraint upon galaxy orientation is somewhat stricter than that proposed by Hart et al. (2017a), and further reduces the sample size to 2081 reasonably face-on spiral galaxies. Finally, we reject any galaxies that were flagged for poor data quality by the DRP or had for any reason failed to produce the necessary DAP data sets. This leaves a final sample comprising 1619 reasonably face-on spiral galaxies that are fit for analysis. These 1619 galaxies are analysed later in Chapter 5.

The same procedure yields a subsample of 1205 MPL-8 galaxies (out of a total of 6293), which forms the initial sample used Chapter 3; and a subsample of 1475 MPL-9 galaxies (out of a total of 7823), which comprises the final sample used in Chapter 4. Finally, to ensure that the individual spaxels used for analysis in this work were of a sufficiently high quality, a minimum continuum S/N cut of 10 or higher was imposed; spaxels below this threshold were discarded prior to analysis.

2.2.2 Galaxy Zoo: 3D

Previous Galaxy Zoo projects, including both the original GZ and its successor, GZ2, focused on asking relatively simple questions – such as, for example, whether bars or spiral arms were present or absent in galaxies. By contrast, the GZ:3D (Masters et al., 2021) project was more detailed in scope; volunteers were asked not only whether these features were present, but also where exactly the bars or spiral arms were located in each galaxy. Respondents were asked to identify the arms and bars of spiral galaxies with the aid of a freehand drawing tool, which these volunteers used to decide how best to enclose these features in SDSS images.

GZ:3D ultimately provided crowd-sourced masks for the bars and spiral arms of 29831 galaxies, of which 9188 were observed by MaNGA (Masters et al., 2021). When coupled with the DAP maps produced by MaNGA (described in Section 2.1.4), these masks denoted which of the MaNGA spaxels comprised part of (for instance) the spiral arms of a given galaxy, as can be seen in Figure 2.7. Previous authors have already successfully employed both the bar masks (e.g. Fraser-McKelvie et al., 2019, 2020a; Krishnarao et al., 2020) and the spiral arm masks (e.g. Peterken et al., 2019a,b) in conjunction with MaNGA data.

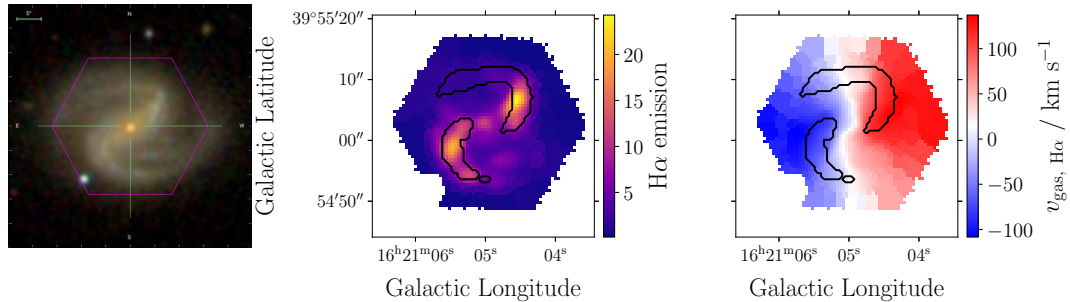


Figure 2.7: As Figure 2.6, showing the same 3-colour SDSS image and example DAP maps for galaxy 8312-12702, except that these maps are now overlaid with spiral arm masks (black) produced by the GZ:3D project (Masters et al., 2021).

In Chapter 3, we present our own work in which we utilise the spiral arm masks provided by the GZ:3D project to investigate variations between the spiral arm and inter-arm regions of a sample of MaNGA galaxies. Although GZ:3D masks for almost the full MPL-11 MaNGA sample have recently been made publicly accessible (Masters et al., 2021), the GZ:3D project was still ongoing at the time that the research presented in Chapter 3 was undertaken. As a result, GZ:3D spiral arm masks were, at the time, only available for a subset of MPL-5 galaxies (SDSS DR14; Abolfathi et al., 2018). Only 2812 galaxies had been observed upon the release of MPL-5; furthermore, GZ:3D also required that more than half of the GZ2 respondents marked each of these galaxies as having either spiral arms or a bar. Moreover, galaxies in GZ:3D were also subject to all of the various GZ2 sample selection criteria outlined in Section 2.2.1 (see also Willett et al., 2013; Hart et al., 2016). This meant that, at the time of our publication, GZ:3D spiral arm masks were available for only 294 MPL-5 MaNGA galaxies, even though, as discussed in Section 2.2.1, our sample size ostensibly constituted 1205 galaxies from the much larger MPL-8 data release. This number was further reduced to just 247 galaxies upon the exclusion of any galaxies with DAP datacube poor quality flags. This subsample of 247 MPL-8 galaxies (out of a total of 6293) forms the basis of the sample used in Chapter 3.

Despite this smaller sample size, selecting only the GZ:3D spirals has two further advantages for the work we undertake in Chapter 3. First, almost all GZ:3D spirals are close to face-on, as a result of volunteers determining the location of spiral arms more readily in face-on galaxies than in edge-on galaxies. Consequently, it is easier to consistently compare dust attenuation properties of different galaxies within this sample, since the variation of inclination from galaxy to galaxy is small. Moreover, choosing purely GZ:3D spirals ensures that each galaxy has well-defined spiral arms, reducing ambiguity in subsequent analysis.

2.3 Full-Spectrum Stellar Population Fitting

Much of the work presented in this thesis requires fitting the MaNGA spectra with a set of template spectra in order to investigate how the properties of the sample galaxies depend on both age and metallicity. In order to obtain this information, we make use of the full-spectrum stellar population fitting code `STARLIGHT` (Cid Fernandes et al., 2005). We explain our rationale for our decision to use `STARLIGHT` over the plethora of other spectral fitting codes in Section 2.3.1. Section 2.3.2 details exactly how `STARLIGHT` was implemented to obtain much of the data used in this work. Finally, Section 2.3.3 describes methods by which the certain aspects of the `STARLIGHT` fitting procedure were tested.

2.3.1 Why STARLIGHT?

There are several publicly available spectral fitting codes from which to choose. Our justifications for using `STARLIGHT` are as follows:

1. Certain stellar population fitting algorithms – such as Bayesian Analysis of Galaxies for Physical Inference and Parameter ESTimation (`BAGPIPES`; Carnall et al., 2018), Code Investigating GALaxy Emission (`CIGALE`; Boquien et al., 2019), and `SNITCH` (Smethurst et al., 2019) – are parametric in nature: they impose assumptions on the shape of the star formation history that we wish to measure, which we wish to avoid in this work. By contrast, `STARLIGHT` is fully non-parametric. Parametric fitting codes are computationally fast, but the choice of star formation history shape can severely bias the fitting results (e.g. Lee et al., 2009, 2010; Maraston et al., 2010; Pforr et al., 2012). Although non-parametric algorithms – such as `STARLIGHT` and `pPXF` (Cappellari & Emsellem, 2004; Cappellari, 2017) – have many more degrees of freedom, which can potentially lead to unconstrained fits and degeneracies, different non-parametric codes are found to yield generally consistent results (e.g. Cid Fernandes et al., 2005; Li et al., 2017; de Amorim et al., 2017; Cid Fernandes, 2018).
2. `STARLIGHT` had already been “battle-tested” when this work commenced: it has been successfully utilised by several previous authors to analyse the stellar populations of galaxies observed by both `CALIFA` (e.g. Pérez et al., 2013; Cid Fernandes et al., 2013, 2014; González Delgado et al., 2017; García-Benito et al., 2019) and `MaNGA` (e.g. Mallmann et al., 2018; Peterken et al., 2019a,b, 2020; Fraser-McKelvie et al., 2020b). More recently developed codes – such as `PIPE3D` (Sánchez et al., 2016a,b) and `Fitting Iteratively For Likelihood analysis` (`FIREFLY`; Wilkinson et al., 2017) – lacked this benefit when this work began.

3. In this work, we are interested in the robust analysis of stellar populations, which STARLIGHT is specifically designed for. We do not study the kinematics of galaxies, which fitting software such as pPXF and PIPE3D specialise in.
4. STARLIGHT has two further advantages over pPXF. Firstly, it is very flexible in its configuration, and this can also be easily altered upon setup. Secondly, STARLIGHT fits the shape of the MaNGA continuum in addition to all absorption lines, which is crucial to the accurate retrieval of stellar population information. pPXF struggles to compete with STARLIGHT in both of these instances.
5. Finally, we already had easy access to a huge set of best-fit spectra when this project began, thanks to concurrent work undertaken by Peterken et al. (2020). These authors had, via the implementation of STARLIGHT, already produced the best fit spectra for the individual spaxels of 1205 MPL-8 galaxies when the work presented in this thesis commenced. It was therefore logical to expand our analysis to the later sample of 1619 MPL-11 galaxies using the same software as Peterken et al. (2020).

2.3.2 Spectral Fitting with STARLIGHT

STARLIGHT uses Monte Carlo techniques to derive best-fit spectra for the input spectra of each of the spaxels in the sample galaxies, with no assumptions made on the shape of the derived star formation histories. Each best-fit spectrum is created from a linear combination of a set of input single stellar population (SSP) template spectra and an applied dust attenuation. An SSP spectrum models the average behaviour of a population of stars at a given chemical composition. Therefore, the SSP spectrum can be used to model how a population of a certain metallicity appears after an arbitrary time interval since an instantaneous burst of star formation. Observational stellar spectra are combined with model isochrones (which indicate the positions of a population of a given age on the Hertzsprung-Russell diagram – see Figure 1.3) and an assumed IMF to construct the template SSP spectra (see, for instance, Vazdekis et al., 2010, 2016). For examples of some of the SSP spectra used in this work, see Figure 2.8.

The fitting method we employ in this work is described fully by Peterken et al. (2020); below, we highlight the key relevant details.

Before fitting each spaxel’s spectrum, emission lines are removed using the MaNGA DAP (Westfall et al., 2019; Belfiore et al., 2019b). No binning of neighbouring spaxels is done, since we wish to fully retain all spatial information. Each of the MaNGA spectra are fitted using a linear combination of SSP templates from the E-MILES library of Vazdekis et al. (2016), which in turn is based on the earlier MILES library of Vazdekis et al. (2010). During the fitting procedure, we

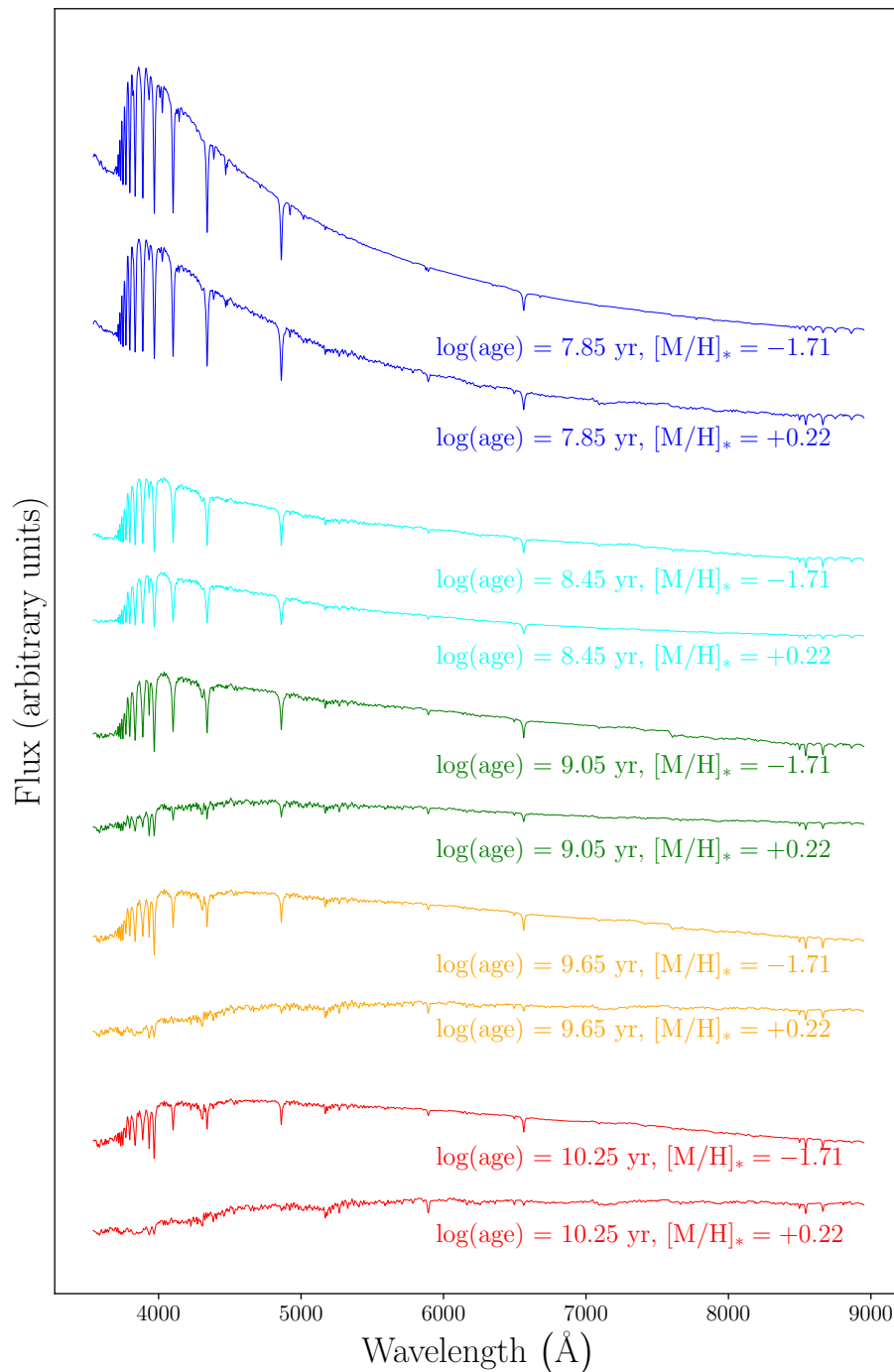


Figure 2.8: The shape of the template SSP spectra from the E-MILES library of Vazdekis et al. (2016) for stellar populations at a range of different ages and metallicities. The vertical axis, showing the flux of the stellar spectra, is somewhat arbitrary as the fluxes of the older populations have been multiplied by different amounts, so that features in their spectra are visible. Additionally, spectra are offset from each other by arbitrary amounts for the sake of clarity.

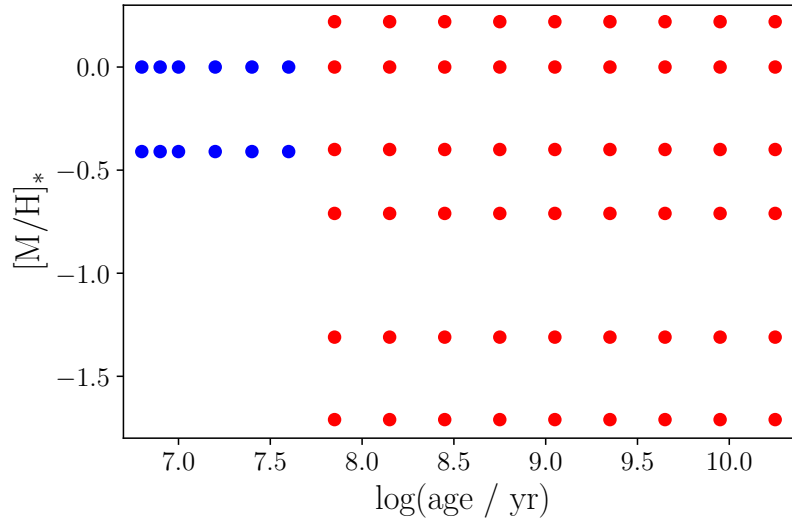


Figure 2.9: The locations in stellar metallicity–age parameter space of the template SSPs used in the spectral fitting procedure. Red points denote the 54 SSPs used from the E-MILES library of Vazdekis et al. (2016); blue points denote the 12 SSPs used from the library of Asa’d et al. (2017).

adopt a Chabrier (2003) IMF, the “Padova” isochrones of Girardi et al. (2000), and a Milky Way $[\alpha/\text{Fe}]$ (“baseFe”).

The 54 E-MILES templates constitute nine ages ($\log(\text{age}/\text{yr}) = 7.85, 8.15, 8.45, 8.75, 9.05, 9.35, 9.65, 9.95, 10.25$) and six metallicities ($[\text{M}/\text{H}]_* = -1.71, -1.31, -0.71, -0.40, +0.00, +0.22$). A selection of these E-MILES template spectra are plotted in Figure 2.8. To reproduce younger stellar populations, we include an additional 12 SSP templates with six ages ($\log(\text{age}/\text{yr}) = 6.8, 6.9, 7.0, 7.2, 7.4, 7.6$) and two metallicities ($[\text{M}/\text{H}]_* = -0.41, +0.00$) from the library of Asa’d et al. (2017). These younger templates are produced in the same way as the E-MILES templates, except the (very similar) isochrones of Bertelli et al. (1994) are used instead. The full stellar metallicity–age parameter space occupied by the template spectra is shown in Figure 2.9.

The result of the **STARLIGHT** fitting process is a set of weights for the mass contributions of SSPs with different ages and chemical compositions to the light seen in the spectrum of each spaxel across the face of a galaxy. From these weights, we subsequently derive stellar metallicity distributions for the sample galaxies in Chapter 4, as well as the star-formation histories of the same galaxies, which form the basis of the work presented in Chapter 5.

Additionally, when building a best-fit spectrum from the SSPs, **STARLIGHT** also fits a dust attenuation $A_{V, \text{stars}}$, for which a Calzetti et al. (2000) attenuation curve is assumed. In doing so, **STARLIGHT** provides us with reliable values for the dust attenuation affecting the stellar populations for every star-forming spaxel in each

of the sample galaxies. These values are utilised in Chapter 3 in our investigation of spatially resolved dust attenuation in spiral galaxies.

2.3.3 Tests and Improvements

There are certain instances where deficiencies in the **STARLIGHT** fitting procedure may affect the results of this work. Fortunately, Peterken et al. (2020) have extensively tested these problems, and in doing so provided a convenient checklist to ensure that we are not ensnared by various pitfalls in the fitting process. Here we discuss the tests performed by Peterken et al. (2020) that are relevant to this work.

The **STARLIGHT** mass weights allow an alternative calculation for the stellar masses of the MaNGA galaxies to those provided by the DRP (see Section 2.1.3), which in turn are taken from the NSA catalogue (Blanton et al., 2005, 2011). The NSA stellar mass estimates are derived from elliptical Petrosian photometry via the software **kcorrect** (Blanton & Roweis, 2007), and assuming a Chabrier (2003) IMF (see Fraser-McKelvie et al., 2019 for an in-depth discussion on obtaining stellar mass estimates for SDSS galaxies). We find that the stellar masses calculated from the **STARLIGHT** mass weights are systematically slightly higher than those in the NSA catalogue, as can be seen in Figure 2.10. This is because we include the mass weight contributions from all of the MaNGA spaxels; if, as Peterken et al. (2020) recommend, we consider only the contributions from spaxels with galactocentric radius $R \leq 1.2 R_e$, thus limiting sky background contamination, we find good agreement between the two methods. Including the mass weight contributions out to only $R \leq 1.2 R_e$ avoids the edges of the hexagonal IFU footprints, as well as ensuring consistency between galaxies.

We also use the **STARLIGHT** configuration settings which prioritise robustness over computation times, following the recommendations of Ge et al. (2018) and Cid Fernandes (2018), and as fully described and tested by Peterken et al. (2020, including Appendix A). Additionally, since emission lines in the MaNGA spectra are well-modelled by the DAP, we use **STARLIGHT** in a mode which fully fits the spectral absorption lines. We require **STARLIGHT** to retain $\geq 97\%$ of the total light during the fitting process, and we also request that the final fit assigns mass (and light) weights to $\geq 30\%$ of the template spectra, again using the **STARLIGHT** configuration settings employed by Peterken et al. (2020). These criteria allow the star formation history of each spaxel to be determined accurately and robustly.

Finally, additional tests performed by Peterken et al. (2020) found significant correlation between the **STARLIGHT** mass weights for SSP templates with ages $\lesssim 10^{7.2}$ yr and $\gtrsim 10^{9.5}$ yr, which is not only unphysical (e.g. Schönrich & Binney, 2009), but also results in a sudden spike in the derived star formation histories of the galaxies at $\sim 10^{7.2}$ yr. Similar effects are also observed by Cid Fernandes &

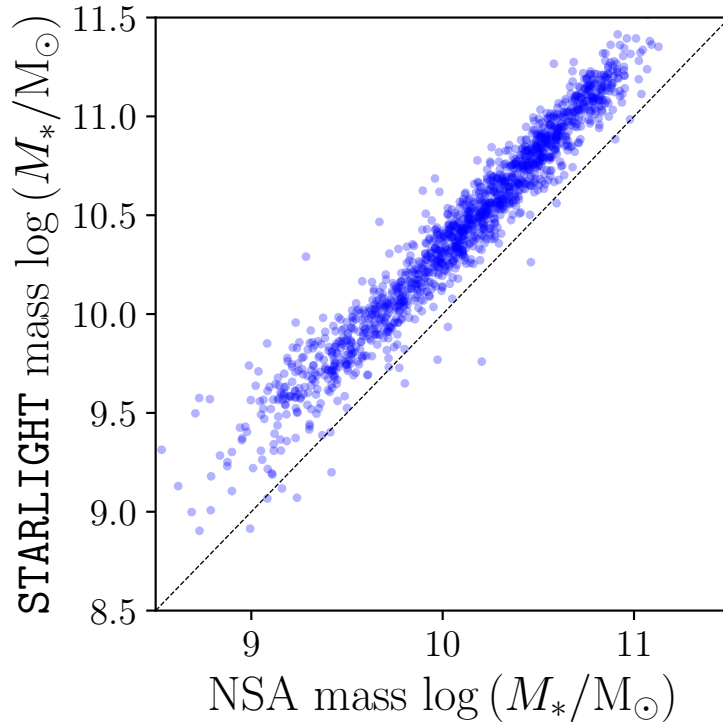


Figure 2.10: A comparison of stellar masses for MPL-11 galaxies from the NSA catalogue, obtained by elliptical Petrosian photometry (Blanton et al., 2005, 2011, horizontal axis); and derived from the **STARLIGHT** mass weights (vertical axis). The dashed black line is a 1-to-1 relation, and does not represent a fit to the data.

González Delgado (2010), and Peterken et al. (2020) argue that this phenomenon may be related to the “UV upturn” arising from planetary nebulae in old stellar populations (see, for instance, Yi, 2008). Since the template spectra of these old populations do not account for this UV radiation, **STARLIGHT** erroneously assigns this light to the young stars at $\sim 10^{7.2}$ yr, the flux from whose spectra dominates at such wavelengths. Therefore, following the advice of Peterken et al. (2020), we ignore the best fit spectra for stellar populations with template ages younger than $10^{7.5}$ yr (~ 30 Myr) in the subsequent analysis of this work. On a more positive note, the testing undertaken by Peterken et al. (2020) ultimately finds that populations with ages older than $10^{7.5}$ yr, are, by contrast, robust, reliable, and safe to use.

2.4 Applications of MaNGA Data in this Work

In summary, we make use of the veritable treasure trove of IFU data obtained by the SDSS-IV MaNGA survey throughout this thesis. These raw data are reduced and calibrated by the DRP, which provides three-dimensional datacubes containing all of the spatial and spectral information for each of the galaxies observed by MaNGA. The DAP then converts the DRP datacubes into high-level maps of various data products, the most salient of which to this work are the emission line maps of the MaNGA galaxies. These emission line maps will be employed in both Chapters 3 and 5 in order to investigate the spatially resolved dust attenuation and gas metallicities of spiral galaxies, respectively.

In order to construct samples of well-defined spiral galaxies in this work, we use selection criteria based upon the classifications made by the GZ2 project in each of Chapters 3, 4 and 5. Furthermore, in order to closely analyse the spiral arms of galaxies in Chapter 3, we additionally make use of classifications provided by the GZ:3D project in this Chapter.

Throughout this thesis, we rely on the full-spectrum stellar population synthesis code `STARLIGHT` to provide us with analysis of the stellar populations of the MaNGA galaxies. We use the data products provided by `STARLIGHT` in a multitude of different ways. In Chapter 3, we use the dust attenuation values that are a by-product of the `STARLIGHT` fitting process as the core basis for our research. In Chapter 4, we use the `STARLIGHT` mass weights to construct stellar metallicity distribution functions for the sample of spiral galaxies. Finally, in Chapter 5 we use these same mass weights to determine both the star formation histories and stellar metallicity histories of the MaNGA galaxies.

Chapter 3

Spatially Resolved Dust Attenuation in Spiral Galaxies

3.1 Introduction

Properties of galaxies such as gas metallicities and star formation rates (SFRs) are derived from nebular emission lines produced as a result of gas heated by star-forming regions. However, this light at optical and ultraviolet (UV) wavelengths is absorbed and scattered by dust grains between the emission source and the observer, which results in dust attenuation.¹ We refer the reader to Kewley et al. (2019) and Salim & Narayanan (2020) for recent reviews on emission lines and dust attenuation respectively, and Calzetti (2001) for a pioneering study on dust within star-forming galaxies. Star-forming spiral galaxies are undergoing dynamical and structural evolution (see reviews in Boselli & Gavazzi, 2006 and Sánchez, 2020), and are often associated with regions with considerable SFRs (e.g. Roberts, 1969; Kennicutt, 1998; Boselli & Gavazzi, 2006; Sánchez, 2020). These findings are of particular interest for this work, as SFRs are often correlated with the total dust content of star-forming galaxies (e.g. da Cunha et al., 2008, 2010; Rowlands et al., 2014; Rémy-Ruyer et al., 2015).

Ultimately, we want to better understand the nature of interstellar dust, and how it affects astronomical observations. The motivation for doing so is compelling. The dust content of galaxies has been shown to correlate with their gas metallicities and gas contents (Calzetti, 2001), but its presence reduces and reddens both the UV and optical flux emerging from host galaxies. This effect results in biased measurements of SFRs (Madau et al., 1996; Steidel et al., 1999; Glaze-

¹*Extinction* is defined as absorption + scattering by dust grains out of the observer's line of sight. This phenomenon is not to be confused with *attenuation*, which is absorption + scattering into and out of the observer's line of sight. These terms are often erroneously used interchangeably – see Figure 3.1 (Salim & Narayanan, 2020) for further clarification.

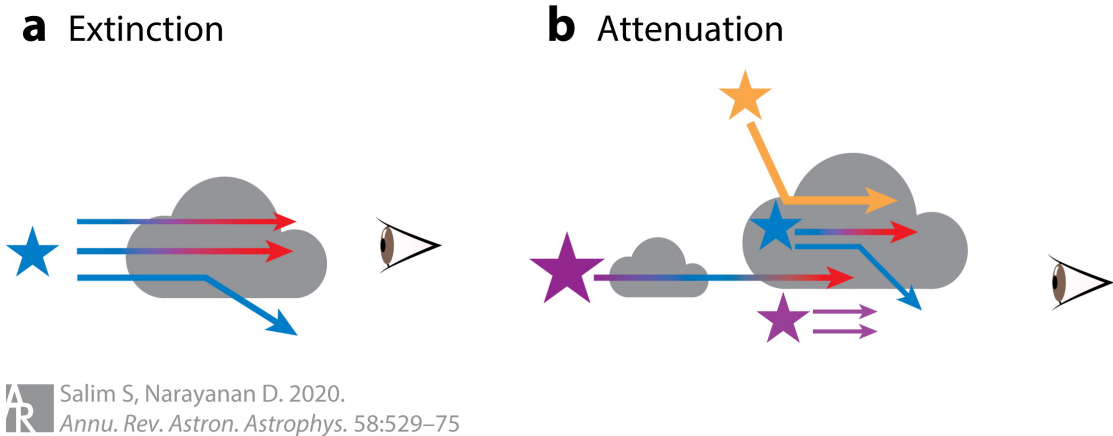


Figure 3.1: Schematic diagram showing the difference between dust extinction (absorption + scattering out of the observer’s line of sight), and dust attenuation (absorption + scattering into and out of the observer’s line of sight). Figure taken from Salim & Narayanan (2020, Figure 1).

brook et al., 1999; Sullivan et al., 2000; Bell & Kennicutt, 2001; da Cunha et al., 2010), SFRs per unit physical surface area (Buat et al., 1989; Kennicutt et al., 2007; Li et al., 2019), SFR densities (Brinchmann et al., 2004), specific SFRs (Buat et al., 2006; Pannella et al., 2009), gas metallicities (Gilbank et al., 2010; Wilkinson et al., 2015), mass and luminosity densities (Brinchmann et al., 2004; Driver et al., 2007), and even distance estimates (Giovanelli et al., 1995).

As discussed in Section 1.2.3 (and references therein), models of dust attenuation usually consider two main components in spiral galaxies: (1) *an interstellar medium (ISM)*, which is diffuse and increases in density closer to the galactic centre; and (2) *birth clouds*, in which dust is very highly concentrated, clumpy, and therefore optically thicker than the ISM. Over time, the older stars migrate away from these clouds, meaning that only the young, hot O and B stars remain in close proximity to their birth clouds (e.g. Walborn et al., 1999; Sellwood & Binney, 2002; Roškar et al., 2008; Minchev & Famaey, 2010; Loebman et al., 2010; Frankel et al., 2018; Minchev et al., 2018; Feltzing et al., 2020). These massive, young stars then ionise the surrounding gas, forming H II regions within the birth clouds. The central star-forming region is surrounded by clumps of gas and dust – propelled outwards by outflows from the starburst site – which absorb both continuum photons and those from the H II regions alike (Charlot & Fall, 2000; Calzetti, 2001).

Previous authors (e.g. Fanelli et al., 1988; Storchi-Bergmann et al., 1994; Calzetti et al., 1994, 2000; Kreckel et al., 2013) have extensively quantified and compared two independent measures of dust attenuation. Firstly, measurements of the ratio of the Balmer emission lines $H\alpha$ to $H\beta$ are used as a diagnostic to derive the dust attenuation in the gas. The ratio of $H\alpha$ to $H\beta$ is known as the Balmer

decrement. Since both lines are produced by the recombination of gas ionised by young stars, the Balmer decrement provides a measure of the dust attenuation due to the clumpy birth clouds, and so is useful to map the distribution of these dust clumps within the star-forming galaxies. The second measure is of the dust attenuation affecting the stellar populations. The gas is associated with the young stars close to the plane of the host galaxies, where dust is concentrated; the stars, by contrast, have a much greater scaleheight on average. Furthermore, since the dust and gas are well-mixed, we therefore might expect the dust attenuation in the gas to be higher than that affecting the stellar populations. Previous work, in which the ratio of these two dust attenuation measures has been calculated, has determined that this is indeed the case (e.g. Fanelli et al., 1988; Storchi-Bergmann et al., 1994; Calzetti et al., 1994, 2000; Kreckel et al., 2013).

The measurements made by many of these previous authors, are, however, limited by a lack of spatial resolution. Fortunately, integral field spectroscopic surveys, such as the Calar Alto Legacy Integral Field Area (CALIFA; Sánchez et al., 2012) survey, the Multi Unit Spectroscopic Explorer Wide (MUSE-Wide; Urrutia et al., 2019) survey, and the largest such survey, Mapping Nearby Galaxies at Apache Point Observatory (MaNGA; Bundy et al., 2015), now allow for spatially resolved observations of nearby spiral galaxies with a representative range of masses and SFRs. Such observations provide spatially resolved measurements for each of the dust attenuation derived from the gas, the dust attenuation affecting the stellar populations, and the excess between the former quantity and the latter. This final metric is perhaps a more physically meaningful property than the ratio between the two dust attenuation measures determined by previous studies, since it quantifies the excess dust attenuation close to the plane of the galaxy.

In this Chapter, we quantify the dust attenuation in a well-defined sample of 232 nearby star-forming spiral galaxies with the aid of integral field spectroscopy. Two independent, but complementary, methods are used: first by using the emission line ratio of $H\alpha$ to $H\beta$ as a diagnostic for the dust attenuation in the gas, and second by using full-spectrum stellar population fitting methods to measure the dust attenuation affecting the stellar populations in the same galaxies.

We shall use this analysis to propose a new geometry for the dust distribution in star-forming spiral galaxies, as well as putting better constraints on the difference between the optical depth of the $H\alpha$ and $H\beta$ Balmer emission lines, and that affecting the stellar continuum. It is relatively easy to use measurements of these Balmer lines to determine the dust attenuation in low-redshift galaxies (e.g. Sullivan et al., 2000; Bell & Kennicutt, 2001; Kreckel et al., 2013) and in high-redshift galaxies (e.g. Glazebrook et al., 1999). For low-redshift galaxies, while the attenuation affecting the stellar populations can also be readily measured (e.g. Sullivan et al., 2000; Kreckel et al., 2013), this measurement becomes increasingly difficult for more distant galaxies (e.g. Madau et al., 1996). A robust conversion factor between the two dust attenuation metrics, such as is calculated in this work,

is therefore an invaluable tool for observing distant galaxies.

This Chapter is structured as follows. Section 3.2 recaps the MaNGA and Galaxy Zoo: 3D data that are used in this work. Section 3.3 describes the methods implemented to quantify dust attenuation, and Section 3.4 explains the different ways in which we categorise galaxies for analysis in this work. In Sections 3.5 and 3.6, we present the results and subsequent discussion of this work for both global and spatially resolved measurements of dust attenuation, respectively. Finally, we propose a new geometry for dust in spiral galaxies in Section 3.7 and draw our conclusions in Section 3.8.

3.2 Sample Selection

As discussed in Section 2.2, we make use of MaNGA data from the MPL-8 data release. MPL-8 contained completed observations of 6293 MaNGA target galaxies. Upon implementing various selection criteria based upon Galaxy Zoo 2 (Willett et al., 2013; see also Hart et al., 2016) classifications described in Section 2.2.1, we are left with a subsample of 1205 MPL-8 spiral galaxies, all of which are oriented reasonably face-on. This subsample is further reduced in size to just 247 galaxies for which Galaxy Zoo: 3D (GZ:3D; Masters et al., 2021) spiral arm masks are available, as explained in Section 2.2.2. Though fairly small, this sample is comprised entirely of unequivocally spiral galaxies with well-defined spiral arms.

Finally, we also exclude from our analysis an additional 15 galaxies which only had $H\alpha$, $H\beta$, $[O\ III]\ \lambda 5007$ or $[N\ II]\ \lambda 6583$ signal data for $< 5\%$ of their spaxels. This leaves us with the final sample of 232 spiral galaxies that we analyse in this work. Individual spaxels within these 232 galaxies which lacked signal data for any of the above emission lines were also rejected.

3.3 Measures of Dust Attenuation

We consider the dust attenuation due to the clumpy birth clouds as well as that due to the diffuse ISM in this Chapter. In this Section, we discuss the methods by which the dust attenuation from both the birth clouds (Section 3.3.1) and the ISM (Section 3.3.2) are measured.

3.3.1 Emission Line Ratios

In this work, we use measurements of the $H\alpha$ emission line at $6563\ \text{\AA}$ and the $H\beta$ emission line at $4861\ \text{\AA}$ in order to calculate the dust attenuation due to the presence of clumpy birth clouds associated with the youngest stellar populations

in the sample of MaNGA spirals. Measuring the ratio of $H\alpha$ to $H\beta$, or the “Balmer decrement”, of a given spectrum allows us to infer the amount of dust attenuation along the line of sight of this spectrum. The Balmer decrement is fundamentally determined both by quantum mechanics and the physical conditions of the gas (namely its electron temperature and electron density). Any measured deviation from its intrinsic value can therefore be attributed to dust attenuation for a given electron temperature and electron density, assuming Case B recombination (Osterbrock & Ferland, 2005). See Groves et al. (2012) for a comprehensive discussion on the Balmer decrement pertaining to SDSS galaxies.

3.3.1.1 BPT Diagrams

The Balmer decrement is only a valid dust attenuation proxy if the measured $H\alpha$ and $H\beta$ emission lines are actually produced by the recombination of gas ionised by these stars. This is because the adopted intrinsic value of the ratio of $H\alpha$ to $H\beta$ is dependent on the emission being produced by photoionisation. We must, therefore, analyse only regions of the galaxies that are dominated by star-forming processes, and exclude regions for which active galactic nuclei (AGN) – and other excitation mechanisms – are responsible for the majority of the line emission. To this end, we employ the most commonly used Baldwin, Phillips and Terlevich (BPT; Baldwin et al., 1981; see also Veilleux & Osterbrock, 1987) diagram. This diagnostic compares the line ratio $[\text{O III}] \lambda 5007 / H\beta$ to $[\text{N II}] \lambda 6583 / H\alpha$.

This procedure follows the work of Belfiore et al. (2015, 2016), who also provide an overview of BPT diagrams in their work. The emission line ratios described above are particularly useful for this work because they have similar wavelengths, and so will not be affected much by the dust that we are endeavouring to measure. The exact demarcation between star-forming and non-star-forming regions is not uniquely defined (see Kewley et al., 2001 and Kauffmann et al., 2003); in this work, we follow the method outlined by Belfiore et al. (2016) for applying BPT diagrams to MaNGA galaxies and consider line emission in spaxels below the less stringent Kewley et al. (2001) demarcation line to be dominated by star-forming regions. Consequently, spaxels in the “composite” region between these demarcation lines are classified as star-forming in this work. Spaxels above the Kewley et al. (2001) line are assumed to be dominated by excitation mechanisms that are not star-forming in nature – such as AGN, Low Ionisation (Nuclear) Emission line Regions (LI(N)ERs), shocks and Seyfert galaxies – and are thus discarded prior to analysis. For an example of these classifications applied to one of the sample galaxies, see Figure 3.2.

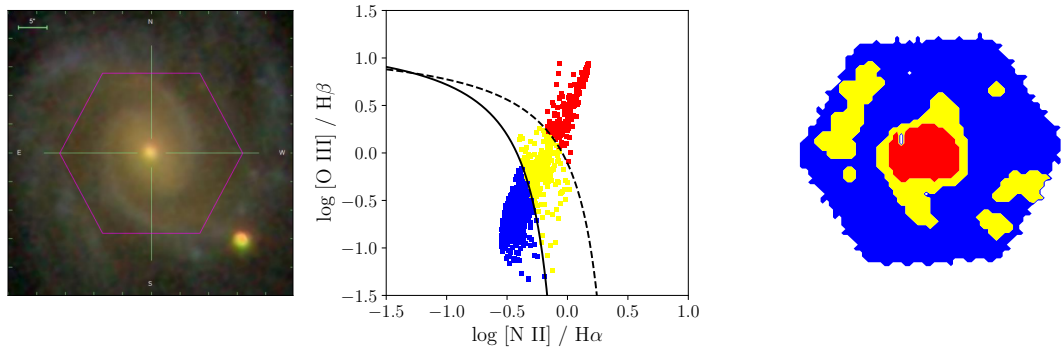


Figure 3.2: 3-colour SDSS image (left), $[\text{O III}] \lambda 5007 / \text{H}\beta$ versus $[\text{N II}] \lambda 6583 / \text{H}\alpha$ BPT diagram (middle), and MaNGA IFU footprint (right) for galaxy 8132-12702. The solid black line in the BPT diagram shows the demarcation line of Kauffmann et al. (2003); the dashed black line, which we use in this work, denotes that of Kewley et al. (2001). Spaxels in both the BPT diagram and the MaNGA footprint are colour-coded depending on their position relative to these lines. Blue spaxels lie below the Kauffmann et al. (2003) demarcation line and are thus considered to be star formation dominated. Red spaxels lie above the Kewley et al. (2001) demarcation line and are considered to be dominated by non-star-forming processes. Yellow spaxels in the composite region between the two demarcation lines are classified as star-forming in this work.

3.3.1.2 Utilising the Balmer Decrement

Ultimately, we want to produce Balmer-decrement derived dust attenuation maps for the sample of galaxies, as well as Balmer-decrement corrected SFR maps, so that we can categorise spaxels by SFR per unit physical surface area. As described in Section 2.1.4, the initial processing of MaNGA data by the DAP has already corrected the emission line fluxes for Milky Way reddening and absorption in the underlying stellar spectrum. Therefore, we need only correct for the dust attenuation intrinsic to the galaxies we are analysing. We first calculate the colour excess $E(B - V)$ using the equation from Osterbrock & Ferland (2005), as in Domínguez et al. (2013); Kreckel et al. (2013):

$$E(B - V) = 1.97 \log_{10} \left[\frac{(\text{H}\alpha / \text{H}\beta)_{\text{obs}}}{2.87} \right]. \quad (3.1)$$

The full derivation for Equation (3.1) can be found in the Appendix of Momcheva et al. (2013). We assume an intrinsic value for $(\text{H}\alpha / \text{H}\beta)_{\text{int}} = 2.87$, which is valid for an electron temperature of $T_e = 10^4 \text{K}$ and an electron density of $n_e = 10^2 \text{cm}^{-3}$, under Case B recombination conditions (Osterbrock & Ferland, 2005).

$(\text{H}\alpha / \text{H}\beta)_{\text{int}}$ is not constant within galaxies; it is dependent upon both the local electron temperature and density. However, as discussed in Section 3.3.1.1,

we only analyse those regions of the galaxies for which star-forming is the dominant source of line emission. In these regions, Osterbrock & Ferland (2005) find that at constant $n_e = 10^2 \text{ cm}^{-3}$, $(\text{H}\alpha/\text{H}\beta)_{\text{int}}$ varies between 3.05 for an electron temperature of $T_e = 5 \times 10^3 \text{ K}$, and 2.76 for $T_e = 2 \times 10^4 \text{ K}$. The dependence on electron density is weaker: at constant $T_e = 10^4 \text{ K}$, $(\text{H}\alpha/\text{H}\beta)_{\text{int}}$ falls only to 2.85 at $n_e = 10^4 \text{ cm}^{-3}$, and to 2.81 at $n_e = 10^6 \text{ cm}^{-3}$ (Osterbrock & Ferland, 2005). Altering the value of $(\text{H}\alpha/\text{H}\beta)_{\text{int}}$ between these extreme values of 3.05 and 2.76 results in an uncertainty in $E(B - V)$ of less than 0.1. Since such a variation is negligible for the analysis in this work, we therefore assume that each spaxel has a uniform value of $(\text{H}\alpha/\text{H}\beta)_{\text{int}} = 2.87$.

The ratio of the dust attenuation at some wavelength λ , A_λ , to the colour excess is denoted $R_\lambda = A_\lambda/E(B - V)$, and is determined at that wavelength for a given reddening curve. In this work, we adopt the reddening curve of Calzetti et al. (2000). When deriving the dust attenuation in the gas from measurements of the Balmer decrement, we choose $R_V = 3.1$; when measuring the dust attenuation affecting the stellar populations, however, we choose $R_V = 4.05$. For a detailed explanation as to why different R_V values are used to determine the two attenuation measures, we refer the reader to Calzetti et al. (2000); see also Catalán-Torrecilla et al. (2015); Pannella et al. (2015). For the gas, we thus obtain $A_{V, \text{gas}} = 3.1E(B - V)$, and for the stellar populations, we instead have $A_{V, \text{stars}} = 4.05E(B - V)$. In this way, the dust attenuation can be calculated purely from measurements of the emission line fluxes of $\text{H}\alpha$ and $\text{H}\beta$ for each star-forming spaxel within all galaxies in the sample.

3.3.2 Stellar Population Modelling

We also determine an entirely independent measure of the dust attenuation affecting the stellar populations at each location on the galaxy. As discussed in Section 2.3.2, we use the full-spectrum stellar population fitting code **STARLIGHT** (Cid Fernandes et al., 2005) to derive a best-fit spectrum for the spectrum of every spaxel in each of the sample galaxies. These best fit spectra are created from a linear combination of a set of input single stellar population (SSP) template spectra – with no assumptions or restrictions on the shape of the derived star formation histories – and an applied dust attenuation, $A_{V, \text{stars}}$.

For the fitted dust attenuation, **STARLIGHT** uses the attenuation curve of Calzetti et al. (2000) with an R_V of 4.05 (see, for instance Calzetti et al., 2000; Catalán-Torrecilla et al., 2015; Pannella et al., 2015). The large wavelength range of the MaNGA and E-MILES spectra are exploited by fitting between 3541.4 and 8950.4 Å to use as much of the information contained in the whole continuum shape as possible to constrain the value of $A_{V, \text{stars}}$. The value of $A_{V, \text{stars}}$ is allowed to vary in the range $-1 \leq A_{V, \text{stars}} \leq 8$ to permit a full exploration of reasonable parameter space. The best fit results are, reassuringly, nearly all contained within

the range $0 \leq A_{V, \text{stars}} \leq 0.8$.

The **STARLIGHT** fit only applies a single $A_{V, \text{stars}}$ to the overall spectrum. Such an approach is a simplification, since we expect the spectra of the youngest stellar populations to be attenuated to a greater degree than those of older populations. To allow for this discrepancy, **STARLIGHT** includes an option to include extra attenuation to be applied to specified SSP templates in the fit. However, in practice, the youngest SSPs do not have strong spectral features, making this extra attenuation degenerate with changes in the continuum shape with population age or metallicity. We therefore do not use this feature. In addition, the contribution of the youngest stellar populations to the total spectrum is difficult to distinguish from hot stars present – but not modelled – in the oldest SSP templates which are responsible for the “UV upturn” (see Yi, 2008 for a review). Peterken et al. (2020) show that this results in **STARLIGHT** fits which are unreliable for stellar populations younger than 30 Myr (an effect also found by Cid Fernandes & González Delgado, 2010), but that the older populations are still modelled well.

Together, these limitations mean that the **STARLIGHT** attenuation measurements are liable to some uncertainties regarding the attenuation of the youngest stars. However, the value of $A_{V, \text{stars}}$ used in the fit is likely to be a good indicator of the average attenuation of the flux from the average stellar population. The stellar population effectively probed by **STARLIGHT**’s attenuation measurement is significantly older than that probed using the Balmer decrement, which specifically measures the attenuation in the star-forming regions.

Nevertheless, this procedure generates reliable values for the dust attenuation affecting the stellar populations for every star-forming spaxel in each of the sample galaxies. In this work, these $A_{V, \text{stars}}$ measurements are determined for every star-forming spaxel in each of the sample galaxies for comparison with the Balmer-decrement derived $A_{V, \text{gas}}$ measurements (described in Section 3.3.1.2). An example comparing $A_{V, \text{stars}}$ to $A_{V, \text{gas}}$ measurements for galaxy 8312-12702 is shown in Figure 3.3.

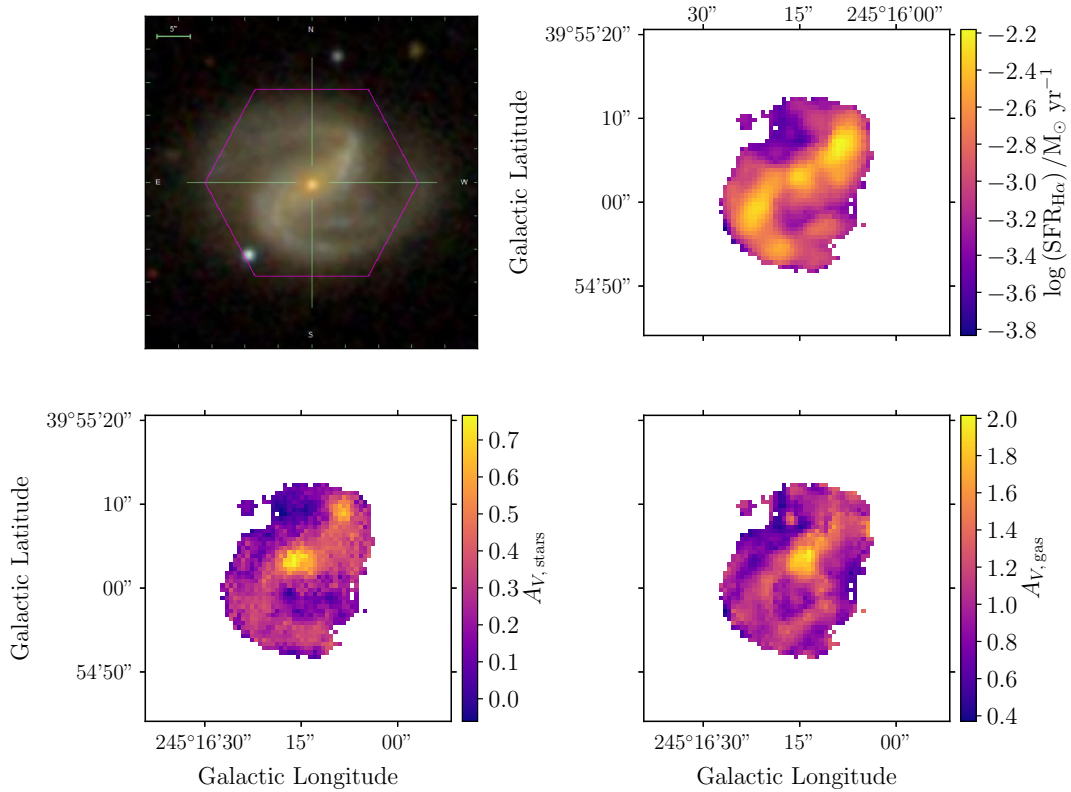


Figure 3.3: 3-colour SDSS image (top left), Balmer-decrement corrected SFR map (top right), dust attenuation map produced by STARLIGHT (bottom left), and dust attenuation map derived from the Balmer decrement (bottom right) for galaxy 8312-12702.

3.4 Categorising Galaxies by Global Properties

We ultimately want to determine which galactic properties are the main drivers of variations in dust attenuation. Therefore, we choose to categorise the sample into four types by looking at two important global properties of galaxies (as shown in Figure 3.4) – first their stellar mass, and second their specific SFR (sSFR; defined as SFR / stellar mass) relative to the star-forming main sequence (SFMS; Grootes et al., 2017). Of course, there are myriad SFMS calibrations from which to choose (for instance Noeske et al., 2007; Peng et al., 2010; Whitaker et al., 2012; Guo et al., 2015; Rodríguez del Pino et al., 2017 – and references within, notably Brinchmann et al., 2004 and Abazajian et al., 2009 – Grootes et al., 2017; Spindler et al., 2018; Salim et al., 2018). We employ the SFMS calculated by Grootes et al. (2017) since these authors fit a SFMS for spiral galaxies with redshifts of $z < 0.06$, which is the appropriate redshift range for the vast majority of the galaxies analysed in

this work. Grootes et al. (2017) derive SFRs by integrating the total near-UV luminosity of the galaxies in their sample.

We first split the galaxies into four distinct categories based on their stellar masses (obtained from the NSA catalogue; Blanton et al., 2005, 2011), as seen in Figure 3.4.

Categorising galaxies by sSFR is more convoluted. We first need to produce SFR maps for each of the galaxies. This in turn requires us to determine the intrinsic H α flux $f_{\text{int, H}\alpha}$ for every star-forming spaxel in each of the galaxies in the sample:

$$f_{\text{int, H}\alpha} = f_{\text{obs, H}\alpha} \times 10^{0.4A_{\text{H}\alpha}}, \quad (3.2)$$

where $f_{\text{obs, H}\alpha}$ is the raw H α flux from the DAP, and the H α dust attenuation, $A_{\text{H}\alpha} = 2.38E(B - V)$ for star-forming galaxies (using the Calzetti et al., 2000 reddening curve with $R_V = 3.1$). The H α luminosity in Watts, $L_{\text{H}\alpha}$ [W], of the galaxies is determined using the luminosity distances provided by the NSA catalogue (Blanton et al., 2005, 2011) for our chosen cosmology. The H α derived SFR, $\text{SFR}_{\text{H}\alpha}$, for each star-forming spaxel in the galaxies may then be calculated using the Kennicutt (1998) relation, assuming a Chabrier (2003) IMF – see also Kreckel et al. (2013); Schaefer et al. (2017, 2019):

$$\text{SFR}_{\text{H}\alpha} [\text{M}_{\odot} \text{ yr}^{-1}] = \frac{L_{\text{H}\alpha} [\text{W}]}{2.16 \times 10^{34} \text{ M}_{\odot} \text{ yr}^{-1}}. \quad (3.3)$$

A $\text{SFR}_{\text{H}\alpha}$ map produced in this way for one of the galaxies in the sample is shown in Figure 3.3.

Dividing a galaxy’s global $\text{SFR}_{\text{H}\alpha}$ by its stellar mass yields the global $\text{sSFR}_{\text{H}\alpha}$, $\Psi_{*, \text{H}\alpha}$ for that galaxy. We use this quantity to categorise the sample galaxies by their vertical offset from the SFMS, $\Delta \log(\Psi_{*, \text{H}\alpha} / \text{yr}^{-1})$ (shown in Figure 3.4; Grootes et al., 2017); that is to say, galaxies are categorised by their $\text{sSFR}_{\text{H}\alpha}$ at a given mass. We choose not to categorise galaxies by $\text{sSFR}_{\text{H}\alpha}$ alone, since doing so would introduce bias due to the implicit dependence on stellar mass.

Figure 3.4 does not actually show the total sSFRs of the galaxies, since Balmer-decrement corrected SFRs can be calculated only for star-forming spaxels, as discussed in Section 3.3.1. Moreover, and of greater concern, the spatial coverage of MaNGA is limited to a distance of $1.5 R_e$ and $2.5 R_e$ for the galaxies in the primary and secondary samples, respectively. This means that we are at risk of calculating lower limits on the global H α derived sSFRs of the sample galaxies. Nevertheless, the majority of star formation should still be captured, since it is likely to be enclosed within $1.5 R_e$.

To estimate how much flux we typically miss in the outer regions of the galaxies, we compared global $\text{SFR}_{\text{H}\alpha}$ calculated from the primary and the secondary sample galaxies separately. The mean global $\text{SFR}_{\text{H}\alpha}$ for the primary sample

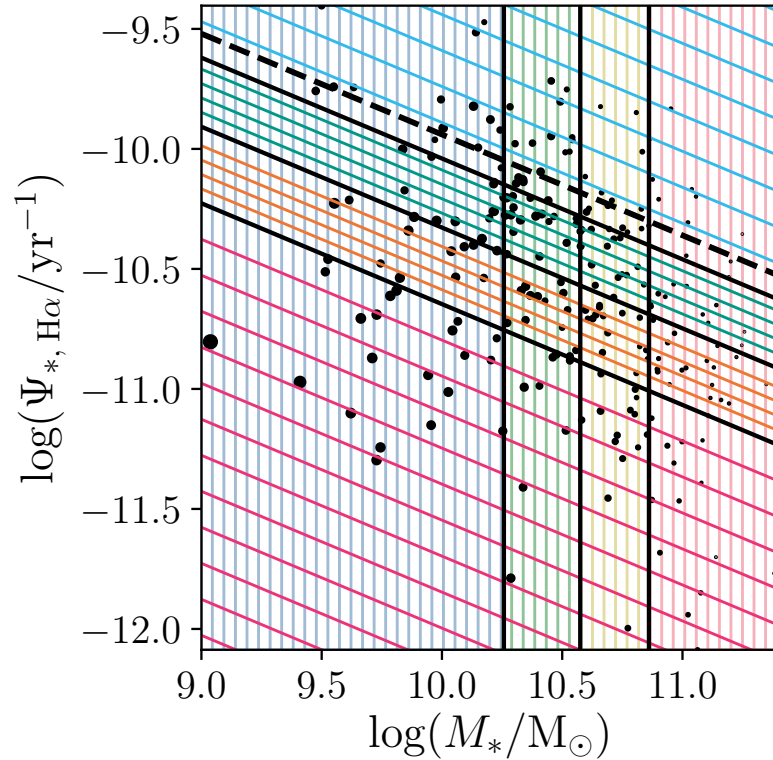


Figure 3.4: Specific SFR relative to the star-forming main sequence (dashed black line; Grootes et al., 2017) versus stellar mass for galaxies in the sample. Galaxies are first categorised based on their mass; we choose there to be roughly the same number of galaxies within each category. Galaxies in the blue region have stellar masses of $\log(M_*/M_\odot) < 10.26$, those in the green have $10.26 < \log(M_*/M_\odot) < 10.58$, those in the yellow have $10.58 < \log(M_*/M_\odot) < 10.86$, and those in the red have $\log(M_*/M_\odot) > 10.86$. We subsequently categorise galaxies by their vertical offset from the SFMS, $\Delta\log(\Psi_{*,\text{H}\alpha}/\text{yr}^{-1})$: galaxies in the magenta region have a sSFR_{H α} of $\Delta\log(\Psi_{*,\text{H}\alpha}/\text{yr}^{-1}) < -0.71$ from the SFMS, those in the orange have $-0.71 < \Delta\log(\Psi_{*,\text{H}\alpha}/\text{yr}^{-1}) < -0.39$ from the SFMS, those in the teal have $-0.39 < \Delta\log(\Psi_{*,\text{H}\alpha}/\text{yr}^{-1}) < -0.10$ from the SFMS, and those in the cyan have $\Delta\log(\Psi_{*,\text{H}\alpha}/\text{yr}^{-1}) > -0.10$ from the SFMS. Solid black lines show the boundaries between these regions. The size of each point is directly proportional to the volume weight for each galaxy. Note that this plot does not show the total sSFRs of the galaxies: simply the sum of SFR_{H α} across all star-forming spaxels within each of the galaxies divided by the total stellar mass.

galaxies is $1.5 \pm 0.1 M_{\odot} \text{ yr}^{-1}$, whereas the increased spatial coverage means that the mean global $\text{SFR}_{\text{H}\alpha}$ for the secondary sample galaxies is slightly higher, at $1.8 \pm 0.3 M_{\odot} \text{ yr}^{-1}$. It therefore seems likely that the limited MaNGA field of view means that the global $\text{H}\alpha$ derived SFRs calculated in this work are systematically underestimated by $\sim 20\%$. This can be seen in Figure 3.4, in which many of the star-forming galaxies lie below the SFMS. It should be noted that this systematic effect does not compromise the final results of this work in any way, because we are interested only in analysing relative differences in star formation activity.

Figure 3.4 therefore plots the sum of the $\text{SFR}_{\text{H}\alpha}$ of each star-forming spaxel for each galaxy divided by the total stellar mass versus the total stellar mass of that galaxy. Bins are chosen such that there are roughly the same number of galaxies within each category. The lowest mass galaxies (blue) have stellar masses of $\log(M_*/M_{\odot}) < 10.26$; the highest mass galaxies (red) have $\log(M_*/M_{\odot}) > 10.86$. Galaxies with the lowest global $\text{H}\alpha$ derived sSFRs relative to the SFMS (magenta) have a $\text{sSFR}_{\text{H}\alpha}$ of $\Delta \log(\Psi_{*,\text{H}\alpha}/\text{yr}^{-1}) < -0.71$ from the SFMS; those with the highest relative $\text{H}\alpha$ derived sSFRs (cyan) have a $\text{sSFR}_{\text{H}\alpha}$ of $\Delta \log(\Psi_{*,\text{H}\alpha}/\text{yr}^{-1}) > -0.10$ from the SFMS. The definitions of these categories as outlined above are used when discussing the results of both Section 3.5 and Section 3.6.

3.5 Global Dust Attenuation Measurements

We first present and discuss the results obtained from looking just at the global properties of the galaxies. In their seminal paper, Calzetti et al. (2000) found empirically that the global ratio of the reddening – i.e. the colour excess $E(B - V)$ – affecting the stellar continuum to that derived from the Balmer decrement was equal to 0.44 ± 0.03 . Since the observed flux from the emission lines and the stellar continuum is not produced by the same stars, the attenuation of the former is more than twice as high as that of the latter (Keel, 1993; Calzetti et al., 1994). The data of Calzetti et al. (2000) were obtained by the International Ultraviolet Explorer (IUE; Boggess et al., 1978). The IUE possessed both a high- and low-resolution spectrograph but was not equipped for integral field spectroscopy (Boggess et al., 1978). In order to compare our work with the results of Calzetti et al. (2000), we initially consider just the global properties of the galaxies in the sample; we do not (yet) make use of the spatial information that MaNGA provides for each galaxy.

Figure 3.5 shows the distributions of the global A_V dust attenuation affecting the stellar populations (hereafter denoted $A_{V,\text{stars}}$), global A_V dust attenuation derived from the Balmer decrement (hereafter $A_{V,\text{gas}}$), and the ratio of the two quantities (hereafter $A_{V,\text{stars}}/A_{V,\text{gas}}$) for each of the four stellar mass categories and the four categories of $\text{sSFR}_{\text{H}\alpha}$ relative to the SFMS. The average $A_{V,\text{stars}}$ and $A_{V,\text{gas}}$ values for each galaxy are light-weighted using the g -band flux. The histogram bins have been volume-weighted. Table 3.1 summarises the volume-

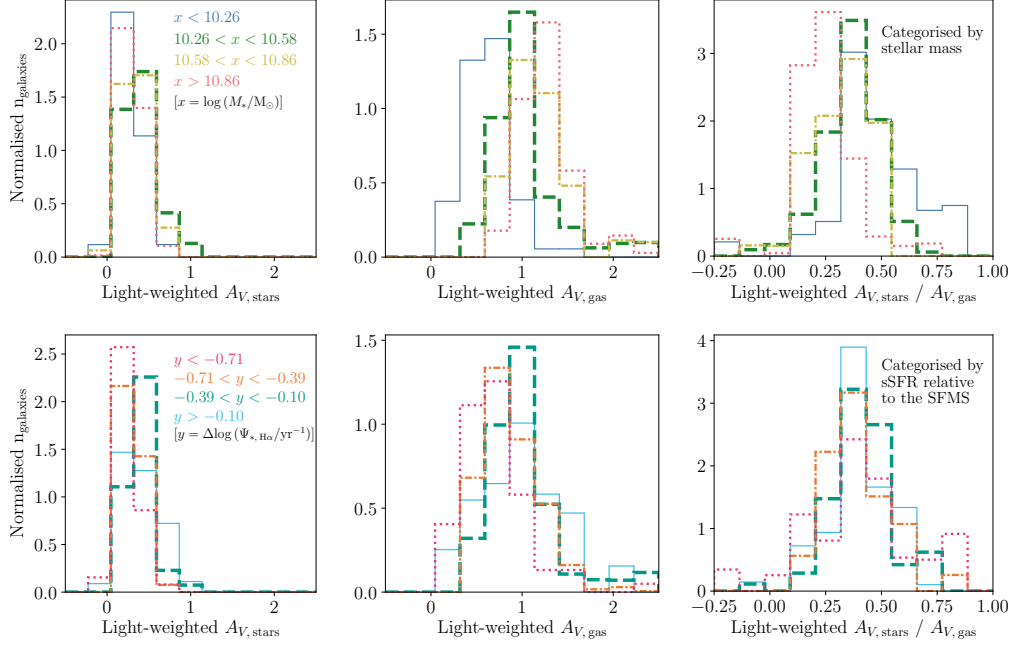


Figure 3.5: Distributions of (from left to right) light-weighted A_V dust attenuation affecting the stellar populations, light-weighted A_V dust attenuation derived from the Balmer decrement, and the ratio of the two quantities. The bins have been volume-weighted, and are normalised so that the area under each line is equal to one. Distributions on the top row have been categorised by stellar mass; blue lines denote the lowest-mass galaxies with stellar masses of $\log(M_*/M_\odot) < 10.26$, green lines denote stellar masses of $10.26 < \log(M_*/M_\odot) < 10.58$, yellow lines of $10.58 < \log(M_*/M_\odot) < 10.86$, and red lines denote the highest-mass galaxies with stellar masses of $\log(M_*/M_\odot) > 10.86$. Distributions on the bottom row have been categorised by global sSFR_{H α} relative to the SFMS; magenta lines denote that galaxies have a sSFR_{H α} of $\Delta \log(\Psi_{*, \text{H}\alpha}/\text{yr}^{-1}) < -0.71$ from the SFMS, orange lines denote a sSFR_{H α} of $-0.71 < \Delta \log(\Psi_{*, \text{H}\alpha}/\text{yr}^{-1}) < -0.39$ from the SFMS, teal lines denote a sSFR_{H α} of $-0.39 < \Delta \log(\Psi_{*, \text{H}\alpha}/\text{yr}^{-1}) < -0.10$ from the SFMS, and cyan lines denote a sSFR_{H α} of $\Delta \log(\Psi_{*, \text{H}\alpha}/\text{yr}^{-1}) > -0.10$ from the SFMS.

Table 3.1: Volume-weighted mean of the light-weighted averages of A_V dust attenuation affecting the stellar populations, A_V dust attenuation derived from the Balmer decrement, and the ratio of the two quantities, for galaxies categorised (1) by stellar mass; (2) by $\text{sSFR}_{\text{H}\alpha}$ relative to the SFMS, $\Delta\log(\Psi_{*,\text{H}\alpha}/\text{yr}^{-1})$. The standard errors on the mean are quoted to 1σ . Also shown are the statistical significance levels between pairs of distributions in Figure 3.5, determined via KS testing. Each sigma value corresponds to how significant the distinction is between a given distribution and the distribution in the table which immediately precedes it.

Stellar mass	Mean $A_{V,\text{stars}}$		Mean $A_{V,\text{gas}}$		Mean $A_{V,\text{stars}}/A_{V,\text{gas}}$	
	Value	Significance	Value	Significance	Value	Significance
$\log(M_*/M_\odot) < 10.26$	0.27 ± 0.02	—	0.62 ± 0.03	—	0.43 ± 0.03	—
$10.26 < \log(M_*/M_\odot) < 10.58$	0.36 ± 0.02	2.0σ	0.99 ± 0.04	$> 5\sigma$	0.36 ± 0.02	2.3σ
$10.58 < \log(M_*/M_\odot) < 10.86$	0.33 ± 0.02	$< 1\sigma$	1.18 ± 0.05	3.4σ	0.29 ± 0.02	1.7σ
$\log(M_*/M_\odot) > 10.86$	0.30 ± 0.02	$< 1\sigma$	1.20 ± 0.03	2.7σ	0.25 ± 0.01	2.9σ
$\text{sSFR}_{\text{H}\alpha}$ relative to the SFMS	Mean $A_{V,\text{stars}}$		Mean $A_{V,\text{gas}}$		Mean $A_{V,\text{stars}}/A_{V,\text{gas}}$	
	Value	Significance	Value	Significance	Value	Significance
$\Delta\log(\Psi_{*,\text{H}\alpha}/\text{yr}^{-1}) < -0.71$	0.25 ± 0.02	—	0.73 ± 0.05	—	0.41 ± 0.03	—
$-0.71 < \Delta\log(\Psi_{*,\text{H}\alpha}/\text{yr}^{-1}) < -0.39$	0.28 ± 0.02	$< 1\sigma$	0.83 ± 0.04	$< 1\sigma$	0.35 ± 0.02	$< 1\sigma$
$-0.39 < \Delta\log(\Psi_{*,\text{H}\alpha}/\text{yr}^{-1}) < -0.10$	0.37 ± 0.02	3.0σ	0.97 ± 0.05	$< 1\sigma$	0.39 ± 0.02	2.1σ
$\Delta\log(\Psi_{*,\text{H}\alpha}/\text{yr}^{-1}) > -0.10$	0.34 ± 0.03	3.7σ	0.92 ± 0.05	2.7σ	0.35 ± 0.03	2.0σ

weighted means of the light-weighted averages for the global $A_{V, \text{stars}}$, $A_{V, \text{gas}}$, and the ratio between the two quantities, for each of the four stellar mass categories and the four categories of $\text{sSFR}_{\text{H}\alpha}$ relative to the SFMS.

Both Figure 3.5 and Table 3.1 show that $A_{V, \text{gas}}$ consistently has a higher mean value than $A_{V, \text{stars}}$. This finding is in agreement with the work of those who have extensively studied dust within starburst galaxies (e.g. Fanelli et al., 1988; Keel, 1993; Calzetti et al., 1994, 2000; Kreckel et al., 2013). Both the peaks of the distributions in Figure 3.5 and the mean global $A_{V, \text{stars}}/A_{V, \text{gas}}$ ratios in Table 3.1 may be compared with the value obtained by Calzetti et al. (2000), who found that $E(B - V)_{\text{stars}}/E(B - V)_{\text{gas}} = 0.44 \pm 0.03$. Accounting for the differing values of R_V used in the reddening curves for the stellar populations and the gas in this work (see Section 3.3.1.2), this ratio of colour excesses corresponds to a ratio of $A_{V, \text{stars}}/A_{V, \text{gas}} = 0.57 \pm 0.04$ (Calzetti et al., 2000). The ratios calculated in this work in Table 3.1 are systematically lower than that found by Calzetti et al. (2000).

The results in this work, however, should not be directly compared with those of Calzetti et al. (2000) for two main reasons. Firstly, the methods are different. Calzetti et al. (2000) derived the dust attenuation affecting the stellar populations by measuring the shape of the observed UV continuum; in this work, however, these attenuation values are obtained through the use of the full-spectrum stellar population synthesis code **STARLIGHT** (Cid Fernandes et al., 2005), which assumes a reddening curve for the stellar continuum. Secondly, the samples are different. The galaxies analysed by Calzetti et al. (2000) were starburst galaxies with exceptionally hyperactive SFRs: the mean and median SFRs of their galaxies are $18 \pm 5 M_{\odot} \text{ yr}^{-1}$ and $5 \pm 6 M_{\odot} \text{ yr}^{-1}$ respectively (Storchi-Bergmann et al., 1994). By contrast, the mean and median $\text{H}\alpha$ derived SFRs of the MaNGA galaxies, at $1.6 \pm 0.1 M_{\odot} \text{ yr}^{-1}$ and $1.0 \pm 0.2 M_{\odot} \text{ yr}^{-1}$ respectively, are more representative of normal star-forming spiral galaxies.

We now consider the effect that both stellar mass and global $\text{sSFR}_{\text{H}\alpha}$ relative to the main sequence of star-forming galaxies have upon both of the dust attenuation measures, and the ratio between them.

Figure 3.5 shows that there is a dependence on the stellar mass of the galaxies for the global light-weighted $A_{V, \text{gas}}$ and the $A_{V, \text{stars}}/A_{V, \text{gas}}$ ratio: the global light-weighted $A_{V, \text{gas}}$ increases and the global light-weighted $A_{V, \text{stars}}/A_{V, \text{gas}}$ ratio decreases as the stellar mass of the galaxies increases. However, this effect is non-existent for the global light-weighted $A_{V, \text{stars}}$, which remains roughly constant in each of the mass categories. Kolmogorov-Smirnov (KS) testing of the distributions in Figure 3.5 reveals that the dependence on stellar mass for the global light-weighted $A_{V, \text{gas}}$ and the $A_{V, \text{stars}}/A_{V, \text{gas}}$ ratio is statistically significant, but finds no statistical difference between the distributions in the global light-weighted $A_{V, \text{stars}}$. The mean values of all of these quantities for each stellar mass category,

as well as the significance levels to which the distributions are distinct, are summarised in Table 3.1.

Further KS testing of the distributions in Figure 3.5 finds that there is only a weak dependence on global $\text{sSFR}_{\text{H}\alpha}$ relative to the SFMS for each of the global light-weighted $A_{V, \text{stars}}$ and $A_{V, \text{gas}}$: as the global $\text{sSFR}_{\text{H}\alpha}$ of the galaxies decreases relative to the SFMS, the values of both the attenuation measures decrease. No statistically significant dependence on global $\text{sSFR}_{\text{H}\alpha}$ relative to the SFMS is detected for the ratio of these two quantities; Table 3.1 shows that the mean values for the global light-weighted $A_{V, \text{stars}}/A_{V, \text{gas}}$ ratio remain roughly constant at ~ 0.35 .

3.6 Spatially Resolved Dust Attenuation

We now use the spatial resolution of MaNGA to look not just at the global properties of the galaxies, but their local properties as well. In particular, we investigate how dust attenuation depends on the location within galaxies: how it varies spatially, with galactocentric radius², and between the spiral arm and inter-arm regions. Moreover, we study how these dust attenuation properties vary between the stellar mass and $\text{sSFR}_{\text{H}\alpha}$ categories defined in Section 3.4.

3.6.1 Spiral Arm and Inter-Arm Regions

Since dust lanes are often associated with the spiral arms of galaxies (e.g. Tamburro et al., 2008; Hou & Han, 2015; Shabani et al., 2018), we use the GZ:3D spiral arm masks to decompose each of the galaxies in the sample into their spiral arm and inter-arm regions. Ultimately, however, almost no significant difference is seen between any of the dust attenuation quantities described so far for data inside the spiral arms and in the inter-arm regions. This null result is likely due to the relatively large FWHM of the MaNGA PSF of $\sim 2.5''$ (Yan et al., 2016a); an angular distance of ~ 2 kpc at the average distance of the sample. At such a spatial resolution, the results are smeared and it is difficult to resolve whether dust lanes, which tend to be narrow (e.g. Xilouris et al., 1999; Dalcanton et al., 2004; Holwerda et al., 2012), are located in the spiral arm or inter-arm region of the GZ:3D mask. This effect is compounded by the fact that GZ:3D respondents would naturally select the brightest part of the image as the spiral arm, which also is likely to

²Galactocentric radius values used in this work are normalised by the elliptical Petrosian effective radius (a measure of the half-light radius), based on the SDSS r -band, from the NASA Sloan Atlas (NSA; Blanton et al., 2005, 2011) catalogue. This method is the most reliable way to measure photometric properties of MaNGA galaxies, and is done in order to account for the effects of inclination on radius measurements. Similarly, stellar mass estimates are taken from the NSA catalogue, again derived from elliptical Petrosian photometry; these masses are produced using `kcorrect` (Blanton & Roweis, 2007), as discussed in Section 2.3.3.

exclude dust lanes which lag behind spiral arms (e.g. Egusa et al., 2004; Chandar et al., 2017) from the GZ:3D masks employed in this work. Finally, dust lanes are optically thick (e.g. White & Keel, 1992; White et al., 2000; Holwerda et al., 2005), which will result in regions of reduced brightness, meaning they might be intentionally omitted from the GZ:3D masks.

Furthermore, observations of nearby galaxies reveal that there is no real physical distinction between spiral and inter-arm regions; instead the two regions are simply a continuum, with a wave in the disk forming the arm (e.g. Mathewson et al., 1972; Rots, 1975; Tamburro et al., 2008; Egusa et al., 2009; Vallée, 2020). However, the peak of this wave occurs in different places for different media. The wave we commonly call the spiral arm is the peak of the wave in the density of young stars, which is why they are dominated by blue light. The gas and dust, however, each peak at different wavelengths; meaning that the region of most dense dust is often located behind the region of highest density of youngest stars, giving the appearance that dust lanes lag behind the spiral arms (e.g. Egusa et al., 2004; Tamburro et al., 2008; Hou & Han, 2015; Chandar et al., 2017; Shabani et al., 2018).

3.6.2 Radial Dependence on Stellar Mass

We next investigate how the average dust attenuation quantities depend on galaxy stellar mass. Figure 3.6 shows graphs of each of local A_V dust attenuation affecting the stellar populations, local A_V dust attenuation derived from the Balmer decrement, and finally the ratio of, and the difference between, these two quantities as a function of radius. The blue points (far left column) are data from the lowest-mass galaxies in the sample. Moving rightwards, the stellar mass increases; the red data (far right column) are from the highest-mass galaxies in the sample. Volume-weighted running medians and inter-quartile ranges are overlaid on the data.

Figure 3.6 compares how the median local dust attenuation affecting the stellar populations, $A_{V, \text{stars}}$, and the median local dust attenuation derived from measurements of the Balmer decrement, $A_{V, \text{gas}}$, the ratio between the two attenuation measures, and the $A_{V, \text{gas}}$ excess are affected by stellar mass. Of these quantities, the median local $A_{V, \text{gas}}$ depends most strongly on stellar mass: its average value increases for increasing stellar mass. This finding is in agreement with those of other authors, who report higher average values for the local $A_{V, \text{gas}}$ for higher-mass galaxies (Nelson et al., 2016a; Jafariyazani et al., 2019). By contrast, the median local $A_{V, \text{stars}}$ does not change appreciably between each stellar mass category (although see González Delgado et al., 2015 and Goddard et al., 2016, both of whom do find higher average values for $A_{V, \text{stars}}$ in galaxies with higher stellar masses. We likely do not see this effect since these authors had at their disposal a much wider range of stellar masses than in this work). At any rate, this work

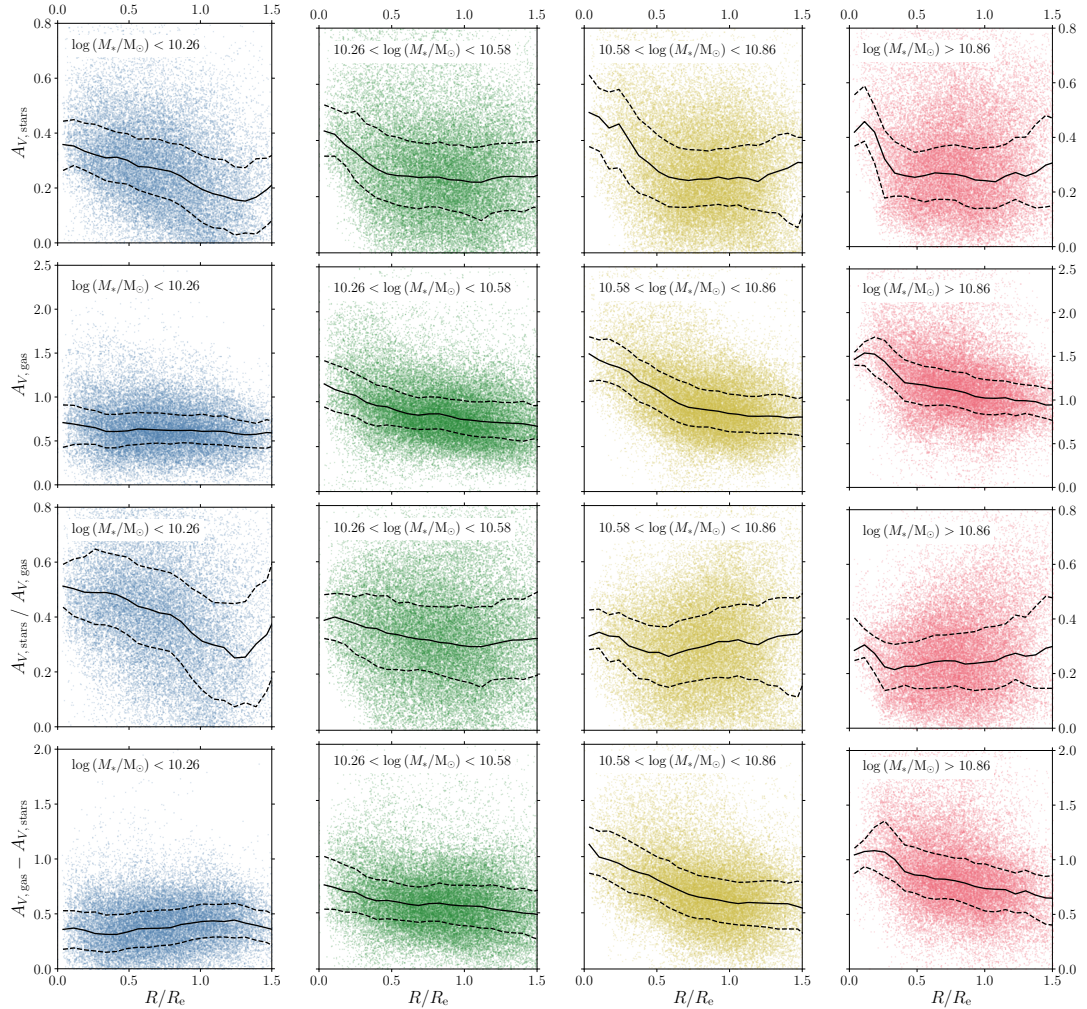


Figure 3.6: All spaxels plotted on scatter graphs showing the local A_V dust attenuation affecting the stellar populations (top row), the local A_V dust attenuation derived from the Balmer decrement (upper-middle row), the ratio of the two quantities (lower-middle row), and the difference between the two quantities (bottom row) as a function of distance from the galactic centre in units of R_e . The blue points (far left column) are data from galaxies with stellar masses in the range $\log(M_*/M_\odot) < 10.26$, green (centre-left column) data are from galaxies with $10.26 < \log(M_*/M_\odot) < 10.58$, yellow (centre-right column) data are from galaxies with $10.58 < \log(M_*/M_\odot) < 10.86$, and the red (far right column) data from galaxies with $\log(M_*/M_\odot) > 10.86$. The running medians (solid black lines) and inter-quartile ranges (dashed black lines) to the data have also been added to each plot. Each of these running averages has been volume-weighted.

shows that the average value of $A_{V, \text{gas}}$ is more strongly influenced by stellar mass than the average $A_{V, \text{stars}}$; this in turn means that the average $A_{V, \text{stars}}/A_{V, \text{gas}}$ ratio decreases for increasing stellar mass.

So far, we have determined the $A_{V, \text{stars}}/A_{V, \text{gas}}$ ratio for the sake of comparison with the work of Calzetti et al. (2000). Although this ratio is a useful diagnostic for determining global properties of galaxies, it is actually not physically motivated, since A_λ is a logarithmic quantity measured in magnitudes (see for instance Salim & Narayanan, 2020). Consequently, the ratio of $A_{V, \text{stars}}$ to $A_{V, \text{gas}}$ – a ratio of two logarithms – does not represent a physically meaningful quantity.

We therefore here introduce a new quantity, which we coin the $A_{V, \text{gas}}$ excess, defined as $A_{V, \text{gas}} - A_{V, \text{stars}}$, and which unlike the $A_{V, \text{stars}}/A_{V, \text{gas}}$ ratio is physically motivated. Since (as we discuss in Section 3.3.2) **STARLIGHT** provides little information about the dust attenuation affecting the youngest stellar populations, $A_{V, \text{stars}}$ primarily quantifies the contribution to the dust attenuation from the diffuse ISM. By contrast, $A_{V, \text{gas}}$ quantifies the dust attenuation due to the combination of this diffuse ISM and the clumpy birth clouds. Therefore, by subtracting $A_{V, \text{stars}}$ from $A_{V, \text{gas}}$ it is possible to estimate the dust attenuation due to the birth clouds alone. Note that the $A_{V, \text{gas}}$ excess probably over-estimates the dust attenuation due to the birth clouds, since **STARLIGHT** calculates the dust attenuation affecting the stellar populations down to $\sim 3 \times 10^7 \text{yr}$, which are relatively young and will hence experience both attenuation from the diffuse ISM and birth clouds.

Since measurements of the $A_{V, \text{gas}}$ excess can also provide information about local variations in the dust geometry of star-forming galaxies, we now examine how the average of this newly-defined quantity varies with stellar mass. Figure 3.6 shows that a similar (though less pronounced) effect is seen in both the variation of the average $A_{V, \text{gas}}$ excess and the average $A_{V, \text{gas}}$, both of which increase as stellar mass increases.

As well as showing the average values of the dust attenuation quantities, Figure 3.6 also shows that both the local $A_{V, \text{stars}}$ and local $A_{V, \text{gas}}$ exhibit some radial dependence: the inner regions possess higher values for both dust attenuation quantities, which flatten out beyond $\sim 0.5 R_e$. Each stellar mass category sees the value of $A_{V, \text{stars}}$ fall from around $\sim 0.4 - 0.5 \text{ mag}$ at the galactic centre to $\sim 0.2 - 0.3 \text{ mag}$ at $1.5 R_e$. Furthermore, the lowest-mass galaxies see no radial variation in their local $A_{V, \text{gas}}$, which remains constant at around $\sim 0.6 \text{ mag}$, whereas for the highest-mass galaxies the local $A_{V, \text{gas}}$ falls almost a magnitude from a value of $\sim 1.6 \text{ mag}$ to $\sim 0.8 \text{ mag}$. It is tempting to explain away this lack of radial variation in the local $A_{V, \text{gas}}$ for the lowest-mass galaxies by assuming that the bulges of low-mass galaxies are proportionally smaller than high-mass galaxies, thereby causing galaxies with lower stellar masses to exhibit lower values of local $A_{V, \text{gas}}$ nearer to their central regions. However, analysis of the bulge-to-total (B/T) light ratio of each galaxy (see Simard et al., 2011) reveals that the mean B/T ratio is broadly

similar for each category: this difference, therefore, is likely not a consequence of low-mass galaxies having small bulges in proportion to their size.

These findings are in agreement with previous work: both González Delgado et al. (2015) as well as Goddard et al. (2016) find that dust attenuation affecting the stellar populations exhibits a similar radial gradient for both CALIFA survey galaxies and MaNGA galaxies, respectively. Furthermore, both Nelson et al. (2016a) and Jafariyazani et al. (2019) show that dust attenuation derived from measurements of the Balmer decrement declines radially in a very similar manner for both 3D-HST survey galaxies and MUSE-Wide survey galaxies, respectively. Moreover, these authors also report steeper radial gradients for higher-mass galaxies for both the local $A_{V, \text{stars}}$ (González Delgado et al., 2015; Goddard et al., 2016) and for the local $A_{V, \text{gas}}$ (Nelson et al., 2016a; Jafariyazani et al., 2019). Again, this behaviour can be seen in the plots of Figure 3.6.

The local $A_{V, \text{stars}}/A_{V, \text{gas}}$ ratio is not particularly affected by radius at any galaxy stellar mass. The highest-mass galaxies (red) exhibit only a very small gradient close to their centres, after which $A_{V, \text{stars}}/A_{V, \text{gas}}$ remains reasonably constant with radius; the ratio for the intermediate-mass galaxies (yellow and green) is roughly constant between the galactic centre and $1.5 R_e$. This behaviour is intriguing considering that $A_{V, \text{stars}}$ and $A_{V, \text{gas}}$ are independent measures of dust attenuation: to yield a ratio that is roughly constant with radius, both the local $A_{V, \text{stars}}$ and $A_{V, \text{gas}}$ must decrease with radius at approximately the same rate. The only exception is the local $A_{V, \text{stars}}/A_{V, \text{gas}}$ for the lowest-mass galaxies (blue), which exhibit a stronger radial gradient for this ratio, driven by the lack of such a gradient in the local $A_{V, \text{gas}}$. Quite why the lowest-mass galaxies exhibit this behaviour is, however, unclear; it is possible that this could be a consequence of higher-mass galaxies having clumpier dust distributions and a greater amount of clumpy dust nearer to their centres than lower-mass galaxies.

The $A_{V, \text{gas}}$ excess varies with radius in a very similar manner to the local $A_{V, \text{gas}}$. The $A_{V, \text{gas}}$ excess is higher at the centres of the galaxies than at their outskirts (again with the exception of those galaxies with the lowest stellar masses). This behaviour suggests that the radial gradients seen in the local $A_{V, \text{gas}}$, both in this work and in other work (e.g. Nelson et al., 2016a; Jafariyazani et al., 2019) cannot be attributed to a radial gradient in the diffuse ISM alone.

3.6.3 Radial Dependence on Relative Global sSFR

When the same analysis is carried out based on the categories of relative global $\text{sSFR}_{\text{H}\alpha}$, similar results are obtained. These results are shown in Figure 3.7, which plots each of the four dust attenuation quantities described in Section 3.6.2 as a function of radius. The magenta data (far left column) are from the galaxies with the lowest relative global $\text{H}\alpha$ derived sSFRs. Moving rightwards, the relative

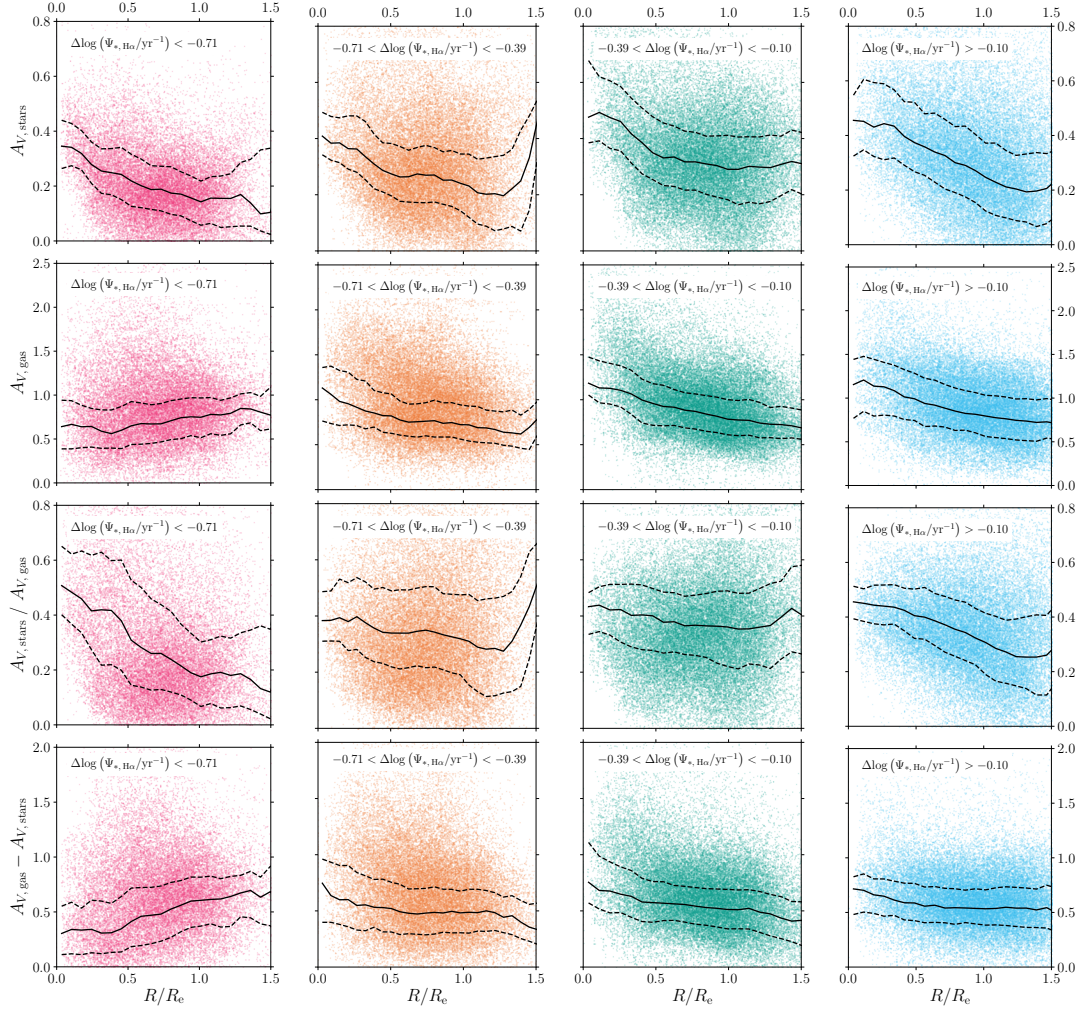


Figure 3.7: As in Figure 3.6, except galaxies are now categorised by their global $\text{sSFR}_{\text{H}\alpha}$ relative to the SFMS. The magenta points (far left column) are data from galaxies with a $\text{sSFR}_{\text{H}\alpha}$ of $\Delta\log(\Psi_{*,\text{H}\alpha}/\text{yr}^{-1}) < -0.71$ from the SFMS, orange (centre-left column) data are from galaxies with a $\text{sSFR}_{\text{H}\alpha}$ of $-0.71 < \Delta\log(\Psi_{*,\text{H}\alpha}/\text{yr}^{-1}) < -0.39$ from the SFMS, teal (centre-right column) data are from galaxies with a $\text{sSFR}_{\text{H}\alpha}$ of $-0.39 < \Delta\log(\Psi_{*,\text{H}\alpha}/\text{yr}^{-1}) < -0.10$ from the SFMS, and the cyan (far right column) data are from galaxies with a $\text{sSFR}_{\text{H}\alpha}$ of $\Delta\log(\Psi_{*,\text{H}\alpha}/\text{yr}^{-1}) > -0.10$ from the SFMS.

global $\text{sSFR}_{\text{H}\alpha}$ increases; the cyan data (far right column) are from the galaxies with the highest relative global $\text{H}\alpha$ derived sSFRs.

The median values of the local $A_{V, \text{stars}}$, $A_{V, \text{gas}}$, and the $A_{V, \text{gas}}$ excess are less dependent on relative global $\text{sSFR}_{\text{H}\alpha}$ than stellar mass. Nevertheless, all of these attenuation quantities have higher values for galaxies with high relative global $\text{H}\alpha$ derived sSFRs compared with those with low relative global $\text{H}\alpha$ derived sSFRs. In contrast to the results of Figure 3.6, the average $A_{V, \text{stars}}/A_{V, \text{gas}}$ ratio is not dependent on relative global $\text{sSFR}_{\text{H}\alpha}$; it has a constant median value of approximately ~ 0.35 , since the average values of the local $A_{V, \text{stars}}$ and $A_{V, \text{gas}}$ are affected in very similar ways by the relative global $\text{sSFR}_{\text{H}\alpha}$ of the galaxy. This contrast suggests that stellar mass has more influence on the local dust attenuation properties of a galaxy than the relative global $\text{sSFR}_{\text{H}\alpha}$.

Strong radial gradients are found for the local $A_{V, \text{stars}}$ for each of the four relative global $\text{sSFR}_{\text{H}\alpha}$ categories, as well as for the local $A_{V, \text{gas}}$ for each of the categories (except the galaxies with the lowest relative global $\text{H}\alpha$ derived sSFRs). The similar radial variation of these two independent measures of dust attenuation causes the local $A_{V, \text{stars}}/A_{V, \text{gas}}$ ratios to remain broadly constant between $0-1.5 R_e$ for each of the categories (except for galaxies with the lowest relative global $\text{H}\alpha$ derived sSFRs). The radial gradients in the $A_{V, \text{gas}}$ excess in Figure 3.7, however, are not as strong as those seen in Figure 3.6. While this behaviour again suggests that both the diffuse ISM and the clumpy birth clouds increase in density nearer to the centres of the galaxies (apart from those with the lowest relative global $\text{H}\alpha$ derived sSFRs), it also reiterates that the galaxy stellar mass is a more important driver of local dust attenuation properties than the relative global $\text{sSFR}_{\text{H}\alpha}$.

3.6.4 Investigating Local Variations in Dust Attenuation

Having studied the effect of global galaxy properties on dust attenuation, we now consider the effect of local properties.

The spatial resolution of MaNGA means that we do not have to group spaxels belonging to the same galaxies into the same categories: we can split the spaxels of each galaxy into multiple groups. In other words, the local effects of dust attenuation are now analysed, rather than purely global effects. Spaxels are categorised based on their $\text{SFR}_{\text{H}\alpha}$ per unit physical surface area (hereafter denoted $\Sigma_{\text{SFR}, \text{H}\alpha}$), as seen in Figure 3.8. The histogram bins have been volume-weighted.

We compare the effect of global $\text{sSFR}_{\text{H}\alpha}$ with local $\Sigma_{\text{SFR}, \text{H}\alpha}$ rather than with local $\text{sSFR}_{\text{H}\alpha}$ since Σ_{SFR} is proportional to SFR per unit physical volume for disks of approximately uniform thickness. SFR per unit physical surface area is hence a more direct physical measurement of the star formation activity in a given region of a galaxy than SFR per unit stellar mass; moreover, local Σ_{SFR} is a less model-dependent measure of star formation activity than local sSFR and yields similar

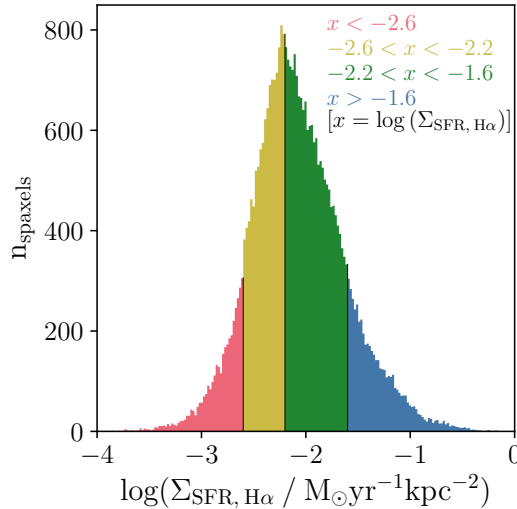


Figure 3.8: Histogram of all spaxels in the sample binned by $\text{SFR}_{\text{H}\alpha}$ per unit physical surface area, $\Sigma_{\text{SFR}, \text{H}\alpha}$. The bins have been volume-weighted. The red region contains spaxels with the lowest $\Sigma_{\text{SFR}, \text{H}\alpha}$, with $\log(\Sigma_{\text{SFR}, \text{H}\alpha} / \text{M}_{\odot} \text{yr}^{-1} \text{kpc}^{-2}) < -2.6$; yellow contains $-2.6 < \log(\Sigma_{\text{SFR}, \text{H}\alpha} / \text{M}_{\odot} \text{yr}^{-1} \text{kpc}^{-2}) < -2.2$; green contains $-2.2 < \log(\Sigma_{\text{SFR}, \text{H}\alpha} / \text{M}_{\odot} \text{yr}^{-1} \text{kpc}^{-2}) < -1.6$; and the blue region contains spaxels with the highest $\Sigma_{\text{SFR}, \text{H}\alpha}$, with $\log(\Sigma_{\text{SFR}, \text{H}\alpha} / \text{M}_{\odot} \text{yr}^{-1} \text{kpc}^{-2}) > -1.6$.

results (González Delgado et al., 2016; Medling et al., 2018; Sánchez, 2020).

Figure 3.9 shows the distributions of the local A_V dust attenuation affecting the stellar populations, local A_V dust attenuation derived from the Balmer decrement, the ratio of the two quantities, and the difference between the two quantities. The histogram bins have been volume-weighted. Table 3.2 summarises the mean values of the volume-weighted local $A_{V, \text{stars}}$, the volume-weighted local $A_{V, \text{gas}}$, and both the ratio and the difference between the two quantities for each of the four newly defined categories.

Figure 3.9 shows that there is a strong dependence on $\Sigma_{\text{SFR}, \text{H}\alpha}$ for each of the local $A_{V, \text{stars}}$, the local $A_{V, \text{gas}}$, the ratio of these two quantities, and the local $A_{V, \text{gas}}$ excess ($A_{V, \text{gas}} - A_{V, \text{stars}}$). KS tests confirm what can be seen by eye – each of the pairs of neighbouring distributions in Figure 3.9 are found to be distinct to well over 5σ confidence. As the $\Sigma_{\text{SFR}, \text{H}\alpha}$ of the spaxels increases, higher values are seen both for the dust attenuation affecting the stellar populations and the dust attenuation derived from measurements of the Balmer decrement. These trends are in agreement with previous work: SFR is shown to be strongly correlated with the total dust content of galaxies (e.g. da Cunha et al., 2008, 2010; Rowlands et al., 2014; Rémy-Ruyer et al., 2015). Furthermore, SFR has been found to increase both as the dust attenuation affecting the stellar populations increases (e.g. Tress et al., 2018), and as the dust attenuation derived from measurements of the Balmer

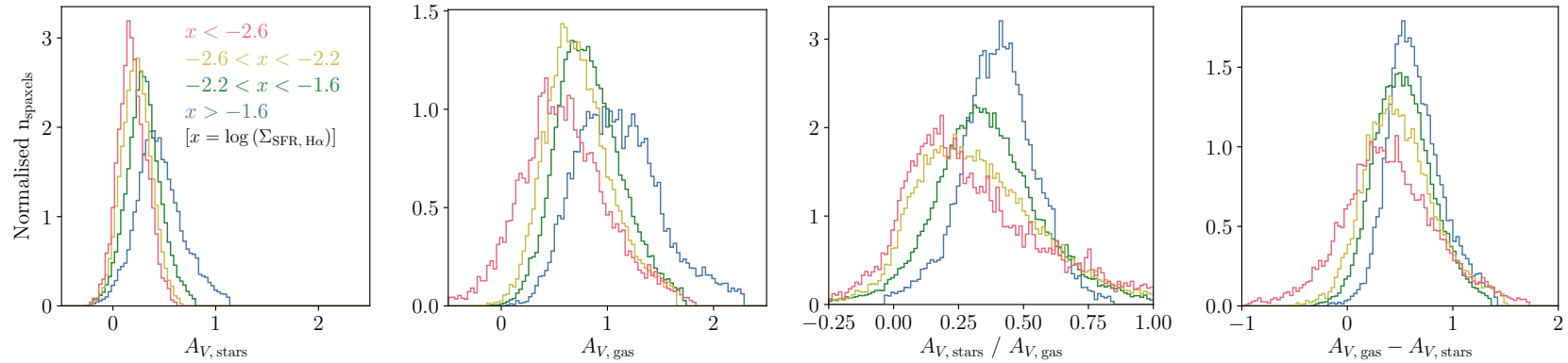


Figure 3.9: Distributions of (from left to right) A_V dust attenuation affecting the stellar populations, A_V dust attenuation derived from the Balmer decrement, the ratio of the two quantities, and the difference between the two quantities. The bins have been volume-weighted, and are normalised so that the area under each line is equal to one. The red histograms comprise spaxels with the lowest $\Sigma_{SFR, H\alpha}$, in the range $\log(\Sigma_{SFR, H\alpha} / M_\odot \text{ yr}^{-1} \text{ kpc}^{-2}) < -2.6$; yellow have $-2.6 < \log(\Sigma_{SFR, H\alpha} / M_\odot \text{ yr}^{-1} \text{ kpc}^{-2}) < -2.2$; green have $-2.2 < \log(\Sigma_{SFR, H\alpha} / M_\odot \text{ yr}^{-1} \text{ kpc}^{-2}) < -1.6$; and blue have the highest $\Sigma_{SFR, H\alpha}$, in the range $\log(\Sigma_{SFR, H\alpha} / M_\odot \text{ yr}^{-1} \text{ kpc}^{-2}) > -1.6$.

Table 3.2: Mean volume-weighted local A_V dust attenuation affecting the stellar populations, A_V dust attenuation derived from the Balmer decrement, the ratio of the two quantities, and the difference of the two quantities for each of the re-defined galaxy categories. The standard errors on the mean are quoted to 1σ .

$\log(\Sigma_{SFR, H\alpha}) [M_\odot \text{ yr}^{-1} \text{ kpc}^{-2}]$	Mean $A_{V, stars}$	Mean $A_{V, gas}$	Mean $A_{V, stars}/A_{V, gas}$	Mean $A_{V, gas} - A_{V, stars}$
$\log(\Sigma_{SFR, H\alpha}) < -2.6$	0.191 ± 0.001	0.592 ± 0.004	0.335 ± 0.005	0.400 ± 0.004
$-2.6 < \log(\Sigma_{SFR, H\alpha}) < -2.2$	0.2312 ± 0.0007	0.733 ± 0.002	0.338 ± 0.001	0.502 ± 0.002
$-2.2 < \log(\Sigma_{SFR, H\alpha}) < -1.6$	0.3000 ± 0.0007	0.833 ± 0.001	0.3635 ± 0.0008	0.534 ± 0.001
$\log(\Sigma_{SFR, H\alpha}) > -1.6$	0.454 ± 0.002	1.108 ± 0.003	0.405 ± 0.001	0.643 ± 0.002

decrement increases (e.g Garn & Best, 2010; Zahid et al., 2013b, 2017). However, the studies undertaken by these authors analysed only the global properties of galaxies; the advantage of this work is to demonstrate that local $\Sigma_{\text{SFR}, \text{H}\alpha}$ variations have more influence than purely global quantities on dust attenuation properties.

The local $A_{V, \text{gas}}$ excess also increases for increasing $\Sigma_{\text{SFR}, \text{H}\alpha}$, which implies that the dependence of the local $A_{V, \text{gas}}$ is not dominated by the dust attenuation due to the diffuse ISM alone. Finally, the $A_{V, \text{stars}}/A_{V, \text{gas}}$ ratio also increases as the $\Sigma_{\text{SFR}, \text{H}\alpha}$ of the spaxels increases, despite the fact that both the numerator and denominator of this ratio increase with increasing $\Sigma_{\text{SFR}, \text{H}\alpha}$. The other plots of Figure 3.9 demonstrate why this is the case: while the dependence on $\Sigma_{\text{SFR}, \text{H}\alpha}$ is strong for $A_{V, \text{gas}}$, this dependence is stronger still for $A_{V, \text{stars}}$. The $A_{V, \text{stars}}/A_{V, \text{gas}}$ ratio therefore increases for increasing $\Sigma_{\text{SFR}, \text{H}\alpha}$. This result is in contrast to that found when considering the purely global properties of the galaxies in Figure 3.5.

The results obtained from Figure 3.9 provide a cautionary tale against putting too much stock in the mean global light- and volume-weighted quantities in Table 3.1 and the mean local volume-weighted quantities in Table 3.2. The mean local $A_{V, \text{stars}}/A_{V, \text{gas}}$ ratios in Table 3.2 especially are at odds with the distributions seen in Figure 3.9, the peaks of which are distinct. For this reason, it is much more illuminating to interpret the results from the distributions of Figure 3.5 and Figure 3.9, rather than simply the mean values in Table 3.1 and Table 3.2.

The behaviour observed in the plots of the $A_{V, \text{stars}}/A_{V, \text{gas}}$ ratio, and, in particular, the $A_{V, \text{gas}}$ excess in Figure 3.9 implies that the increase in concentration of birth clouds nearer to the centres of star-forming spiral galaxies (discussed in Sections 3.6.2 and 3.6.3) is very likely to be a consequence of local physics, rather than global galactic properties. Further, and more generally, the disparity between Figure 3.5 and Figure 3.9 also implies that variations in dust attenuation properties are most likely driven more by local physics than by global physics. Locally, $A_{V, \text{gas}}$ is strongly dependent on $\Sigma_{\text{SFR}, \text{H}\alpha}$ because by isolating only those spaxels within galaxies with higher $\Sigma_{\text{SFR}, \text{H}\alpha}$, a greater number of clumpy birth clouds associated with ongoing star formation should be expected. By contrast, when considering the galaxies globally this effect is washed out because each galaxy is likely to have regions of high $\text{sSFR}_{\text{H}\alpha}$ balanced out by regions where the local $\text{sSFR}_{\text{H}\alpha}$ is lower.

The difference between the global and local distributions for the dust attenuation affecting the stellar populations is not as pronounced. The peaks of the two separate sets of distributions are much closer together than those for the $A_{V, \text{gas}}$ are. The distributions for $A_{V, \text{stars}}$ in Figure 3.5 and Figure 3.9 will average over the clumpy dust since some stars will be in front of the diffuse, dusty ISM (experiencing little attenuation) and some will be behind. This means that there is not as much difference between the global and local $A_{V, \text{stars}}$ distributions. In short, the results of Figure 3.9 imply that while variations in the $A_{V, \text{stars}}$ are probably a result of both local and global physics, variations in the $A_{V, \text{gas}}$, by contrast, are predominantly driven by local physics.

3.7 The Geometry of Dust in Star-Forming Spiral Galaxies

Let us now turn to an interpretation of these results. Models for the geometry of dust in star-forming galaxies – such as that depicted in Figure 13 of Wild et al. (2011) – generally incorporate four key components:

1. **A diffuse, dusty ISM:** This exhibits a radial gradient – the density of the ISM decreases with galactocentric radius.
2. **Young stars:** These highly ionising O and B stars are surrounded by H II regions, and thus produce nebular emission lines. These stars are located in the disk, and are still closely associated with their dusty, clumpy birth clouds.
3. **Intermediate age stars:** These are also found in the disk. Typically, these stars are less associated with birth clouds, and dust attenuation from the ISM dominates.
4. **Old stars:** These are found in both the disks and bulges of spiral galaxies. Relative to an observer outside the galaxy, old stars that are behind the ISM will experience attenuation; those in front of the ISM will not be attenuated by the ISM.

We are now equipped to test the validity of this model. When looking at separate galaxies on a spaxel-by-spaxel basis, as in Figure 3.6 and Figure 3.7, decreasing radial gradients are found for $A_{V, \text{stars}}$. Such gradients can reasonably be attributed to the radial density gradient exhibited by the diffuse, dusty ISM of the host galaxies (e.g. Peletier et al., 1995; Boissier et al., 2004; Muñoz-Mateos et al., 2009; Wild et al., 2011; González Delgado et al., 2015; Goddard et al., 2016).

Ostensibly, a similar explanation might plausibly account for the similar radial gradient exhibited by $A_{V, \text{gas}}$, since a “screen-like” dust attenuation due to the ISM would affect both the old and the young stellar populations in a similar manner. However, this is not in fact the case; such gradients in the dust attenuation derived from the Balmer decrement cannot be explained by a density gradient in the diffuse ISM alone. Both Figure 3.5 and Table 3.1 show that the distributions of both the global light-weighted $A_{V, \text{stars}}$ and $A_{V, \text{gas}}$ increase as the relative global $\text{sSFR}_{\text{H}\alpha}$ of the galaxy increases; this behaviour is a natural consequence of a diffuse ISM which is denser for galaxies with higher sSFRs (e.g. da Cunha et al., 2008, 2010; Rowlands et al., 2014; Rémy-Ruyer et al., 2015). However, the ratio of the two attenuation measures is not dependent upon the relative global $\text{sSFR}_{\text{H}\alpha}$ of the galaxy. This result is in stark contrast to Figure 3.9, in which each of the local $A_{V, \text{stars}}$, the

local $A_{V, \text{gas}}$, and the local $A_{V, \text{stars}}/A_{V, \text{gas}}$ all increase as the local $\Sigma_{\text{SFR}, \text{H}\alpha}$ increases. This behaviour suggests that while the radial gradient in $A_{V, \text{stars}}$ is likely due to a combination of local and global physics (i.e. a diffuse ISM with a radial profile), the seemingly similar gradient in $A_{V, \text{gas}}$ is instead dominated by purely local physics.

The above results suggest that the concentration of birth clouds (and associated young stars) increases towards the centre of star-forming spiral galaxies. Radial gradients have been found in star-forming galaxies for the dust attenuation derived from the Balmer decrement, which we reiterate is a proxy for the dust attenuation due to the birth clouds (e.g. Nelson et al., 2016a; Jafariyazani et al., 2019); SFR per unit physical surface area (e.g. Nelson et al., 2016b; González Delgado et al., 2016; Medling et al., 2018; Sánchez, 2020); and the gas mass per unit physical surface area (e.g. Bigiel et al., 2008; Colombo et al., 2017; Sánchez, 2020; see also Bolatto et al., 2017 and Lin et al., 2017 who find that the molecular gas content of galaxies peaks at their centres). The fact that all of these closely linked quantities are found to decrease with distance from the centres of star-forming galaxies suggests that the same may well be true for the concentration of birth clouds. The increase in molecular gas at the centres of spiral galaxies, seen both by radio (e.g. Bigiel et al., 2008) and IFU (e.g. Lin et al., 2017; Colombo et al., 2017; Sánchez, 2020) observations, is especially indicative of centrally concentrated birth clouds. This is because the molecular gas surface density is related to Σ_{SFR} by the Schmidt–Kennicutt Law (Schmidt, 1959; Kennicutt, 1998). We refer the reader to Bigiel et al. (2008) to see how well Σ_{SFR} is linked to the molecular gas content of galaxies.

A schematic diagram depicting the dust geometry of star-forming spiral galaxies described above is shown in Figure 3.10. This dust geometry is similar to that suggested by Figure 13 of Wild et al. (2011), except that in Figure 3.10 we explicitly depict the radial dependence of the birth clouds, since we find direct evidence for such behaviour. The radial gradients seen for $A_{V, \text{stars}}$ and the $A_{V, \text{gas}}$ excess in Figure 3.6 and Figure 3.7 can be explained by the geometry in Figure 3.10. The line of sight of Observer 1 is far from the galactic centre; therefore, Observer 1 will find low $A_{V, \text{stars}}$ due to the radial dependence of the ISM, and almost zero $A_{V, \text{gas}}$ excess due to the absence of birth clouds along their line of sight. By contrast, Observer 2 has a line of sight close to the galactic centre, and will consequently find higher values for both $A_{V, \text{stars}}$ and the $A_{V, \text{gas}}$ excess.

Further evidence for the concentration of clumpy birth clouds increasing nearer to the centre of star-forming spiral galaxies can be found in Figure 3.6, in which the $A_{V, \text{gas}}$ excess exhibits a radial gradient in all but the lowest-mass galaxies. This behaviour suggests that the radial gradient in the $A_{V, \text{gas}}$ is produced by a combination of radial gradients in both the diffuse dusty ISM and the clumpy birth clouds. The radial gradient in the $A_{V, \text{gas}}$ excess becomes progressively more pronounced for higher-mass galaxies; more massive galaxies, therefore, have clumpier dust distributions and a greater amount of clumpy dust nearer to their centres

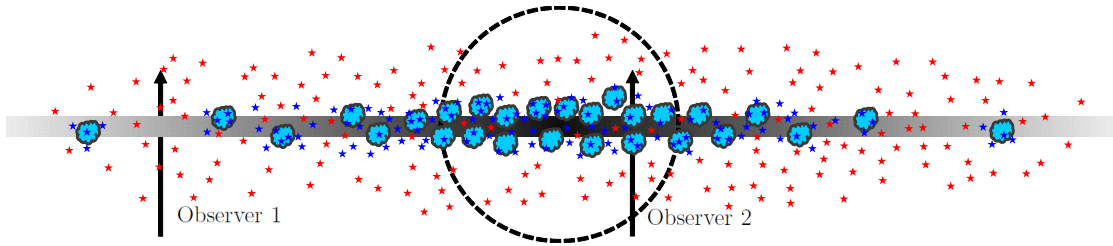


Figure 3.10: Schematic diagram showing an edge-on view of a star-forming spiral galaxy. Depicted are four key components: a *diffuse, dusty ISM* with a radial gradient (grey); *dusty, clumpy birth clouds* surrounded by H II regions (light blue clouds); *young stars* either embedded in, or still closely associated with, these birth clouds (dark blue stars); and *intermediate / old stars* further from their birth clouds (red stars). No assumptions are made about the bulge of the galaxy (dashed black line). Shown also are the lines of sight of two observers. Observer 1 will see a small amount of dust attenuation affecting the stellar populations, but no dust attenuation due to the clumpy birth clouds; Observer 2, however, will see high dust attenuation both due to the diffuse ISM and the clumpy birth clouds. The results in this work suggest that in addition to the presence of a diffuse, dusty ISM, star-forming spiral galaxies also exhibit a higher concentration of young stars and dusty birth clouds nearer to their central regions than at their outskirts.

than less massive galaxies. Figure 3.5 shows that stellar mass is indeed much more important than relative sSFR for determining the global dust and gas properties of a galaxy; this result is in agreement with the findings of others such as Garn & Best (2010) and Zahid et al. (2013b). It is stellar mass that is the dominant factor in determining these global properties, since higher stellar masses cause both higher SFRs (e.g. Brinchmann et al., 2004; Noeske et al., 2007; Peng et al., 2010; Whitaker et al., 2012) and higher gas metallicities (e.g. Tremonti et al., 2004; Mannucci et al., 2010; Garn & Best, 2010; Zahid et al., 2013b). Galaxies with higher stellar masses have higher gas metallicities because they are able to retain a greater proportion of their metals (e.g. Tremonti et al., 2004); this in turn leads to increased dust attenuation, since a greater amount of metals are locked into dust grains (Heckman et al., 1998; Boissier et al., 2004).

In summary, not only do higher-mass galaxies have higher dust attenuations in the diffuse ISM, but they also have even higher dust attenuations due to their birth clouds. The dust geometry in high-mass galaxies must therefore be clumpier than in low-mass galaxies. Furthermore, a greater concentration of birth clouds is found nearer to the centres of high-mass galaxies than at their outskirts. This in turn suggests that star formation may be more centrally concentrated in higher-mass star-forming spiral galaxies.

3.8 Conclusions

We quantify the dust attenuation for 232 star-forming MaNGA spirals using two complementary methods. The Balmer decrement is determined across each galaxy's spaxels, and used to measure the dust attenuation in the gas. This quantity is compared with the dust attenuation affecting the stellar populations of each galaxy, ascertained using the full-spectrum stellar population synthesis code STARLIGHT (Cid Fernandes et al., 2005). Our results can be summarised as follows:

1. The mean global light-weighted dust attenuation affecting the stellar populations ($A_{V, \text{stars}}$) is consistently lower than the mean global light-weighted dust attenuation derived from the Balmer decrement ($A_{V, \text{gas}}$). The mean $A_{V, \text{stars}}$ is not strongly affected by the stellar mass of the galaxy, but the mean $A_{V, \text{gas}}$ increases for increasing stellar mass. Both the mean values of $A_{V, \text{stars}}$ and $A_{V, \text{gas}}$ decrease as the global $\text{H}\alpha$ derived specific star formation rate ($\text{sSFR}_{\text{H}\alpha}$) relative to the star-forming main sequence (SFMS) of the galaxy decreases. The ratio of these two attenuation measures decreases for increasing stellar mass, but is independent of the global $\text{sSFR}_{\text{H}\alpha}$ relative to the SFMS of the galaxy. The calculated ratios are comparable to, but consistently lower than, those found by Calzetti et al. (2000).
2. No difference is found for any of the local dust attenuation quantities analysed in this work between the spiral arm and inter-arm regions of the galaxies. This null result can largely be attributed to the relatively poor spatial resolution of MaNGA, which is unable to resolve narrow dust lanes within the spiral arms. As such, this investigation would be worth revisiting with higher resolution data.
3. Both the local $A_{V, \text{stars}}$ and $A_{V, \text{gas}}$ decrease with galactocentric radius, in agreement with the findings of González Delgado et al. (2015); Goddard et al. (2016) ($A_{V, \text{stars}}$) and Nelson et al. (2016a); Jafariyazani et al. (2019) ($A_{V, \text{gas}}$). By contrast, the local $A_{V, \text{stars}}/A_{V, \text{gas}}$ ratio does not vary between the centre of star-forming spiral galaxies and their outer regions (out to $1.5 R_e$). The exception is the lowest-mass galaxies, which exhibit some radial gradient for this ratio due to the absence of such a gradient in their local $A_{V, \text{gas}}$.
4. We introduce a new dust attenuation quantity, which we coin the $A_{V, \text{gas}}$ excess (defined as $A_{V, \text{gas}} - A_{V, \text{stars}}$). This quantity, unlike the $A_{V, \text{stars}}/A_{V, \text{gas}}$ ratio, is physically meaningful, providing an estimate for the dust attenuation due the birth clouds alone. A radial gradient is also exhibited by the $A_{V, \text{gas}}$ excess, thus demonstrating that the radial gradient in the local $A_{V, \text{gas}}$ cannot be attributed to a gradient in the diffuse ISM alone; the concentration of clumpy dust must also increase nearer to the galactic centre.

5. We utilise the spatial resolution of MaNGA to analyse the local values of each of $A_{V, \text{stars}}$, $A_{V, \text{gas}}$, $A_{V, \text{stars}}/A_{V, \text{gas}}$, and $A_{V, \text{gas}}$ excess. Each of these quantities increases as the local star formation rate per unit physical surface area increases. These results suggest that variations in dust attenuation properties are likely driven predominantly by local physics, rather than the global properties of the galaxies.
6. The results in this work are consistent with the model that stars are born in giant molecular birth clouds in which gas and very clumpy dust are highly concentrated (Lonsdale Persson & Helou, 1987; Charlot & Fall, 2000; Calzetti et al., 2000). However, this work demonstrates that the dust geometry in high-mass galaxies is clumpier than in low-mass galaxies. Furthermore, star-forming spiral galaxies are also shown to exhibit a much higher concentration of both young stars and birth clouds nearer to their central regions than at their outskirts.

The results obtained in this Chapter are, of course, interesting in their own right, but they are also important in the context of the rest of this thesis in our subsequent studies of galactic metallicities. Not only are dust grains themselves metals, but (as discussed at the end of Section 3.7) both the gas and dust contents of galaxies are intimately linked with their stellar masses and their gas metallicities.

We shall explore the relationship between stellar mass and gas metallicity in detail in Chapter 5. For now however, we shall shift our focus in the following Chapter to an investigation of stellar metallicity distributions within spiral galaxies.

Chapter 4

The “G-Dwarf Problem” Revisited

4.1 Introduction

Almost all of the elements heavier than helium that we find in our galaxy’s stars, the “metals”, are there because these objects incorporate matter recycled from previous stellar generations, with stars born early on generally containing less of this enhanced material (Schmidt, 1963; Talbot & Arnett, 1971; Tinsley, 1980). As discussed in Section 1.3.3, there are thus clues to the star-formation history of the Galaxy encoded in the distribution of the metallicity that we find in its stars (Talbot & Arnett, 1971). This phenomenon can be most simply quantified by the cumulative (stellar) metallicity distribution function (CMDf; e.g. Tinsley, 1980), which is just the total mass in stars in which the heavy element fraction is less than Z , $M_*(< Z)$. For a primer on the definition and notation used to describe stellar metallicities, see Section 1.3.1.

Such a simple distribution clearly does not contain the full life history of the Galaxy’s star formation and gas recycling, but it is sufficiently robust to make quite strong statements about its past history. For example, if the Milky Way formed in isolation from a single initial gas cloud of mass $M_{\text{gas},0}$, with enhanced material well mixed in as it is recycled¹ (a scenario termed the “closed box” model of chemical evolution; Schmidt, 1959, 1963; Talbot & Arnett, 1971; Tinsley, 1974), then the CMDf takes the simple form

$$M_*(< Z) = M_{\text{gas},0} [1 - \exp(-Z/p)], \quad (4.1)$$

where p is a parameter that defines the yield of heavy elements created by each generation of stars (see, for example, Binney & Merrifield, 1998 Section 5.3.1). An illustration of the resulting function is shown in Figure 4.1. A conflict between this

¹Throughout this work, we adopt the instantaneous recycling approximation, which assumes that metals are expelled by a generation of stars immediately after these stars form (see, for instance Tinsley, 1980 or Binney & Merrifield, 1998 Section 5.3.1).

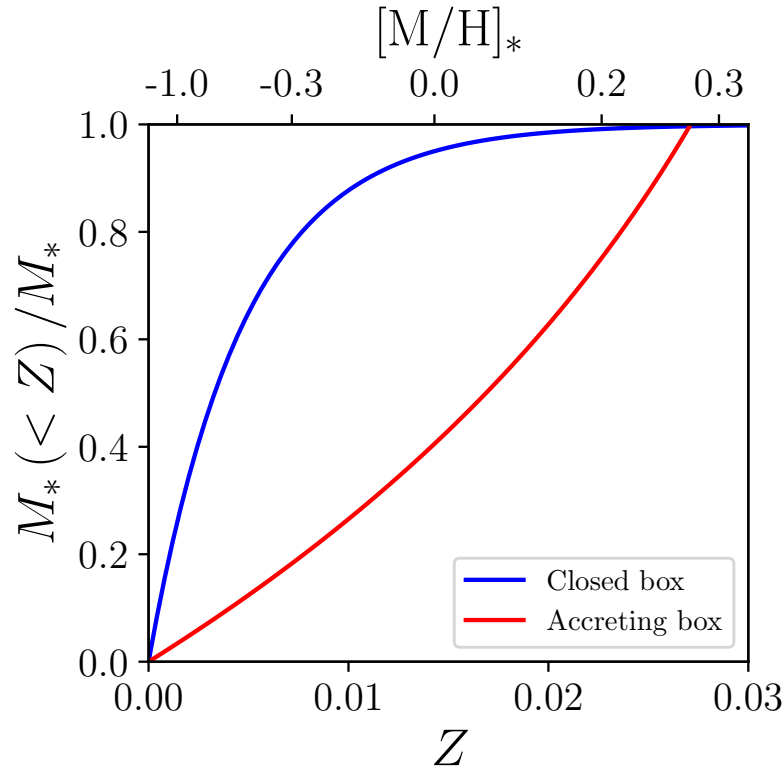


Figure 4.1: Simple model CMDFs showing the fractional mass of stars that have a stellar metallicity less than Z for a closed box (blue) and an accreting box (red). Characteristically, the yield p of a generation of star formation is of order the value of Solar metallicity ($Z_{\odot} = 0.0142$; Asplund et al., 2009); for these models, we adopt yields of one-third Z_{\odot} for the closed box, and three times Z_{\odot} for the accreting box. These yield values are not physically motivated, but have been selected simply for illustrative purposes; as such, the theoretical CMDFs plotted here are not necessarily representative of specific physical systems.

model and observation was first noted by van den Bergh (1962), who pointed out that the Milky Way contains many fewer low-metallicity G-dwarf stars than the steep initial rise in this function predicts (see also Schmidt, 1963). This “G-dwarf problem” has subsequently been observed in populations of K dwarfs (Casuso & Beckman, 2004) and M dwarfs (Mould, 1978; Woolf & West, 2012; Woolf & Wallerstein, 2020), and seen both in the Solar neighbourhood (e.g. Rocha-Pinto & Maciel, 1996; Gratton et al., 1996; Chiappini et al., 1997; Holmberg et al., 2007) and throughout the Galaxy (e.g. Chiappini et al., 2001; Hayden et al., 2015), so is clearly a substantive issue.

Detailed reviews of the G-dwarf problem are given by Pagel & Patchett (1975), Audouze & Tinsley (1976), and Tinsley (1980). In essence, the issue is that by the

time a closed box has built up sufficient heavy elements to make stars with high metallicity, there is very little gas left to make new stars, so it will always produce the majority of its stars at low metallicities. As discussed in Section 1.3.3, a variety of mechanisms have been invoked to seek to resolve the G-dwarf problem (for an extensive list of proposed solutions to the problem, see Pagel, 2009 Section 8.4). However, conceptually the simplest solution – and the most widely accepted – is to introduce a steady stream of pristine gas to the galaxy, the “accreting box” model (Tinsley, 1974, 1975; Tinsley & Larson, 1978), which was originally proposed by Larson (1972, 1976). In this case, the CMDF can be shown to be

$$M_*(< Z) = -M_{\text{gas}} [\ln (1 - Z/p)], \quad (4.2)$$

where M_{gas} is a constant (Binney & Merrifield, 1998 Section 5.3.3). As can be seen from Figure 4.1, the constant addition of new gas provides the raw material necessary for more star formation at later times, tipping the balance in favour of high-metallicity stars. The resulting change in the shape of the CMDF has been found to largely eliminate the G-dwarf problem both in the Solar neighbourhood (Gratton et al., 1996; Chiappini et al., 1997) and across the entire Galaxy (Chiappini et al., 2001; Hayden et al., 2015).

While such a scenario is reassuring for our understanding of the Milky Way, we lack the context to know where our galaxy fits into the wider picture of chemical enrichment. Although stellar metallicity distribution functions can be produced from analysis of resolved stellar populations in Local Group galaxies (e.g. Escala et al., 2018; Manning & Cole, 2018; Gilbert et al., 2019), for more distant unresolved galaxies all that we know for sure is that the average stellar metallicities of less massive galaxies are lower (e.g. Gallazzi et al., 2005; Panter et al., 2008). It therefore remains unclear where the Milky Way lies relative to its spiral galaxy peers in terms of its CMDF.

Fortunately, as recent work by Mejía-Narváez et al. (2020) indicates, the wealth of data obtained by integral field unit (IFU) surveys in the past few years means that we are now in a position to address this question. Observations from the Mapping Nearby Galaxies at Apache Point Observatory (MaNGA) project (Bundy et al., 2015) have provided spectra right across the faces of thousands of nearby galaxies. Spectral synthesis fitting with codes such as **STARLIGHT** (Cid Fernandes et al., 2005) can then be used to decompose such spectra into their component stellar populations of differing ages and metallicities. By integrating across all ages and co-adding all the spatial data for each galaxy, we can reconstruct the CMDFs of these spiral systems for comparison with the Milky Way. Clearly, collapsing all this data into a single one-dimensional function is not making full use of all of the information that it contains, but it does offer a simple robust metric of the global metal content in the stars of a spiral galaxy. While the quality of the reconstructed CMDFs may not be as high as for our own galaxy, it should be more than adequate to distinguish between the very different functions of Figure 4.1,

providing an overview of the stellar metallicity evolution of a complete sample of spiral galaxies in the local Universe.

This relatively succinct Chapter is structured as follows. In Sections 4.2 and 4.3 we recap the sample selection and spectral fitting processes that are relevant to this Chapter. We then present and discuss our results in Section 4.4.

4.2 Sample Selection

In this Chapter, we employ data observed by MaNGA from the MPL-9 data release, as discussed in Section 2.2. MPL-9 comprises a total of 7823 MaNGA galaxies. Since the intent of this Chapter is to place the Milky Way stellar metallicity data in context, we need to select a sample of comparable spiral galaxies from the full MaNGA data set. In order to select only close to face-on spiral galaxies for our analysis, we implement various selection criteria – which we outline in Section 2.2.1 – based upon robust classifications from Galaxy Zoo 2 (Willett et al., 2013; see also Hart et al., 2016). These criteria reduce the MPL-9 sample to the subsample used in this Chapter of 1475 MPL-9 reasonably face-on spiral galaxies.

4.3 Spectral Fitting

The stellar evolution histories of the sample galaxies are determined using the full-spectrum stellar population fitting code **STARLIGHT** (Cid Fernandes et al., 2005). We discuss the methodology of the **STARLIGHT** fitting process fully in Section 2.3.2, but essentially the software derives a best fit to each spectrum by combining a set of single stellar population (SSP) templates of differing ages and stellar metallicities.

We use SSP templates from the E-MILES library (Vazdekis et al., 2010, 2016), which incorporate nine ages ($\log(\text{age}/\text{yr}) = 7.85, 8.15, 8.45, 8.75, 9.05, 9.35, 9.65, 9.95, 10.25$) and six stellar metallicities ($[\text{M}/\text{H}]_* = -1.71, -1.31, -0.71, -0.40, +0.00, +0.22$). Template logarithmic values, $[\text{M}/\text{H}]_*$, are then converted to stellar metallicity $Z = Z_{\odot} \times 10^{[\text{M}/\text{H}]_*}$. To reproduce younger stellar populations, we include an additional six ages ($\log(\text{age}/\text{yr}) = 6.8, 6.9, 7.0, 7.2, 7.4, 7.6$) and two stellar metallicities ($[\text{M}/\text{H}]_* = -0.41, +0.00$) from the templates of Asa'd et al. (2017). As Peterken et al. (2020) recommend, we do not use in our subsequent analysis any stellar metallicities at ages younger than $10^{7.6}$ yr due to uncertainties in the derived SFHs of such populations likely related to the “UV upturn” in old stellar populations (e.g. Yi, 2008; see Section 2.3.3 for a more detailed discussion of this phenomenon). We also do not use stellar metallicities in the age bin at $10^{10.25}$ yr, since this is older than the age of the Universe. As such, it makes no physical sense to retain this age bin for our analysis. Figure 4.2 shows which stellar metallicities were used for the analysis presented in Section 4.4.

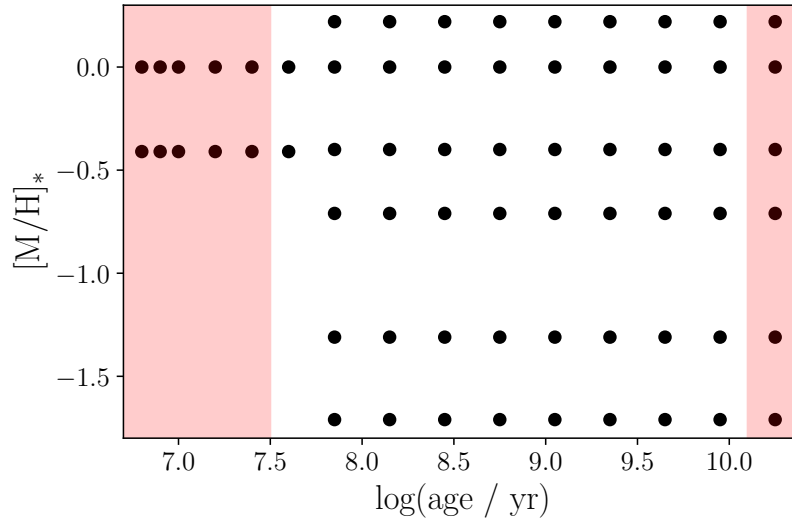


Figure 4.2: As Figure 2.9, with black circles denoting the locations in stellar metallicity–age parameter space of the template SSPs used in the spectral fitting procedure. The red shaded regions indicate that while template SSPs in these regions were used in the fitting procedure, the resulting stellar metallicities determined at these ages from the resulting best-fit spectra are not used in our analysis.

The upshot of the fitting process is that **STARLIGHT** produces a set of weights for the mass contribution made by each template spectrum for every spaxel across the face of a spiral galaxy. Co-adding the results from each spaxel then gives a fit to the integrated light from the entire galaxy, with contributions from SSPs spanning the two-dimensional parameter space of mass-weighted stellar metallicity and age. Adding the contributions from SSPs of different ages reduces the data to a one-dimensional function of the contribution from stars of different metallicities to the total mass of that galaxy. Finally, adding together all the contributions from templates with stellar metallicities less than Z allows us to generate the CMDF, $M_*(< Z)$, for each of the sample galaxies.

4.4 Results and Discussion

The resulting CMDFs are presented in Figure 4.3. In order to investigate any trend with galaxy mass, we have combined the galaxies into five logarithmically-spaced mass bins, normalised each galaxy by its total stellar mass, and calculated the median normalised CMDF within each bin. The step-like nature of the resulting cumulative functions reflects the relatively small number of template stellar metallicities used in the fitting process, which, in turn, is determined by the limited amount of information that can be derived when decomposing such integrated spectral data.

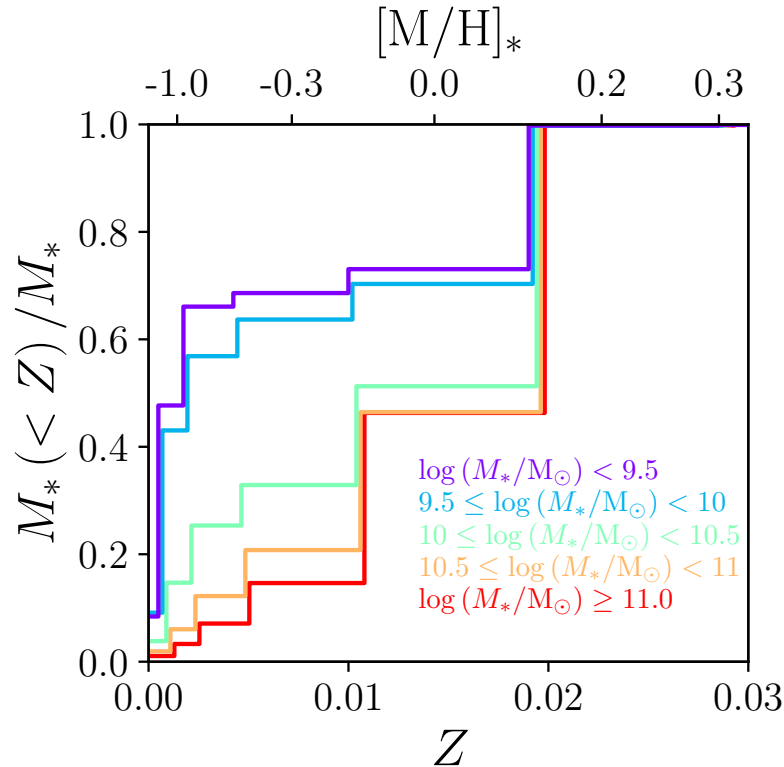


Figure 4.3: CMDFs for the spiral galaxies in the MaNGA sample, binned by stellar mass. The histograms show the median value for the CMDF within each mass bin, normalised by the total mass of each galaxy.

It is immediately apparent from Figure 4.3 that the shape of a galaxy’s CMDF depends strongly on stellar mass. Higher mass galaxies show a steepening CMDF, indicating a relative paucity of low-metallicity stars. Like their kin the Milky Way – a galaxy of stellar mass $\sim 5 \times 10^{10} M_{\odot}$ (McMillan, 2017) – they show a G-dwarf problem, which, comparison to Figure 4.1 confirms, is resolved if these systems are modelled as accreting boxes. By contrast, spiral galaxies with stellar masses of less than $10^{10} M_{\odot}$ show a rapid initial rise in $M_*(< Z)$, reflecting their much greater proportion of low-metallicity stars, and matching rather well to the closed box model shown in Figure 4.1. This finding builds on the significance of the much smaller sample studied by Mejía-Narváez et al. (2020), who found evidence that the distribution of stellar metallicities is broader in lower mass spiral galaxies; and is additionally corroborated by semi-analytic spectral fitting performed by Zhou et al. (2022). It also fits with what has already been gleaned from the other axis in this population decomposition of MaNGA data, the time evolution of star formation, in which it was found that more massive spiral galaxies formed most of their stars in a relatively short period of time, whereas the less massive spiral systems have been slowly but steadily forming their stellar content over most of the

lifetime of the Universe (Peterken et al., 2021a). It would appear that in the more massive galaxies, in order to keep up with the demand for gas to make more stars, largely unmixed pristine gas is pulled in to add to material enriched by the previous generations, making them produce a much larger fraction of high-metallicity stars in what is effectively an accreting box system. By contrast, the more leisurely star formation rate of the lower mass spirals affords them the opportunity to mix recycled gas thoroughly between stellar generations, making them behave as close to closed boxes. While the Milky Way is entirely typical of spiral galaxies of its size in displaying the G-dwarf problem caused by such systems' rush to make stars, lower-mass spiral galaxies avoid the issue by taking their time.

The differences exhibited between the cumulative stellar metallicity distributions of low-mass and high-mass spiral galaxies raise further questions about the overall nature of chemical evolution within these differing systems. In particular, it is interesting to ask whether we would find different behaviour in the time evolution of low-mass spirals compared to higher-mass spirals. Therefore, we shall now follow on from this work, and that of Peterken et al. (2021a), by investigating the time evolution of galactic stellar metallicities in the subsequent Chapter. Furthermore, we shall also endeavour to determine the gas metallicity histories of these same galaxies, in order to ultimately answer the question originally posed at the very start of this thesis: how do the chemical compositions of spiral galaxies change over cosmic time?

Chapter 5

The Chemical Co-Evolution of Gas and Stars in Spiral Galaxies

5.1 Introduction

In order to better understand the fundamental processes that drive galactic formation and evolution, we need to study the chemical evolution of the stars and the gas within these galaxies. However, although metallicities are known to evolve with cosmic time, the precise evolution of the metal content of both the stellar populations and the gas¹ within galaxies is still not fully understood. Since metallicities are closely associated with other fundamental galaxy properties such as star formation rates (SFRs) and stellar masses (e.g. Mannucci et al., 2010; Yates et al., 2012; Curti et al., 2020), this is a crucial problem for astronomy to solve. Consequently, the evolution of metallicities back to the point at which galactic SFRs were at their most prodigious is of particular interest. This epoch, known as “cosmic noon”, occurred at a redshift of $z \sim 1.5$ (Madau et al., 1998; Madau & Dickinson, 2014). It is thus especially important to investigate how metallicities have evolved since cosmic noon to build a robust model of galaxy evolution.

While most studies of chemical evolution tend to focus on gas and stellar metallicities separately, these quantities can – and should – be treated on equal footing, since the stars whose metallicities we measure form from the same gas we are also interested in studying. Previous authors, such as Lian et al. (2018a,b), and Yates et al. (2021), have found success in modelling the metallicities of the gas and the stars within galaxies in tandem.

¹While stellar metallicities can readily be determined via spectral fitting methods, gas metallicities are not directly measured. Instead, we calculate the relative abundance of oxygen to hydrogen of the gas, defined in units of $12 + \log(\text{O}/\text{H})$. Scaling relations are then used to obtain estimates of galactic gas metallicities from these abundances; we describe this process in detail in Section 5.3.2.1.

In recent years, stellar metallicity histories have been determined thanks to observations of low-redshift, spatially resolved galaxies made by integral field unit (IFU) surveys such as the Mapping Nearby Galaxies at Apache Point Observatory (MaNGA; Bundy et al., 2015) survey; the Calar Alto Legacy Integral Field Area (CALIFA; Sánchez et al., 2012) survey; and the Sydney-AAO (Australian Astronomical Observatory) Multi-object Integral field spectrograph (SAMI; Croom et al., 2012) galaxy survey. For example, Peterken et al. (2019a, 2020), Camps-Fariña et al. (2021, 2022), and Fraser-McKelvie et al. (2022) estimate spatially resolved stellar metallicity histories by excavating the fossil records of nearby MaNGA, CALIFA, and SAMI galaxies respectively. Spectral fitting methods, such as those employed by these authors, allow us to track the evolution of the average stellar metallicity with time within individual galaxies. This evolution can be yet further constrained when such methods are used in conjunction with direct observations of average stellar metallicities in higher-redshift galaxies (see, for instance, Onodera et al., 2015; Sanders et al., 2021; and Beverage et al., 2021).

By contrast, determining the gas metallicity histories within galaxies has previously proved elusive. The gas metallicity of a given galaxy can be estimated at the time at which the light was emitted by measuring certain emission lines in the galactic spectra, but it is not possible to track the evolution of these emission lines back over cosmic time. Nevertheless, the desire to do so is well-motivated, as work by Vale Asari et al. (2007) demonstrates. From their analysis of the star formation histories (SFHs) of over 80 000 galaxies, these authors found that galaxies with lower mean gas metallicities evolved more slowly than metal-rich galaxies.

It is, of course, possible to model the gas metallicity histories of galaxies through the use of simulations, as work by authors such as Fu et al. (2012), Somerville et al. (2015) and Yates et al. (2021) demonstrates. Observationally, however, the evolution of the gas metallicity has traditionally been estimated by observing galaxies at increasing redshift (see, for example, work by Troncoso et al., 2014; Wuyts et al., 2014; and Kashino et al., 2017). Unfortunately, this approach provides us only with snapshots of the chemical evolution of galaxies; furthermore, the quality of such snapshots diminishes with the redshift at which they are obtained. In theory, it should be possible to track the complete evolution histories of the gas metallicity in low-redshift, spatially resolved galaxies, just as is done for the average stellar metallicity. However, the wealth of observational information from IFU surveys such as MaNGA has not yet been fully exploited to determine the fossil records of the gas metallicities, as has been so successfully done for the stars which formed from this same gas.

Fortunately, gas metallicities are closely linked to other physical properties of galaxies. In particular, as discussed in Chapter 3, star-forming galaxies with higher stellar masses exhibit higher SFRs (see also, for instance, Brinchmann et al., 2004; Noeske et al., 2007; Whitaker et al., 2012). This correlation is often called the “star formation main sequence”. More massive galaxies also tend to have

higher gas metallicities – a correlation often referred to as the “mass–gas metallicity relation” (MZ_{gR} ; e.g. Tremonti et al., 2004; Mannucci et al., 2010; Zahid et al., 2013b; Maiolino & Mannucci, 2019). Both of these relations are discussed in Section 1.3.2. Moreover, and perhaps unsurprisingly, authors such as Mannucci et al. (2010), Lara-López et al. (2010), Yates et al. (2012), and Curti et al. (2020) have demonstrated that there exists a more fundamental relation between stellar mass, gas metallicity, and SFR (see again Section 1.3.2). In essence, these authors find that gas metallicity exhibits a very tight relationship with both stellar mass and SFR. This relationship is generally referred to as the fundamental metallicity relation (FMR; see, for instance, Figure 2 of Mannucci et al., 2010). Since the FMR does not evolve with redshift out to at least $z \sim 2.5$ (Mannucci et al., 2010; Sanders et al., 2021), it is therefore possible to infer the gas metallicity at earlier cosmic times from quantities that are derivable from spectral fitting – namely, stellar mass and SFR as a function of redshift.

This process of spectral fitting (i.e. decomposing the integrated galaxy spectrum into stellar population spectra of single ages and stellar metallicities) brings us into dangerous territory, and due care must be taken during the procedure (see, for instance, discussions in Cid Fernandes & González Delgado, 2010; Vazdekis et al., 2010, 2016; and Peterken et al., 2020). We have to ensure that the spectra are reliably decomposed into the full two-dimensional stellar metallicity–age plane of the single stellar population (SSP) templates. We must perform checks to ensure that this spectral decomposition can be done safely, after which we can confidently proceed with our analysis of the stellar masses and SFHs produced as a result of the procedure.

In this Chapter, we infer via galactic archaeology the evolution of both the gas and stellar metallicity over cosmic time for a well-defined sample of galaxies in the present-day Universe that have been observed by the MaNGA survey. These quantities are calculated for the same galaxies both at the present day and at a redshift of $z \sim 1.4$. The gas metallicity histories of the galaxies are determined by using the FMR of Mannucci et al. (2010). Giving equal consideration to both the gas and the stars within the galaxies allows us to probe the redshift evolution of their gas and stellar metallicities simultaneously back to the epoch of cosmic noon.

This Chapter is structured as follows. In Section 5.2 we recap the sample selection process relevant to this Chapter. We explain how stellar and gas metallicities are determined – and also describe the various checks and tests we perform on the SSP templates employed in this work – in Section 5.3. Our results are presented and discussed in Section 5.4, and finally Section 5.5 summarises our conclusions.

5.2 Sample Selection

As discussed in Section 2.2, we use data from the full MPL-11 MaNGA data release, which in total comprises 10010 galaxies. These observations were made publicly available with the release of SDSS DR17 (Abdurro’uf et al., 2022). In order to select a representative sample of spiral galaxies, we again implement various selection criteria based upon Galaxy Zoo 2 (Willett et al., 2013; see also Hart et al., 2016) classifications, as described in Section 2.2.1. These cuts leave us with the final subsample of 1619 reasonably face-on spiral galaxies from the MPL-11 data release that we use in this Chapter.

5.3 Metallicities

The chemical compositions of both the stellar populations as well as the gaseous interstellar medium (ISM) within the sample galaxies are considered in this Chapter. In this Section, we detail the processes by which the metallicities of both the stars and the gas are measured. See Section 1.3.1 for a brief primer on metallicities, and an explanation of the notation used throughout this Section.

5.3.1 Stellar Metallicities

The average stellar metallicities of the sample galaxies are calculated using the full-spectrum stellar population fitting code **STARLIGHT** (Cid Fernandes et al., 2005), which we describe in detail in Section 2.3.2. SSP templates from the E-MILES library (Vazdekis et al., 2010, 2016) are used in this work. These incorporate nine ages ($\log(\text{age}/\text{yr}) = 7.85, 8.15, 8.45, 8.75, 9.05, 9.35, 9.65, 9.95, 10.25$) and six metallicities ($[\text{M}/\text{H}]_* = -1.71, -1.31, -0.71, -0.40, +0.00, +0.22$). Younger stellar populations are reproduced by including an additional six ages ($\log(\text{age}/\text{yr}) = 6.8, 6.9, 7.0, 7.2, 7.4, 7.6$) and two metallicities ($[\text{M}/\text{H}]_* = -0.41, +0.00$) from the templates of Asa’id et al. (2017)². See Figure 5.1 for the stellar metallicity–age parameter space occupied by the template spectra.

We do not use stellar metallicities at ages younger than $10^{7.6}$ yr in any subsequent analysis. Although, as we explain in Section 2.3.3, this is due **STARLIGHT** not accounting for the UV upturn in older stellar populations, there is additional motivation for excluding this range of ages in this Chapter. Essentially, at ages younger than $10^{7.6}$ yr, the calculated stellar metallicities also become increasingly unreliable; young, metal-poor stars are rare, and thus it is difficult to create accurate SSP templates for such populations. Moreover, the optical spectra of very

²These SSP ages, which are frequently referred to as lookback times throughout this Chapter, are considered in the rest frame of a given galaxy. For reference, the median redshift of the sample is $z = 0.036$, which corresponds to a lookback time of $\sim 10^{8.7}$ yr.

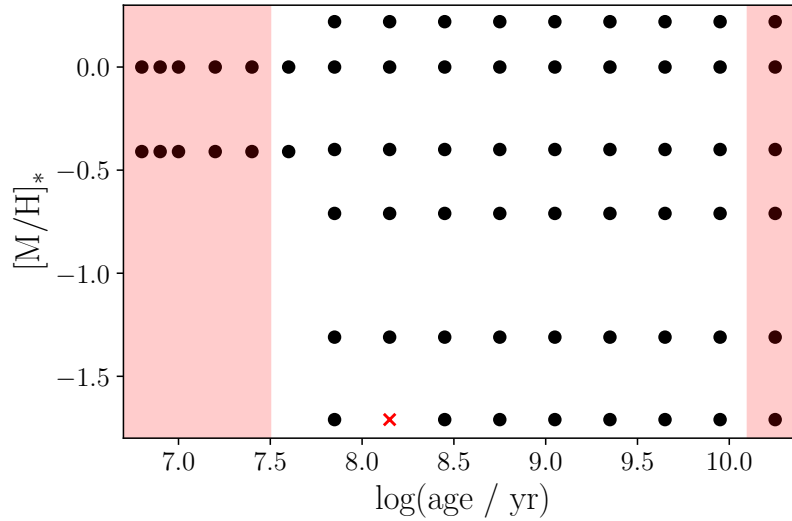


Figure 5.1: As Figure 2.9, with black circles denoting the locations in stellar metallicity–age parameter space of the template SSPs used in the spectral fitting procedure. The red cross indicates that the SSP at $10^{8.15}$ yr and $[M/H]_* = -1.71$ was not included during the fitting procedure – see text for details. The red shaded regions indicate that while template SSPs in these regions were used in the fitting procedure, the resulting stellar metallicities determined at these ages from the resulting best-fit spectra are not used in our analysis.

hot type O stars do not have significant metal absorption lines, and thus provide poor stellar metallicity diagnostics. We do, however, include in our analysis the SSP templates at this threshold age of $10^{7.6}$ yr. Just like in Chapter 4, we do not use stellar metallicities in the age bin at $10^{10.25}$ yr, since doing so would not make physical sense. See Figure 5.1 for further clarification.

The **STARLIGHT** fitting process provides a best fit to the spectrum of every spaxel within each of the sample galaxies. Additionally, **STARLIGHT** produces a set of weights for the mass contribution made by each template spectrum for all of the spaxels whose spectra are fitted. We use these weights to produce two separate one-dimensional functions that we use for subsequent analysis in this Chapter. In Chapter 4, we collapsed these weights along the axis of age; in this Chapter, we now collapse these weights along the axis of stellar metallicity.

Firstly, we can collapse the two-dimensional stellar metallicity–age parameter space by summing the contributions from SSPs of different metallicities. This reduces the data for each galaxy to a one-dimensional function that encodes the proportion of stellar mass that stars in different age bins contribute to the total mass of that galaxy. This allows us to ascertain the stellar mass history of each galaxy at each of the 15 template ages. Furthermore, we also determine the star formation history of the galaxies at each age bin by finding the difference in stellar

mass between two ages, and then dividing this mass difference by the time span between bins.

Alternatively, using a similar procedure, we instead can collapse the same stellar metallicity–age parameter space to form a one-dimensional function of mass-weighted metallicity, which we use to obtain the mean value for the mass-weighted stellar metallicity history for each galaxy at the 15 template ages.

It is well known that some of the SSP templates are ill-constrained by the fitting process (Vazdekis et al., 2010, 2016). In particular, low metallicity templates with ages around $\sim 10^8$ yr are likely to fit systematic errors, such as residual flux calibration errors, rather than the data.

It is particularly difficult to produce reliable SSP templates for low metallicity populations. Creating these templates for populations that are dominated by intermediate age type B and A stars poses a challenge, since these stars are not only rare, but also contain very few metal lines in their spectra. Arguably, it is harder to create templates for these populations than those dominated by type O stars, since type B and A stars are vastly less luminous than their younger counterparts and hence their spectra are harder to observe. Like type O stars, the absence of metal lines makes the optical spectra of intermediate age populations poor metallicity diagnostics. In fact, Vazdekis et al. (2010, 2016) note that the templates of such stars flirt with being unreliable, as can be seen in Figure 6 of Vazdekis et al. (2010) and Figs. 3 and 5 of Vazdekis et al. (2016). Both Figure 6 of Vazdekis et al. (2010) and Figure 3 of Vazdekis et al. (2016) show that the threshold age at which the quality of the SSP templates at $[M/H]_* = -1.71$ drops into the “unsafe” range is almost exactly $10^{8.15}$ yr. Indeed, if we perform a fit to the spectra with all of the templates at our disposal (Figure 5.2), we find that the lowest stellar metallicity template at a lookback time of $10^{8.15}$ yr is hugely over-represented, leading to a systematic distortion in the stellar metallicity history of many galaxies. Such a drop is unphysical, and arises due to **STARLIGHT** latching on to the lowest stellar metallicity SSP template at this age, as this template is erroneously identified as the best fit for the galaxy. For an in-depth discussion about the reliability of the SSP templates used in this work, we refer the reader to Section 3.2 of Vazdekis et al. (2010), as well as Section 2 of Vazdekis et al. (2016).

The simplest course of action to try and address this issue is to exclude this lone problematic template at $10^{8.15}$ yr prior to analysis³. Throwing out this template does largely make the problem vanish, as can be seen in Figure 5.3. While there

³It is reasonable to ask here why we did not also exclude this template in Chapter 4. In the present Chapter, we investigate the variation of stellar mass and stellar metallicity with cosmic time; it is thus crucial to ensure that the mass-weighted stellar metallicity calculated for a galaxy at each template age is reliable. By contrast, in Chapter 4, we collapse the **STARLIGHT** mass weights along the axis of age, obtaining for each galaxy a cumulative distribution function for the fractional mass in stars with stellar metallicity less than Z ; therefore, dubious stellar metallicity values at certain template ages are unimportant to the results of this previous Chapter.

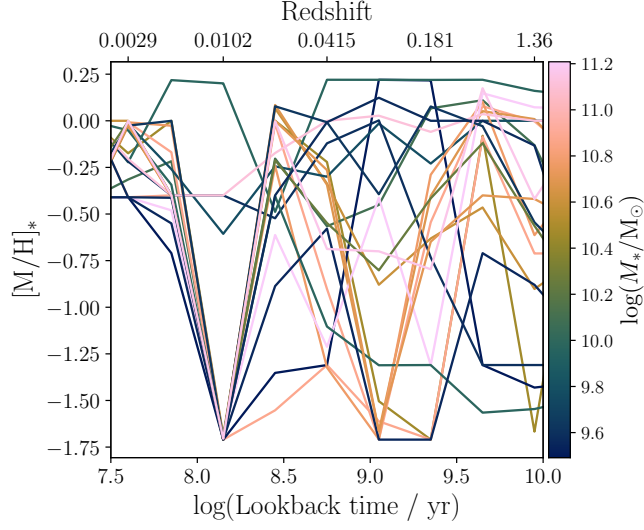


Figure 5.2: Mass-weighted mean stellar metallicity $[M/H]_*$ in each age bin, determined by STARLIGHT, plotted as a function of lookback time for a random subsample of 20 galaxies. The line colour corresponds to the stellar mass of each galaxy. A flaw in the fitting process can be observed at a lookback time of $10^{8.15}$ yr – namely that STARLIGHT is drawn to the lower bound of the stellar metallicity parameter space for this age bin. It is for this reason that we choose to exclude the SSP template with the lowest stellar metallicity value (i.e. $[M/H]_* = -1.71$) at this specific age bin during the fitting process used to determine stellar metallicity histories in this work.

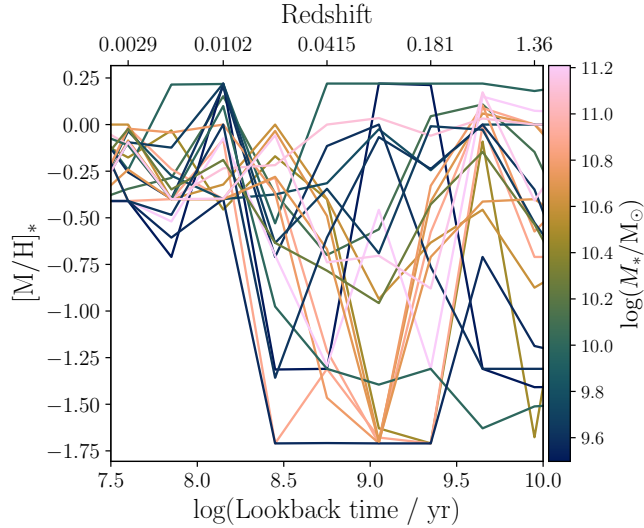


Figure 5.3: As Figure 5.2 for the same random subsample of 20 galaxies, except now the problematic SSP template at $10^{8.15}$ yr and $[M/H]_* = -1.71$ is ignored during the STARLIGHT fitting process.

may still be some residual issues at neighbouring ages, the stellar metallicities for both young (age $< 10^{8.15}$ yr) and old (age $> 10^{9.35}$ yr) populations do not appear to be at all affected by the removal of the SSP template at $10^{8.15}$ yr. Fortunately, since the young and old populations are not strongly coupled, they are robust against this potential systematic uncertainty – particularly when compared to the templates of intermediate age stars. Finally, it is encouraging to see that the mass-weighted mean stellar metallicities in both Figure 5.2 and Figure 5.3 converge to comparable, slightly sub-solar values at more recent lookback times. Despite our earlier concerns about whether the spectra of stars at such ages constitute reliable metallicity diagnostics, this convergence means that we can now with confidence analyse mass-weighted mean stellar metallicities for populations dominated by stars in the range $10^{7.6}$ yr \leq age $< 10^{8.15}$ yr.

Although some systematic residual effects are still apparent in Figure 5.3, the worst of them have been mitigated. Comparing Figs. 5.2 and 5.3, we see that ages $< 10^{8.15}$ yr and $> 10^{9.35}$ yr are largely unaffected by these issues at intermediate ages. Accordingly, we can, with some confidence, compare the inferred mass-weighted mean stellar metallicity properties of galaxies at an age of $10^{9.95}$ yr to those at the present day (age = $10^{7.6}$ yr). This allows us to robustly study chemical evolution since cosmic noon.

5.3.2 Gas Metallicities

The gas metallicities of the galaxies are determined in two separate ways in this work. The first – and most obvious – method by which gas metallicities are calculated is by measuring the strengths of various emission lines in the galaxies’ spectra. While this method is reasonably reliable⁴, measuring the emission lines in these galaxies will naturally only allow the gas metallicities at the present day to be determined. In order to determine the gas metallicities of the galaxies at earlier times, we also employ the FMR of Mannucci et al. (2010). These two separate methods are expanded upon below.

5.3.2.1 Emission Lines

Although it is possible to directly measure the gas metallicity of a galaxy by measuring the strength of its [O III] $\lambda 4363$ emission line, this line is very weak even in the best quality data and with the most appropriate chemical composition (e.g. Kewley & Ellison, 2008; Kewley et al., 2019). Furthermore, this so-called

⁴Calibration methods which rely on converting certain strong emission lines into gas metallicities often notoriously give systematically different values for the gas metallicity, depending on which calibration is used (e.g. Kewley & Ellison, 2008; Maiolino et al., 2008). As Maiolino & Mannucci (2019) acknowledge, these so-called strong-line gas metallicity calibrations provide an “easier, albeit less precise” method by which gas metallicities may be determined.

“direct method” may underestimate gas metallicities in both metal-rich galaxies (e.g. Stasińska, 2002, 2005; Bresolin et al., 2006) as well as metal-poor galaxies (e.g. Kobulnicky & Zaritsky, 1999).

For these reasons, we instead choose to estimate gas metallicities in this work via the use of strong-line methods. Many different theoretical calibrations have been developed to convert certain emission-line ratios, known to be sensitive to gas metallicities, into metallicity estimates. However, in order to obtain gas metallicities from the multitude of strong line calibrations available, these various diagnostics have to first be converted to a common calibration scale. Fortunately, Kewley & Ellison (2008) find that it is possible to convert a given gas metallicity diagnostic into any other calibration scheme via:

$$\log y = \sum_n c_n x^n, \quad (5.1)$$

where y is the original gas metallicity diagnostic to be converted in $12 + \log(\text{O}/\text{H})$ units, the c_n are n th-order polynomial coefficients to be optimised, and x is the gas metallicity (specifically, the oxygen abundance) relative to solar metallicity (which we assume to be $12 + \log(\text{O}/\text{H})_{\odot} = 8.69$; Asplund et al., 2009). For the purposes of subsequent comparison with average stellar metallicities, we convert gas metallicities derived from emission line measurements from their $12 + \log(\text{O}/\text{H})$ values to gas metallicity $[\text{M}/\text{H}]_g$ via:

$$[\text{M}/\text{H}]_g = \log(Z_g/Z_{\odot}) = 12 + \log(\text{O}/\text{H}) - 8.69, \quad (5.2)$$

where Z_{\odot} is the Solar metallicity value ($Z_{\odot} = 0.0142$; Asplund et al., 2009).

There are many different strong line calibrations from which to choose: see, for instance, Kewley & Ellison (2008) for a comprehensive study comparing various different strong line calibrations, as well as to Scudder et al. (2021) for a similar, more recent study exclusive to MaNGA galaxies. However, according to both Kewley & Ellison (2008) and Kewley et al. (2019), the N2O2 ratio – defined as $[\text{N II}] \lambda 6584 / [\text{O II}] \lambda \lambda 3727, 3729$ – is by far the most reliable optical metallicity diagnostic. Not only is it robust (Paalvast & Brinchmann, 2017), but it also does not depend on the ionisation parameter (e.g. Kewley & Dopita, 2002; Blanc et al., 2015). The N2O2 ratio is highly sensitive to gas metallicity for two reasons: firstly, because nitrogen may be formed by both primary and secondary nucleosynthesis processes (e.g. Considère et al., 2000; Kewley et al., 2019); secondly, because the $[\text{O II}] \lambda \lambda 3727, 3729$ line is very sensitive to electron temperature (e.g. Hägele et al., 2008; Kewley et al., 2019). The N2O2 ratio depends on ISM pressure only at very high gas metallicities [$12 + \log(\text{O}/\text{H}) > 9.23$] and at the highest ISM pressures (Kewley et al., 2019). Finally, the N2O2 ratio is also the least sensitive optical diagnostic to the presence of an active galactic nucleus (Kewley et al., 2006) or diffuse ionised gas (Zhang et al., 2017).

While gas metallicities are derived from oxygen abundances (cf. Equation 5.2), stellar metallicities, by contrast, trace the iron abundance of stars (e.g. Tinsley, 1980; Maiolino & Mannucci, 2019). Therefore, in order to treat the metallicities of the stellar populations and the gas from which these formed on equal footing, we must transform our elemental abundance base. Fortunately, Fraser-McKelvie et al. (2022) have demonstrated that it is possible to convert gas metallicities into an iron base using the scaling relations of Nicholls et al. (2017) as follows:

$$\begin{aligned} [\text{M}/\text{H}]_{\text{g, iron}} &= 0.9941 \times (12 + \log(\text{O}/\text{H})) - 8.9011, \\ &\quad (\text{if } 12 + \log(\text{O}/\text{H}) - 8.69 > -0.5), \\ &= 0.6753 \times (12 + \log(\text{O}/\text{H})) - 8.6875, \\ &\quad (\text{if } 12 + \log(\text{O}/\text{H}) - 8.69 < -0.5), \end{aligned} \tag{5.3}$$

(A. Fraser-McKelvie, *private communication*). Throughout the rest of this thesis, any $[\text{M}/\text{H}]_{\text{g}}$ values quoted will be understood to be scaled to an iron base, unless otherwise stated.

In this work, we use the best-fit coefficients calculated by Kewley & Dopita (2002)⁵ in Equation (5.1) to estimate the present-day gas metallicities of the MaNGA galaxies from measurements of the N2O2 line ratio. Since – as Kewley & Ellison (2008) caution – the absolute gas metallicity determined from any particular strong-line method should not be trusted, the final step is to calibrate the gas metallicities calculated in this work to the stellar mass–gas metallicity relation ($\text{MZ}_{\text{g}}\text{R}$) of Tremonti et al. (2004). This is done by forcing the best fit line to our data to have the same value for the gas metallicity predicted by the $\text{MZ}_{\text{g}}\text{R}$ of Tremonti et al. (2004) at a stellar mass of $10^{10} M_{\odot}$. Doing so decreases the calculated gas metallicities by 0.3 dex. Note that the $\text{MZ}_{\text{g}}\text{R}$ is distinct from the stellar mass–stellar metallicity relation, which we denote MZ_{*}R throughout this Chapter for the sake of clarity.

5.3.2.2 The Fundamental Metallicity Relation

Since the aim of this thesis is to compare the chemical evolution of the stars and the gas within spiral galaxies, we require an alternative method for determining the gas metallicities at epochs earlier than the present day.

The relation between gas metallicity and stellar mass, now more commonly known as the $\text{MZ}_{\text{g}}\text{R}$, was first reported by Lequeux et al. (1979), and has since been extensively studied (e.g. Tremonti et al., 2004; Kewley & Ellison, 2008; Zahid et al., 2014a,b, 2017; Curti et al., 2020). More recently, authors began to tentatively report a correlation between gas metallicity and SFR (e.g. Ellison et al., 2008;

⁵ $c_0 = 1.54020$, $c_1 = 1.26602$, and $c_2 = 0.167977$.

Peeples et al., 2009; López-Sánchez, 2010). These two relations were eventually formalised by Mannucci et al. (2010) into a three parameter relation between stellar mass, SFR, and gas metallicity, known as the fundamental metallicity relation (FMR; Mannucci et al., 2010; see also Lara-López et al., 2010). Subsequent authors have confirmed and tested this relation in numerous ways: via simulations (e.g. Yates et al., 2012); observationally, using IFU data from MaNGA and CALIFA (e.g. Cresci et al., 2019); using different abundance scales (e.g. Salim et al., 2014; Sanders et al., 2018; Curti et al., 2020); and its evolution with redshift has also been investigated (e.g. Mannucci et al., 2010; Salim et al., 2015; Sanders et al., 2018, 2021). The form of the FMR used in this work, and its application to solving the problem of determining the gas metallicities in galaxies via galactic archaeology, is given below.

Mannucci et al. (2010) demonstrate that the gas metallicity of a galaxy may be estimated if both its stellar mass, M_* , and its SFR are known:

$$12 + \log(\text{O}/\text{H}) = 8.90 + 0.37m - 0.14s - 0.19m^2 + 0.12ms - 0.054s^2. \quad (5.4)$$

Here, $m = \log(M_*) - 10$, with M_* measured in units of M_\odot ; and $s = \log(\text{SFR})$, with SFR measured in units of $M_\odot \text{ yr}^{-1}$. The FMR described in Equation (5.4) is shown graphically in Figure 1.9 (Mannucci et al., 2010). According to Mannucci et al. (2010), the FMR does not evolve until a redshift of $z \sim 2.5$, while Sanders et al. (2021) conclude that there is no evolution in the FMR until $z \sim 3.3^6$. The findings of Salim et al. (2015) are more conservative; these authors find that there is no redshift evolution until at least $z \sim 2.3$. Nevertheless, we can still use Equation (5.4) to comfortably estimate the gas metallicities of galaxies as far back as the largest lookback time we consider in this work, $10^{9.95} \text{ yr}$ ($z \sim 1.4$)⁷. Again, we convert all gas metallicities determined by using the FMR into $[\text{M}/\text{H}]_g$ values, before calibrating the present-day values against the MZ_gR calculated by Tremonti et al. (2004), as described in Section 5.3.2.1. This calibration results in a decrease in $[\text{M}/\text{H}]_g$ of 0.31 dex at the present day.

Mannucci et al. (2010) did not, as we do in Section 5.3.2.1, use the N2O2 ratio of Kewley & Dopita (2002) as a proxy for gas metallicity in deriving their FMR. Instead, they opted to use a combination of two different emission line ratios: $[\text{N II}] \lambda 6584/\text{H}\alpha$, and $([\text{O II}] \lambda \lambda 3727, 3729 + [\text{O III}] \lambda \lambda 4958, 5007)/\text{H}\beta$ (known colloquially as the N2 and R23 ratios, respectively; see Nagao et al., 2006 and Maiolino et al., 2008 for descriptions of these ratios). Nevertheless, our choice of

⁶While results of earlier work undertaken by these same authors (Sanders et al., 2018) suggest that there may be some very minor evolution in the FMR at $z \sim 2.3$, these results are contradicted by those of Sanders et al. (2021), which, they stress, are more robust. Regardless, since the maximum redshift probed in this work is $z \sim 1.4$, the results of Sanders et al. (2018) should still not be a concern for this work.

⁷Lookback times are converted to redshifts using our assumed cosmology using the Cosmology Calculator of Wright (2006).

N2O2 as a proxy for gas metallicity should not matter for this analysis: there is exceptional agreement between the MZ_gR (and therefore the FMR) of SDSS galaxies derived from measurements of gas metallicity made by Kewley & Dopita (2002) using N2O2, and the MZ_gR obtained by Mannucci et al. (2010) using the N2 and R23 ratios (see the lower panel of Figure 3 in Curti et al., 2020; see also Sanders et al., 2018). Furthermore, Curti et al. (2020) also show that both of these MZ_gR s are consistent with that derived by Tremonti et al. (2004). Additionally, Salim et al. (2014) plot gas metallicities derived both from N2O2 and those obtained by Mannucci et al. (2010) as a function of sSFR, and find that both methods yield consistent results.

Reassuringly, as we shall see from the analysis in Section 5.4.2, gas metallicities inferred from the FMR at recent epochs agree very well with those obtained directly from the gas itself via measurements of the N2O2 line ratio.

5.4 Results and Discussion

We first plot the mass–metallicity relations for both the stellar populations and the gaseous ISM at low and high redshifts. This also allows us to determine how both the MZ_*R and the MZ_gR of the sample galaxies evolve over cosmic time. We then explore the ramifications of these results further by investigating how stellar mass influences the evolution of the average stellar and gas metallicities of these galaxies.

5.4.1 Evolution of the Mass–Metallicity Relations

Figure 5.4 shows mass–metallicity relations for the sample of 1619 MaNGA galaxies. Plots on the top row show the mass-weighted mean stellar metallicities for each of the sample galaxies, and plots on the bottom row show gas metallicity data. The plots in the left-hand column show the MZ_*R and the MZ_gR at the closest lookback time to the present day, $10^{7.6}$ yr ($z \sim 0$), while those in the right-hand column show how both the mass–metallicity relations were at a lookback time of $10^{9.95}$ yr ($z \sim 1.4$; Wright, 2006). Similarly, Figure 5.5 shows (as a comparison), the low-redshift MZ_gR derived from the FMR of Mannucci et al. (2010) compared with the MZ_gR calculated from the N2O2 emission line calibration of Kewley & Dopita (2002). In the latter plot, the gas metallicity for a given galaxy is estimated at the redshift at which the light is emitted from that galaxy; the median redshift of the sample galaxies is $z \sim 0.036$.

The gas metallicities exhibit a much tighter relationship with stellar mass than do the mass-weighted mean stellar metallicities. This is because they are estimated (via the FMR – see Equation 5.4) using just two input parameters: the stellar mass and the SFR at a particular age. This means that the tight relationship in the

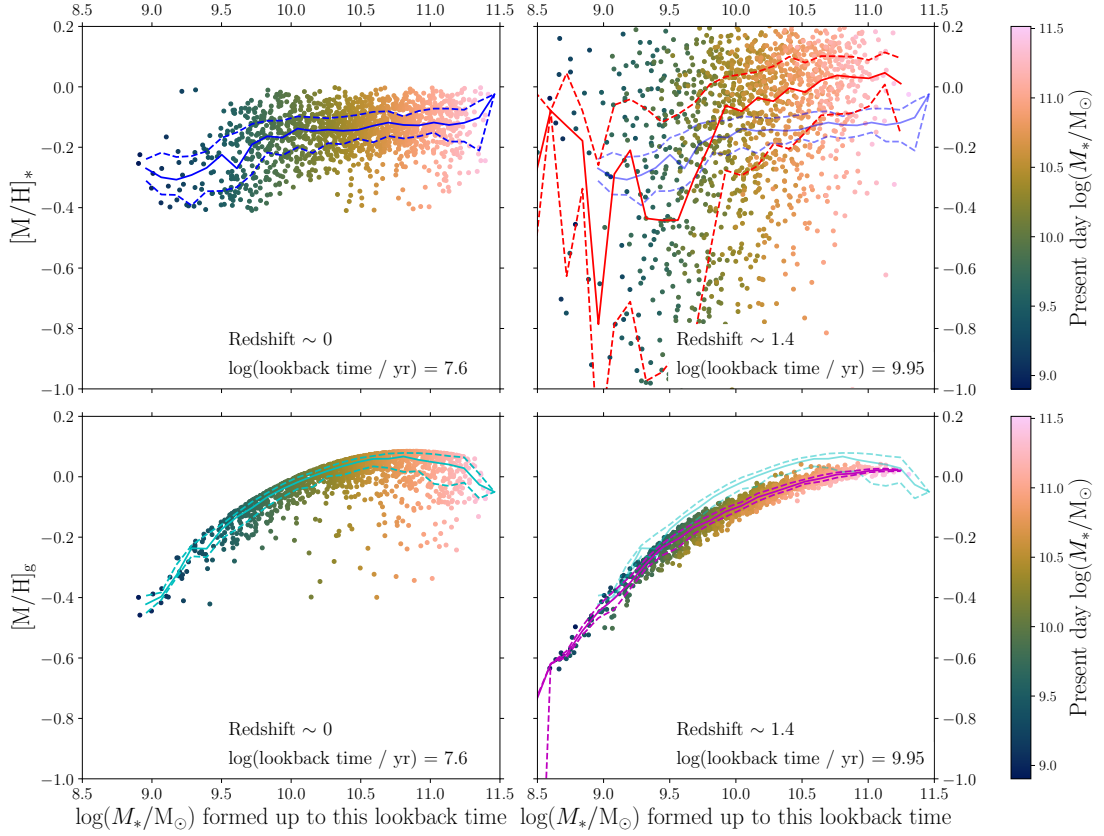


Figure 5.4: Mass–metallicity relations for the sample of MaNGA galaxies. Individual galaxies are coloured by their present-day stellar masses. The horizontal axis shows the mass in stars that has formed up to a certain lookback time. The plots on the top row show mass-weighted mean stellar metallicity as a function of stellar mass, while the plots on the bottom row show gas metallicity as a function of stellar mass. The data in the left-hand column are from the youngest age bin at a lookback time of $10^{7.6}$ yr, while the right-hand column shows data from the oldest age bin at a lookback time of $10^{9.95}$ yr. The running medians (solid lines) and running inter-quartile ranges (dashed lines) to the mass-weighted mean stellar metallicity data at high and low redshift are overplotted in red and blue, respectively. Similarly, the equivalent lines for the gas metallicities at high and low redshift are overplotted in magenta and cyan, respectively.

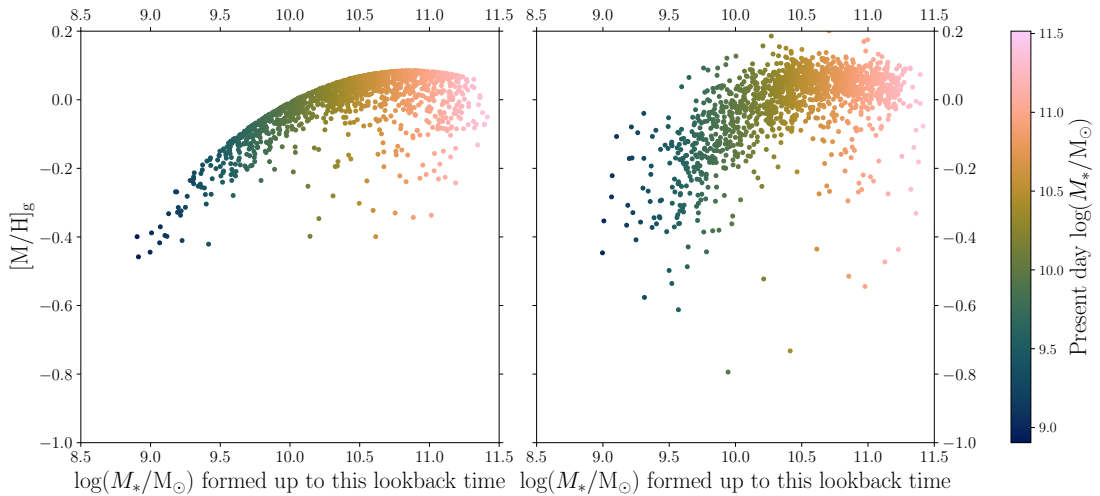


Figure 5.5: Low redshift mass–gas metallicity relations for the sample of MaNGA galaxies. Just as in Figure 5.4, individual galaxies are coloured by their present-day stellar masses, and the horizontal axis shows the mass in stars that has formed up to this lookback time. The left-hand plot shows the MZ_gR at a lookback time of $10^{7.6}$ yr derived from the FMR of Mannucci et al. (2010) – i.e. exactly the same plot as the bottom-left panel of Figure 5.4. The right-hand plot shows, as a comparison, the MZ_gR estimated from the N2O2 emission line calibration of Kewley & Dopita (2002) at the time the light was emitted from the galaxies.

MZ_gR is actually a consequence of the tight relationship between stellar mass and SFR. The MZ_gR is seen to increase to higher gas metallicity values between a redshift of $z \sim 1.4$ and the present day. This result is in line with many authors who have previously studied the redshift evolution of the MZ_gR – for instance Maiolino et al. (2008); Moustakas et al. (2011); Zahid et al. (2013a, 2014b); Lian et al. (2018a,b); and Yates et al. (2021). The gas metallicities determined in this work are, as discussed, derived from measurements of stellar mass and SFR – and encouragingly, the star forming main sequence has also been found to evolve in a similar way over cosmic time (e.g. Madau et al., 1996; Noeske et al., 2007; Whitaker et al., 2012; Speagle et al., 2014).

A similar evolution in the MZ_*R has been found from semi-analytic modelling performed by Yates et al. (2021), as well as at a high redshift range of $1.6 \leq z \leq 3.0$ by Kashino et al. (2022). Observational results at low redshifts from authors such as Camps-Fariña et al. (2021, 2022) and Fontanot et al. (2021) also show that the MZ_*R does indeed evolve from high to low redshift, with high-mass galaxies found to evolve faster than low-mass ones. It is important to note, however, that Camps-Fariña et al. (2021, 2022) also find that the chemical evolution history of a galaxy may be strongly influenced by other fundamental properties, such as their stellar masses and morphologies. In addition, Beverage et al. (2021) find that the MZ_*R may not evolve with redshift at all, depending on the elemental abundance

concerned.

It can be seen from Figure 5.4 that there has been little evolution in the median $MZ_{*}R$ with redshift since a lookback time of $\sim 10^{9.95}$ yr. While a similar lack of evolution in the $MZ_{*}R$ over this time period is reported by Panter et al. (2008) and Vale Asari et al. (2009), other authors, such as Camps-Fariña et al. (2021, 2022) show that $[M/H]_{*}$ has decreased since this lookback time. However, the overall spread of the $MZ_{*}R$ clearly does evolve with redshift. Fundamentally, there is a very large spread in the observed mass-weighted mean stellar metallicities of galaxies, particularly at higher redshifts. This can be seen in this work in the top-right plot of Figure 5.4, as well as in work by previous authors such as Gallazzi et al. (2005); Panter et al. (2008); and Beverage et al. (2021). The spread of the data in this top-right plot is very similar to the $MZ_{*}R$ found by Panter et al. (2008).

As we move closer to the present day, however, the mass-weighted mean stellar metallicities exhibit a much tighter relation with stellar mass, and are comparable to the observed gas metallicities; the data here are actually in much better agreement with the $MZ_{g}R$ of Tremonti et al. (2004). Such a finding is in accord with previous work by authors such as González Delgado et al. (2014), Sánchez et al. (2018), and Lacerda et al. (2019), each of whom find good agreement between the $MZ_{g}R$ and the $MZ_{*}R$ at young stellar ages. This makes sense when we recall that this is the gas from which these same stars are forming. That the mass-weighted mean stellar metallicities converge in this manner over cosmic time is not a consequence of our sample selection; in reality it is a consequence of the rich and varied chemical evolution histories of the individual galaxies over several generations of star formation. As Fraser-McKelvie et al. (2022) explain, the difference between stellar and gas metallicities at early cosmic times is dependent on the SFH of the galaxy. Galaxies that reach their peak SFR at later times take longer to accumulate metals, and so $[M/H]_{*} \ll [M/H]_{g}$ (Fraser-McKelvie et al., 2022).

The analysis presented in this work ultimately represents a step forward over complementary methodology by which gas metallicities are also observationally determined – i.e. obtaining snapshots of the metallicity of the gas in various galaxies at increasing redshifts. While the quality of data obtained via these snapshots decreases with increasing redshift, this alternative method of galactic archaeology, by contrast, acquires high-quality measurements of the gas metallicity back to distant lookback times, as seen in Figure 5.4. Such analysis is similar to that which has already been carried out for the stellar metallicity histories of galaxies by authors such as Peterken et al. (2019a, 2020), Camps-Fariña et al. (2021, 2022), and Fraser-McKelvie et al. (2022). Furthermore, since we are tracking the evolution of the gas (as well as the stellar populations) from observations made in very low-redshift galaxies, we are also able to check the validity of our archaeological approach against present-day emission-line data in these same galaxies. This

concept is explored further in Section 5.4.2.

5.4.2 How does Stellar Mass Affect Metallicity Evolution?

In order to investigate how stellar mass influences metallicity evolution, we now turn to Figure 5.6, which shows how both mass-weighted mean stellar metallicity, $[M/H]_*$, and gas metallicity, $[M/H]_g$, have evolved with cosmic time since cosmic noon. We have divided the galaxies into five logarithmically-spaced stellar mass bins, and calculated the median of the gas and mass-weighted mean stellar metallicity for each mass bin. The star-shaped datapoints are generated using mass-weighted mean stellar metallicity data from STARLIGHT, and gas metallicity data from the FMR of Mannucci et al. (2010); these evolve from a lookback time of $10^{9.95}$ yr through to $10^{7.6}$ yr. The open circles show – as a comparison – the same stellar metallicities at a lookback time of $10^{7.6}$ yr, but plotted instead against the present-day gas metallicities that have been directly determined from measurements of the N2O2 ratio. The two complementary methods for determining gas metallicities at the present epoch yield consistent values for galaxies in all mass bins. To summarise, Figure 5.6 represents the ultimate result of the co-evolution of gas and stellar metallicity that we originally set out to measure. As mentioned in Section 5.3.2.2, the good agreement between the present-day gas metallicity derived from the FMR and that measured directly from emission lines gives some confidence in the validity of this approach.

In interpreting these results, let us first consider those spiral galaxies with stellar masses less than $10^{10} M_{\odot}$. Generically, these galaxies are seen to increase both their stellar and gas metallicities since cosmic noon. The increases in the median gas metallicities are consistent with those measured by Maiolino et al. (2008), and similar increases in stellar metallicities over this time period are also seen by Camps-Fariña et al. (2021). While certain authors, such as Sánchez Almeida (2017), Sánchez-Menguiano et al. (2019), and Belfiore et al. (2019a), have reported that gas accretion may in fact play an important role in galactic evolution, even in low-mass systems, the findings presented in this Chapter fit in well with the results presented in Chapter 4, in which we concluded that such relatively low-mass spiral galaxies tend to evolve as closed boxes (i.e. very little or no gas flows into or out of the galaxy over the course of its life – see Talbot & Arnett, 1971 and Tinsley, 1974).

Within the context of these results, the behaviour of the low-mass spiral galaxies in Figure 5.6 is to be anticipated. Since these low-mass galaxies evolve as closed boxes but are still forming stars at the present epoch, they must be forming stars over much longer timescales than their high-mass counterparts. Previous authors, such as Vale Asari et al. (2007), have attributed the languid star formation within such galaxies to their proportionally lower gas metallicities (see Figure 5.6). However, it is more likely that the low stellar masses of such galaxies are actually

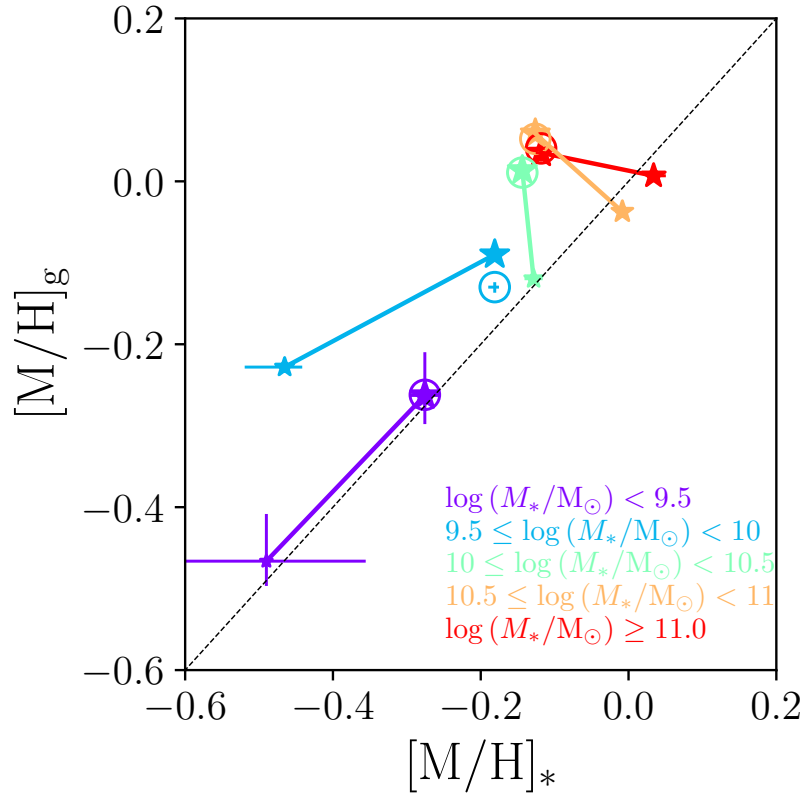


Figure 5.6: Evolution of stellar and gas metallicities with cosmic time. The median metallicities for the sample galaxies are determined for five different stellar mass bins. Three datapoints are plotted for each mass bin. Star-shaped datapoints denote mass-weighted mean stellar metallicity data derived from STARLIGHT and gas metallicity data from the FMR of Mannucci et al. (2010). The size of the star is proportional to the fraction of mass that had formed at that redshift. The larger stars therefore correspond to a lookback time of $10^{7.6}$ yr ($z \sim 0$), and the smaller stars to a lookback time of $10^{9.95}$ yr ($z \sim 1.4$; Wright, 2006). The open circles plot the stellar metallicities of the mass bins at a lookback time of $10^{7.6}$ yr against the present-day gas metallicities derived from measurements of the N2O2 ratio (Kewley & Dopita, 2002) to ensure the gas metallicities predicted by the FMR are plausible. The errorbars show the 1σ uncertainty on the median of each datapoint. The black diagonal line is a 1-to-1 relation, and does not represent a fit to the data.

the driving force behind their lengthy star formation timescales (as discussed in Section 4.4; see also Peterken et al., 2021b, Camps-Fariña et al., 2021, and Fraser-McKelvie et al., 2022), since stellar mass is the dominant factor influencing the gas metal content of galaxies (e.g. Tremonti et al., 2004). This leisurely pace allows these low-mass galaxies to thoroughly mix their gas between stellar generations, and thus they steadily increase both the metallicity of their stars – and the ISM which these stars pollute – over cosmic time, exactly as we see in Figure 5.6.

Figure 5.6 shows that high-mass galaxies have also increased their median gas metallicities since $z \sim 1.4$ (albeit less dramatically than their low-mass counterparts; again, this is consistent with the direct measurements made by Maiolino et al., 2008). In Section 4.4, we showed that a spiral galaxy with a stellar mass greater than $10^{10} M_{\odot}$ is far more likely to behave instead as an accreting box rather than a closed box. The accreting box model is similar to that of a closed box, but additionally allows for a steady stream of pristine gas to flow into the galaxy over time (Larson, 1972, 1976; Tinsley, 1974, 1980). Moreover, if galaxies do not accrete pristine gas, their star formation quenches rapidly; this effect is also far more pronounced for higher mass galaxies in the epoch since cosmic noon (E. Taylor et al. 2022, *in prep.*).

This infall of metal-poor gas allows these galaxies to produce a significant quantity of high-mass stars, which, upon their deaths, pollute the ISM with newly-forged metals. Subsequent generations of stars will be formed from this enriched material, which ultimately means that over cosmic time, the gas metallicity of high-mass galaxies gradually increases.

We might expect that the stellar populations in high-mass galaxies should be similarly enriched over cosmic time; however, Figure 5.6 demonstrates that the median stellar metallicity of such galaxies decreases at later times. This is a surprising result, and is in disagreement with other authors such as Panter et al. (2008) – who find essentially no change in the average stellar metallicity over this redshift interval – and Camps-Fariña et al. (2021, 2022) – while these authors do report a decrease in the average stellar metallicity since $\sim 10^{9.75}$ yr, this decrease is less pronounced than that which we report here. Why should this be? High-mass galaxies must accrete largely unmixed pristine gas over their lifetimes in order to satiate the demand required to maintain star formation at later times. Furthermore, these galaxies have been found to form the majority of their stars at earlier times (e.g. Beverage et al., 2021; Peterken et al., 2021b; Zhou et al., 2021; Fraser-McKelvie et al., 2022).

The decrease in the median stellar metallicities of these galaxies over cosmic time could, therefore, be a direct consequence of the pristine gas that they accrete. If this gas is not well mixed into the galaxy, it is probable that metal-poor stars will continuously form, even at very late times. These stars will still pollute the ISM with metals upon their deaths, raising the average metallicity of the gas in

these galaxies over time; however, even at late times the average stellar metallicity may be suppressed if such metal-poor stars always form from the supply of pristine gas. Further work will be required to investigate whether the stellar metallicities observed in high-mass galaxies in this work at the redshift of $z \sim 1.4$ around cosmic noon represents a local maximum, or whether the median stellar metallicities of such galaxies increases yet further at even higher redshifts.

5.5 Conclusions

We investigate the chemical evolution histories of both the stellar populations and the gas for a well-defined sample of 1619 spiral galaxies observed by MaNGA. Mass-weighted mean stellar metallicities are determined at low ($z \sim 0$) and high ($z \sim 1.4$) redshifts via the use of the full-spectrum stellar population synthesis code `STARLIGHT` (Cid Fernandes et al., 2005); gas metallicities are estimated at the same epochs using the FMR of Mannucci et al. (2010). We also calculate the present-day gas metallicities of the same galaxies by using the strong-line N2O2 calibration proposed by Kewley & Dopita (2002).

The evolution of both the MZ_{*R} and the MZ_{gR} are examined and discussed, in addition to the mass-dependence of the average stellar and gas metallicities of the galaxies. The results of these investigations are summarised below.

1. The MZ_{gR} is generically found to evolve in such a way that at a given mass, the gas within the galaxies becomes increasingly metal-rich with cosmic time. This result is in agreement with the findings of Maiolino et al. (2008), Moustakas et al. (2011), Zahid et al. (2013a, 2014b), Lian et al. (2018a,b), and Yates et al. (2021). Unlike the methods by which these authors determine the evolution of the MZ_{gR} , however, the method used in this work of tracking the evolution of the gas within low-redshift galaxies back to more distant lookback times via galactic archaeology allows for high-quality measurements of the gas metallicity even at high redshifts.
2. The median MZ_{*R} exhibits a general decline in stellar metallicity from $z \sim 1.4$ to $z \sim 0$, for the bulk of the explored sample, with the possible exception for the mass range $M_* < 10^{10} M_{\odot}$, in which little to no evolution is seen. The shape of the MZ_{*R} also changes: it is steeper at $z \sim 1.4$ and shallower at $z \sim 0$. The spread of the mass-weighted mean stellar metallicity data – comparable to that found by Gallazzi et al. (2005), Panter et al. (2008), and Beverage et al. (2021) – does evolve with cosmic time: the MZ_{*R} exhibits a much tighter relation at later times. In fact, at $z \sim 0$, the observed MZ_{*R} is more comparable to the MZ_{gR} of Tremonti et al. (2004) than, for instance, the MZ_{*R} of Panter et al. (2008), since these stars are forming from the same gas whose emission lines authors such as Tremonti et al. (2004) observe.

3. The results in this Chapter align well with those in Chapter 4, in which we concluded that low-mass spirals evolve as closed boxes, whereas high-mass spirals accrete a stream of relatively pristine gas over the course of their lives. We find in this work that low-mass galaxies steadily increase their stellar and gas metallicities over cosmic time since they form stars relatively slowly and are parsimonious with their gas reservoirs. High-mass galaxies, by contrast, have lower average stellar metallicities at later times. If the pristine gas is not particularly well-mixed into the galaxy upon accretion, large numbers of metal-poor stars will readily form in that galaxy even at very late times. This could result in the average stellar metallicities in high-mass spiral galaxies being suppressed at the present epoch.

Chapter 6

Conclusions and Future Work

At the start of this thesis, we asked the question: How do the chemical compositions of spiral galaxies change over cosmic time? In this concluding Chapter, we shall discuss to what extent this question has been addressed by this thesis. We shall also propose additional future science that could be undertaken using the work presented here as a basis.

Although the common thread throughout this thesis is the wealth of state-of-the-art data provided by SDSS-IV MaNGA (Bundy et al., 2015) that is ripe for scientific exploration – we discuss the data provided by MaNGA fully in Chapter 2 – not all of the Chapters in this thesis are directly aimed at answering this question. The results of Chapter 3 in particular are somewhat independent and are not necessarily concerned with the chemical evolution of galaxies. Therefore, we use MaNGA data throughout this thesis in different ways: in our investigation of dust attenuation (Chapter 3), we focus on a relatively small sample of galaxies but fully exploit the spatial resolution of MaNGA; by contrast, in Chapters 4 and 5 we turn to the main theme of chemical evolution, and utilise the huge number of galaxies observed by MaNGA to our advantage and analyse much larger samples of galaxies. We shall now summarise the results of Chapters 3, 4, and 5 in turn, before discussing the prospects for future work.

6.1 Dust Attenuation in Spiral Galaxies

In Chapter 3, we determine spatially resolved measurements for the dust attenuation in a well-defined sample of star-forming spiral galaxies observed by MaNGA. Two methods are used to calculate different measures of the dust attenuation. First, we use the Balmer decrement to obtain spatially resolved estimates for dust attenuation in the gas ($A_{V, \text{gas}}$) for each of the sample galaxies. Second, we use the full-spectrum stellar population synthesis code **STARLIGHT** (Cid Fernandes et al., 2005) to acquire equivalent estimates for the dust attenuation affecting the stellar

populations ($A_{V, \text{stars}}$) at the same locations in the same galaxies.

We first investigate the global trends in both $A_{V, \text{stars}}$ and $A_{V, \text{gas}}$. It is immediately apparent from our results that the overall mean value of $A_{V, \text{stars}}$ is consistently much lower than the mean $A_{V, \text{gas}}$ for a given galaxy. We investigate the dependence of dust attenuation on two global properties: stellar mass and $\text{H}\alpha$ derived specific star formation rate, $\text{sSFR}_{\text{H}\alpha}$ (relative to the star-forming main sequence; SFMS). While the mean $A_{V, \text{stars}}$ is not particularly influenced by stellar mass, the mean $A_{V, \text{gas}}$ increases for increasing stellar mass. Both the mean values of $A_{V, \text{stars}}$ and $A_{V, \text{gas}}$ increase as the $\text{sSFR}_{\text{H}\alpha}$ (relative to the SFMS) increases.

We also investigate the impact of these two global properties upon spatially resolved measurements of these dust attenuation metrics. First, we investigate how the variation of dust attenuation with galactocentric radius depends on stellar mass; second, we explore how this radial variation depends on $\text{sSFR}_{\text{H}\alpha}$ (relative to the SFMS). Both $A_{V, \text{stars}}$ and $A_{V, \text{gas}}$ exhibit negative radial gradients: they decrease for increasing galactocentric radius. The strength of the radial gradient for the $A_{V, \text{gas}}$ in particular appears to be strongly influenced by stellar mass, with higher mass galaxies exhibiting progressively steeper declines in $A_{V, \text{gas}}$ with radius. The $\text{sSFR}_{\text{H}\alpha}$ (relative to the SFMS) is a less influential property than stellar mass, but still seems to affect the radial gradient for the $A_{V, \text{gas}}$: galaxies close to (or above) the SFMS have steeper declines than those far below the SFMS.

We introduce a new dust attenuation quantity, the $A_{V, \text{gas}}$ excess (defined as $A_{V, \text{gas}} - A_{V, \text{stars}}$), which aims to provide an estimate for the dust attenuation only due to the giant molecular clouds in which stars are born. A negative radial gradient is also exhibited by the $A_{V, \text{gas}}$ excess, thus demonstrating that the radial gradient in the local $A_{V, \text{gas}}$ cannot be attributed to a gradient in the diffuse ISM alone; the concentration of clumpy dust must also increase nearer to the centres of galaxies. The gradient in the $A_{V, \text{gas}}$ excess is affected by stellar mass and $\text{sSFR}_{\text{H}\alpha}$ (relative to the SFMS) in a very similar way to the gradient in $A_{V, \text{gas}}$, likely because the gradients in $A_{V, \text{stars}}$ are not particularly influenced by these properties.

Finally, the spatial resolution of MaNGA is fully exploited to analyse the local values of $A_{V, \text{stars}}$, $A_{V, \text{gas}}$, and $A_{V, \text{gas}}$ excess. Each of these quantities increases as the local star formation rate per unit physical surface area increases. Our results suggest that variations in dust attenuation properties are likely driven predominantly by local physics, rather than by global properties of the galaxies.

While these results lend support to the conventional wisdom that stars are born in giant molecular birth clouds in which gas and very clumpy dust are highly concentrated, our results also imply that dust in high-mass galaxies likely has a clumpier distribution than in low-mass galaxies. Furthermore, we demonstrate that star-forming spiral galaxies probably exhibit a much higher concentration of both young stars and giant molecular birth clouds nearer to their centres than in their outer regions.

6.2 Chemical Evolution of Galaxies

We now turn to the task of answering the primary question posed at the start of this thesis. This investigation commences in Chapter 4 and continues into Chapter 5. The software **STARLIGHT**, which we used to obtain measures for the dust attenuation affecting the stellar populations for the sample of galaxies in Chapter 3, is now instead used to provide the metallicities for the populations in the galaxies analysed in both of these subsequent Chapters.

The **STARLIGHT** fitting process generates a set of weights for the mass contribution made by each of the input template spectra for every spaxel across the face of a given galaxy. These mass weights allow us to explore many different avenues in our investigations into the metallicities of the stars in spiral galaxies. In Chapter 4, the mass weights produced by **STARLIGHT** are used to construct stellar metallicity distribution functions for a sample of spiral galaxies observed by MaNGA. By contrast, in Chapter 5 we use these same mass weights to instead investigate the star formation histories, and also the stellar metallicity histories, for a very similar sample of galaxies.

6.2.1 Resolving the G-Dwarf Problem Outside the Milky Way

In Chapter 4, we address an issue which first arose many decades ago, when it was discovered that there are very few low-metallicity G-dwarf stars in the Solar neighbourhood. This observation, originally reported by van den Bergh (1962) and Schmidt (1963), is inconsistent with the simplest picture of a galaxy formed from a “closed box” of gas; this inconsistency later became known as the “G-dwarf problem”. In the Solar neighbourhood – and the wider Milky Way as a whole – the G-dwarf problem can be resolved by treating the Galaxy as an open system that accretes gas throughout its life.

Until the recent advent of large scale integral field unit (IFU) surveys, it has only been possible to measure the metallicity distributions of stars within the Milky Way (and certain nearby galaxies). We thus make use of high-quality spectral data from MaNGA in conjunction with **STARLIGHT** to acquire stellar metallicity distributions for the first large sample of spiral galaxies. The analysis presented in Chapter 4 shows that high-mass spirals generically show a similar deficit of low-metallicity stars, implying that the Milky Way’s history of gas accretion is common. By contrast, low-mass spirals show little sign of a G-dwarf problem, presenting the metallicity distribution that would be expected if such systems evolved as pretty much closed boxes.

This result implies that more massive spiral galaxies formed most of their stars at a rapid rate in a relatively short period of time. In order to keep up with the demand for gas to make more stars, such galaxies must pull in largely

unmixed pristine gas, adding this to material that has been enriched by the previous generations, and hence high-mass galaxies produce a much larger fraction of high-metallicity stars. By contrast, the less massive spiral systems have been slowly but steadily forming their stellar content over most of the lifetime of the Universe. Their more leisurely star formation rates allow these low-mass galaxies to mix recycled gas thoroughly between stellar generations, and they instead evolve effectively as closed boxes.

6.2.2 The Evolution of Chemical Compositions with Cosmic Time

We lastly investigate, for a similar sample of spiral galaxies, the chemical evolution histories of both the stellar populations and the gas in Chapter 5. As in Chapter 4, the mass-weighted metallicities of the stellar populations in these galaxies are determined using STARLIGHT. Gas metallicities are estimated using the fundamental metallicity relation (FMR) of Mannucci et al. (2010). These methods allow, respectively, the mean stellar and gas metallicities to be determined at both low ($z \sim 0$) and high ($z \sim 1.4$) redshifts. The gas metallicities yielded by the FMR at $z \sim 0$ are compared against those determined (at the present epoch) via the strong-line N2O2 calibration proposed by Kewley & Dopita (2002) for the same galaxies. We use these data to investigate the redshift evolution of both the stellar mass–stellar metallicity relation (MZ_{*R}) and the stellar mass–gas metallicity relation (MZ_gR). Furthermore, we also analyse the influence of stellar mass upon the redshift evolution of the average stellar and gas metallicities of the same galaxies.

Studying the redshift evolution of the MZ_gR reveals that the gas within the sample galaxies becomes increasingly metal-rich with cosmic time. By contrast, the median MZ_{*R} exhibits a general decline in stellar metallicity over the same time period (except for the mass range $M_* < 10^{10} M_\odot$, for which almost no evolution occurs). Furthermore, the shape of the MZ_{*R} also changes: it is steeper at $z \sim 1.4$ and shallower at $z \sim 0$. Indeed, at the present epoch, the observed MZ_{*R} is more comparable to the tight MZ_gR of Tremonti et al. (2004) than, for instance, the MZ_{*R} reported by Panter et al. (2008). This is likely because these stars are forming from the same gas whose emission lines are traditionally used to derive the relationship between stellar mass and gas metallicity.

So, how do the chemical compositions of spiral galaxies change over cosmic time? From the work presented in this thesis, the simple answer to this question seems to be that it depends upon the stellar mass of the galaxy in question. Low-mass galaxies, which we found typically behave as closed boxes, steadily increase both their average stellar and gas metallicities over cosmic time, likely because they form stars relatively slowly and are parsimonious with their gas reservoirs. This is consistent with a simple closed box model for chemical evolution, in which low-mass stars are generally expected to lock up metals in their cores, whilst high-mass stars pollute the surrounding gas with metals when they explode as supernovae.

(Of course, this simplified dichotomy ignores the presence of Type Ia supernovae, which release the metals locked up by the white dwarf remnants of low-mass main sequence stars in accreting binary systems). Nevertheless, subsequent generations of stars will be formed from this enriched material, and so the metallicities of the stars and gas in a closed box galaxy will increase over cosmic time. In high-mass galaxies, which we found typically behave as accreting boxes, the average gas metallicity increases over cosmic time (albeit less dramatically than in their low-mass counterparts), but we find that the average metallicity of the stars may actually be lower at later times. As we concluded in Chapter 4, such galaxies are more likely to form a significant proportion of their metal-poor stars at very late times. This tendency could be the reason why high-mass spiral galaxies are found to have lower average stellar metallicities at the present epoch than at $z \sim 1.4$.

Of course, the true answer to our original question is almost certainly more nuanced than this somewhat simplistic interpretation. In reality, we have likely only scratched the surface of the fertile field of galactic chemical evolution, and it will be fascinating to see what future astronomers will achieve with the riches of data from IFU surveys – such as MaNGA – and their planned successors alike.

6.3 Future Work

One of the ways the work presented in this thesis could be directly extended is by applying chemical evolution models other than just the accreting and closed box models to the MaNGA data (cf. Chapter 4). We discussed this prospect briefly in Section 1.3.3: one of the obvious comments to make upon this work is that we only consider inflows of gas into the system, but not outflows. Chemical evolution models which consider only outflows (but not inflows) of pristine gas are known as “leaky box” models (e.g. Hartwick, 1976); models which consider both inflows and outflows in tandem are referred to as “bathtub models” (e.g. Finlator & Davé, 2008; Lilly et al., 2013; Belfiore et al., 2019a). We do not consider these models during our investigation of the G-dwarf problem in Chapter 4, simply because many previous authors have found that models which consider the effects of gas outflows are not necessary in order to solve the G-dwarf problem in the Solar neighbourhood: only inflows of gas really need to be considered in order to solve this issue (e.g. Tinsley, 1974, 1975; Tinsley & Larson, 1978). Therefore, we choose not to complicate the relatively simple investigation we undertake in this thesis by considering the impact of outflows. There is, however, no reason why future authors could not extend our analysis to consider the effects of either the leaky box and/or bathtub model upon the stellar metallicity distributions of MaNGA galaxies, if they were so inclined.

Furthermore, as work by Zhou et al. (2022) demonstrates, it is possible to fit chemical evolution models – such as those described above – directly to MaNGA

spectra. This would be a very interesting avenue to explore if implemented in conjunction with the results presented in Chapters 4 and 5 of this thesis.

As discussed at the start of Chapter 2, the golden era of IFU spectroscopy is only just beginning. The next SDSS generation, SDSS-V (Kollmeier et al., 2017), will take up the mantle with even higher-quality data being provided by projects such as the Local Volume Mapper (LVM; Konidaris et al., 2020). One of the limitations of MaNGA is that it has a spatial resolution of $\sim 2.5''$ full width at half-maximum (Yan et al., 2016a). This resolution corresponds to an angular size of a couple of kpc at the average redshift of a galaxy in the MaNGA sample, which is typically too large to resolve individual H II regions which may be only a couple of hundred pc across; furthermore, the limited resolution of MaNGA was one of the main reasons why, in Section 3.6.1, we were unable to determine whether dust lanes were located in the spiral arm or inter-arm region of the MaNGA galaxies. By contrast, the LVM will be able to resolve individual star-forming structures, giant molecular clouds, and H II regions (Kollmeier et al., 2017); clearly, this level of detail would be advantageous for some of the work presented in this thesis, especially in Chapter 3 where we fully leverage the spatial resolution of MaNGA.

It will also be particularly interesting and relevant to the future of this work when both MOONS (Cirasuolo et al., 2020) and HARMONI (Laurent et al., 2018) commence observations at the Very Large and Extremely Large Telescopes, respectively. Planned projects for the MOONS instrument include the MOONS REDdened Milky WAY (REDWAY; Gonzalez et al., 2020) survey, and the MOONS Redshift-Intensive Survey Experiment (MOONRISE; Maiolino et al., 2020). Both of these projects will be able to enhance the work presented in this thesis in very different ways. The REDWAY survey aims to sample $\sim 500\,000$ stars in the plane of the Milky Way (Gonzalez et al., 2020), which will provide state-of-the-art spectroscopic data for deeper analysis of the distribution of stellar metallicity in the Galaxy. MOONRISE, meanwhile, aims to provide spectroscopic observations for around 500 000 galaxies in the redshift range $0.9 < z < 2.6$ in order to probe the properties of their stellar populations and ISMs (Maiolino et al., 2020). Furthermore, one of the specific science goals of MOONRISE is to investigate the metallicity evolution of galaxies by assessing the evolution of the stellar mass–gas metallicity relation and the fundamental metallicity relation (Maiolino et al., 2020). Clearly, the results from the MOONRISE project will be of extreme relevance to anyone looking to directly build upon the work presented in this thesis.

HARMONI aims to provide IFU observations of galaxies up to very high redshifts – possibly even to $z \sim 10$ (Thatte et al., 2021). This represents a much deeper redshift range than that probed by MaNGA. As such, the galactic archaeology performed on the sample of MaNGA galaxies in Chapter 5 would be greatly enhanced by HARMONI data: we would be able use observations of galaxies in the high-redshift Universe as a starting point, rather than an ending point, to completely excavate their chemical evolution histories.

It is our hope that the work presented in this thesis may be used as a springboard for other astronomers wishing to delve deeper into the mysteries of galactic chemical evolution. In addition, upcoming IFU surveys, such as those described above, will surely provide us with a more detailed understanding of this field of research. We can only wait and see what the future will bring.

Bibliography

- Abazajian K., Adelman-McCarthy J.K., Ageros M.A. et al., 2003. *The First Data Release of the Sloan Digital Sky Survey*. *AJ*, 126, 4, 2081–2086.
- Abazajian K.N., Adelman-Mccarthy J.K., Agüeros M.A. et al., 2009. *The Seventh Data Release of the Sloan Digital Sky Survey*. *ApJS*, 182, 2, 543–558.
- Abdurro’uf, Accetta K., Aerts C. et al., 2022. *The Seventeenth Data Release of the Sloan Digital Sky Surveys: Complete Release of MaNGA, MaStar, and APOGEE-2 Data*. *ApJS*, 259, 2, 35.
- Abolfathi B., Aguado D.S., Aguilar G. et al., 2018. *The Fourteenth Data Release of the Sloan Digital Sky Survey: First Spectroscopic Data from the Extended Baryon Oscillation Spectroscopic Survey and from the Second Phase of the Apache Point Observatory Galactic Evolution Experiment*. *ApJS*, 235, 2, 42.
- Aguado D.S., Ahumada R., Almeida A. et al., 2019. *The Fifteenth Data Release of the Sloan Digital Sky Surveys: First Release of MaNGA-derived Quantities, Data Visualization Tools, and Stellar Library*. *ApJS*, 240, 2, 23.
- Arribas S., del Burgo C., Carter D. et al., 1998. *INTEGRAL: an Optical-Fiber System for 2-D Spectroscopy on the 4.2-in William Herschel Telescope*. *ASPC*, 152, 149.
- Asa’d R.S., Vazdekis A., Cervino M. et al., 2017. *Young LMC clusters: the role of red supergiants and multiple stellar populations in their integrated light and CMDs*. *MNRAS*, 471, 3, 3599–3614.
- Asplund M., Grevesse N., Sauval A.J. et al., 2009. *The Chemical Composition of the Sun*. *ARA&A*, 47, 1, 481–522.
- Audouze J. & Tinsley B.M., 1976. *Chemical evolution of galaxies*. *ARA&A*, 14, 43.
- Bacon R., Adam G., Baranne A. et al., 1988. *The Integral Field Spectrograph TIGER*. *Proc. ESO Conf.*, Garching, 30, 1185.

- Bacon R., Adam G., Baranne A. et al., 1995. *3D spectrography at high spatial resolution. I. Concept and realization of the integral field spectrograph TIGER*. A&AS, 113, 347.
- Baldwin J.A., Phillips M.M. & Terlevich R., 1981. *Classification parameters for the emission-line spectra of extragalactic objects*. PASP, 93, 5–19.
- Barden S.C. & Wade R.A., 1988. *DensePak and spectral imaging with fiber optics*. Proc. ASP Conf. in Tucson, AZ, 3, 113.
- Belfiore F., Maiolino R., Bundy K. et al., 2015. *P-MaNGA Galaxies: Emission-lines properties – gas ionization and chemical abundances from prototype observations*. MNRAS, 449, 1, 867–900.
- Belfiore F., Maiolino R., Maraston C. et al., 2016. *SDSS IV MaNGA-spatially resolved diagnostic diagrams: A proof that many galaxies are LIERs*. MNRAS, 461, 3, 3111–3134.
- Belfiore F., Vincenzo F., Maiolino R. et al., 2019a. *From ‘bathtub’ galaxy evolution models to metallicity gradients*. MNRAS, 487, 1, 456–474.
- Belfiore F., Westfall K.B., Schaefer A. et al., 2019b. *The Data Analysis Pipeline for the SDSS-IV MaNGA IFU Galaxy Survey: Emission-Line Modeling*. AJ, 158, 4, 160.
- Bell E.F. & Kennicutt Jr. R.C., 2001. *A Comparison of Ultraviolet Imaging Telescope Far-Ultraviolet and H α Star Formation Rates*. ApJ, 548, 2, 681–693.
- Benjamin R.A., Churchwell E., Babler B.L. et al., 2005. *First GLIMPSE Results on the Stellar Structure of the Galaxy*. ApJ, 630, 2, L149–L152.
- Bertelli G., Bressan A., Chiosi C. et al., 1994. *Theoretical isochrones from models with new radiative opacities*. A&AS, 106, 275.
- Bertelli G., Girardi L., Marigo P. et al., 2008. *Scaled solar tracks and isochrones in a large region of the Z-Y plane I. From the ZAMS to the TP-AGB end for 0.15 - 2.5 Mo stars*. A&A, 484, 3, 815–830.
- Beverage A.G., Kriek M., Conroy C. et al., 2021. *Elemental Abundances and Ages of $z \sim 0.7$ Quiescent Galaxies on the Mass–Size Plane: Implication for Chemical Enrichment and Star Formation Quenching*. ApJ, 917, 1, L1.
- Bigiel F., Leroy A., Walter F. et al., 2008. *The Star Formation Law in Nearby Galaxies on Sub-Kpc Scales*. AJ, 136, 6, 2846–2871.
- Binney J. & Merrifield M., 1998. *Galactic Astronomy*. Princeton University Press, Princeton.

- Blanc G.A., Kewley L., Vogt F.P. et al., 2015. *IZI: Inferring the gas phase metallicity (Z) and ionization parameter (q) of ionized nebulae using bayesian statistics*. ApJ, 798, 2, 99.
- Blanton M.R., Schlegel D.J., Strauss M.A. et al., 2005. *New York University Value-Added Galaxy Catalog: A Galaxy Catalog Based on New Public Surveys*. AJ, 129, 6, 2562–2578.
- Blanton M.R. & Roweis S., 2007. *K-corrections and filter transformations in the ultraviolet, optical, and near infrared*. AJ, 133, 2, 734–754.
- Blanton M.R., Kazin E., Muna D. et al., 2011. *Improved background subtraction for the Sloan Digital Sky Survey images*. AJ, 142, 1, 31.
- Blanton M.R., Bershady M.A., Abolfathi B. et al., 2017. *Sloan Digital Sky Survey IV: Mapping the Milky Way, Nearby Galaxies, and the Distant Universe*. AJ, 154, 1, 28.
- Boggess A., Carr F.A., Evans D.C. et al., 1978. *The IUE spacecraft and instrumentation*. Nature, 275, 5679, 372–377.
- Boissier S., Boselli A., Buat V. et al., 2004. *The radial extinction profiles of late-type galaxies*. A&A, 424, 2, 465–476.
- Bolatto A.D., Wong T., Utomo D. et al., 2017. *The EDGE-CALIFA Survey: Interferometric Observations of 126 Galaxies with CARMA*. ApJ, 846, 2, 159.
- Boquien M., Burgarella D., Roehlly Y. et al., 2019. *CIGALE: A python Code Investigating GALaxy Emission*. A&A, 622, 103.
- Boselli A. & Gavazzi G., 2006. *Environmental Effects on Late-Type Galaxies in Nearby Clusters*. PASJ, 118, 842, 517–559.
- Branch D. & Tammann G.A., 1992. *Type Ia supernovae as standard candles*. ARA&A, 30, 1, 359–389.
- Bresolin F., Pietrzynski G., Urbaneja M.A. et al., 2006. *The Araucaria Project. VLT spectra of blue supergiants in WLM: classification and first abundances*. ApJ, 648, 2, 1007–1019.
- Brinchmann J., Charlot S., White S.D.M. et al., 2004. *The physical properties of star-forming galaxies in the low-redshift Universe*. MNRAS, 351, 4, 1151–1179.
- Brodie J.P., Romanowsky A.J., Strader J. et al., 2014. *The SAGES Legacy Unifying Globulars and Galaxies Survey (SLUGGS): Sample definition, methods, and initial results*. ApJ, 796, 1, 52.
- Buat V., Deharveng J.M. & Donas J., 1989. *Star formation rate and gas surface density in late-type galaxies*. A&A, 223, 42–46.

- Buat V., Takeuchi T.T., Iglesias-Paramo J. et al., 2006. *The Local Universe as Seen in Far-Infrared and in Far-Ultraviolet: A Global Point of View on the Local Recent Star Formation*. ApJS, 173, 2, 404–414.
- Bundy K., Bershady M.A., Law D.R. et al., 2015. *Overview of the SDSS-IV MaNGA Survey: Mapping Nearby Galaxies at Apache Point Observatory*. ApJ, 798, 1, 7.
- Calzetti D., Kinney A.L. & Storchi-Bergmann T., 1994. *Dust extinction of the stellar continua in starburst galaxies: The ultraviolet and optical extinction law*. ApJ, 429, 582.
- Calzetti D., Armus L., Bohlin R.C. et al., 2000. *The Dust Content and Opacity of Actively Star-forming Galaxies*. ApJ, 533, 2, 682–695.
- Calzetti D., 2001. *The Dust Opacity of Star-forming Galaxies*. PASP, 113, 790, 1449–1485.
- Calzetti D., Kennicutt R.C., Bianchi L. et al., 2005. *Star Formation in NGC5194 (M51a): The Panchromatic View from GALEX to Spitzer*. ApJ, 633, 2, 871–893.
- Camps-Fariña A., Sanchez S.F., Lacerda E.A.D. et al., 2021. *Evolution of the chemical enrichment and the Mass-Metallicity relation in CALIFA galaxies*. MNRAS, 504, 3, 3478–3493.
- Camps-Fariña A., Sánchez S.F., Mejía-Narváez A. et al., 2022. *Chemical evolution history of MaNGA galaxies*. eprint (arXiv:2203.01159).
- Cappellari M. & Emsellem E., 2004. *Parametric Recovery of Line-of-Sight Velocity Distributions from Absorption-Line Spectra of Galaxies via Penalized Likelihood*. PASP, 116, 816, 138–147.
- Cappellari M., Emsellem E., Krajnović D. et al., 2011a. *The ATLAS 3D project - VII. A new look at the morphology of nearby galaxies: The kinematic morphology-density relation*. MNRAS, 416, 3, 1680–1696.
- Cappellari M., Emsellem E., Krajnović D. et al., 2011b. *The ATLAS3D project - I. A volume-limited sample of 260 nearby early-type galaxies: Science goals and selection criteria*. MNRAS, 413, 2, 813–836.
- Cappellari M., 2017. *Improving the full spectrum fitting method: Accurate convolution with Gauss-Hermite functions*. MNRAS, 466, 1, 798–811.
- Cardelli J.A., Clayton G.C. & Mathis J.S., 1989. *The relationship between infrared, optical, and ultraviolet extinction*. ApJ, 345, 245.

- Carnall A.C., McLure R.J., Dunlop J.S. et al., 2018. *Inferring the star formation histories of massive quiescent galaxies with BAGPIPES: Evidence for multiple quenching mechanisms*. MNRAS, 480, 4, 4379–4401.
- Casuso E. & Beckman J.E., 2004. *The K-dwarf problem and the time-dependence of gaseous accretion to the Galactic disc*. A&A, 419, 1, 181–190.
- Catalán-Torrecilla C., de Paz A.G., Castillo-Morales A. et al., 2015. *Star Formation in the Local Universe from the CALIFA sample. I. Calibrating the SFR using IFS data*. A&A, 584, A87.
- Chabrier G., 2003. *Galactic Stellar and Substellar Initial Mass Function*. PASP, 115, 809, 763–795.
- Chandar R., Chien L.H., Meidt S. et al., 2017. *Clues to the Formation of Spiral Structure in M51 from the Ages and Locations of Star Clusters*. ApJ, 845, 1, 78.
- Chandrasekhar S., 1931. *The Maximum Mass of Ideal White Dwarfs*. ApJ, 74, 81.
- Charlot S. & Fall S.M., 2000. *A Simple Model for the Absorption of Starlight by Dust in Galaxies*. ApJ, 539, 2, 718–731.
- Cherinka B., Andrews B.H., Sánchez-Gallego J. et al., 2018. *Marvin: A Toolkit for Streamlined Access and Visualization of the SDSS-IV MaNGA Data Set*. AJ, 158, 2, 74.
- Cheung E., Athanassoula E., Masters K.L. et al., 2013. *Galaxy zoo: Observing secular evolution through bars*. ApJ, 779, 2, 162.
- Chiappini C., Matteucci F. & Gratton R., 1997. *The Chemical Evolution of the Galaxy: the two-infall model*. ApJ, 477, 2, 765–780.
- Chiappini C., Matteucci F. & Romano D., 2001. *Abundance Gradients and the Formation of the Milky Way*. ApJ, 554, 2, 1044–1058.
- Cid Fernandes R., Mateus A., Sodré L. et al., 2005. *Semi-empirical analysis of Sloan Digital Sky Survey galaxies – I. Spectral synthesis method*. MNRAS, 358, 2, 363–378.
- Cid Fernandes R. & González Delgado R.M., 2010. *Testing spectral models for stellar populations with star clusters - I. Methodology*. MNRAS, 403, 2, 780–796.
- Cid Fernandes R., Pérez E., García Benito R. et al., 2013. *Resolving galaxies in time and space: I. Applying STARLIGHT to CALIFA datacubes*. A&A, 557, 86.

- Cid Fernandes R., González Delgado R.M., García-Benito R. et al., 2014. *Resolving galaxies in time and space: II: Uncertainties in the spectral synthesis of datacubes*. A&A, 561, 130.
- Cid Fernandes R., 2018. *On tests of full spectral fitting algorithms*. MNRAS, 480, 4, 4480–4488.
- Cirasuolo M., Fairley A., Rees P. et al., 2020. *MOONS: The New Multi-Object Spectrograph for the VLT*. Messenger, 180, 10–17.
- Colombo D., Kalinova V., Utomo D. et al., 2017. *The EDGE-CALIFA survey: The influence of galactic rotation on the molecular depletion time across the Hubble sequence*. MNRAS, 475, 2, 1791–1808.
- Considère S., Coziol R., Contini T. et al., 2000. *Starbursts in barred spiral galaxies IV. On young bars and the formation of abundance gradients*. A&A, 356, 1, 89–101.
- Cortese L., Fritz J., Bianchi S. et al., 2014. *PACS photometry of the Herschel reference survey - far-infrared/ submillimetre colours as tracers of dust properties in nearby galaxies*. MNRAS, 440, 1, 942–956.
- Cresci G., Mannucci F. & Curti M., 2019. *Fundamental metallicity relation in CALIFA, SDSS-IV MaNGA, and high- z galaxies*. A&A, 627, 42.
- Croom S.M., Lawrence J.S., Bland-Hawthorn J. et al., 2012. *The Sydney-AAO Multi-object Integral Field Spectrograph*. MNRAS, 421, 1, 872–893.
- Curti M., Mannucci F., Cresci G. et al., 2020. *The mass-metallicity and the fundamental metallicity relation revisited on a fully Te-based abundance scale for galaxies*. MNRAS, 491, 1, 944–964.
- da Cunha E., Charlot S. & Elbaz D., 2008. *A simple model to interpret the ultraviolet, optical and infrared emission from galaxies*. MNRAS, 388, 4, 1595–1617.
- da Cunha E., Eminian C., Charlot S. et al., 2010. *New insight into the relation between star formation activity and dust content in galaxies*. MNRAS, 403, 4, 1894–1908.
- Daddi E., Dickinson M., Morrison G. et al., 2007. *Multiwavelength Study of Massive Galaxies at $z \sim 2$. I. Star Formation and Galaxy Growth*. ApJ, 670, 1, 156–172.
- Daddi E., Elbaz D., Walter F. et al., 2010. *Different star formation laws for disks versus starbursts at low and high redshifts*. ApJ, 714, 1, 118–122.

- Dalcanton J.J., Yoachim P. & Bernstein R.A., 2004. *The Formation of Dust Lanes: Implications for Galaxy Evolution*. ApJ, 608, 1, 189–207.
- Dawson K.S., Schlegel D.J., Ahn C.P. et al., 2013. *The Baryon Oscillation Spectroscopic Survey of SDSS-III*. AJ, 145, 1, 2013.
- Dawson K.S., Kneib J.P., Percival W.J. et al., 2016. *The SDSS-IV extended Baryon Oscillation Spectroscopic Survey: Overview and early data*. AJ, 151, 2, 44.
- de Amorim A.L., García-Benito R., Fernandes R.C. et al., 2017. *The PyCASSO database: Spatially resolved stellar population properties for CALIFA galaxies*. MNRAS, 471, 3, 3727–3752.
- De Looze I., Fritz J., Baes M. et al., 2014. *High-resolution, 3D radiative transfer modeling: I. The grand-design spiral galaxy M51*. A&A, 571, A69.
- de Vaucouleurs G., 1959. *Classification and Morphology of External Galaxies*. Handbuch der Physik, 53, 275–310.
- de Vaucouleurs G., 1963. *Revised Classification of 1500 Bright Galaxies*. ApJS, 8, 31.
- de Vaucouleurs G., 1964. *Interpretation of velocity distribution of the inner regions of the Galaxy*. IAUSymp, 20, 195.
- de Zeeuw P.T., Bureau M., Emsellem E. et al., 2002. *The SAURON project. II. Sample and early results*. MNRAS, 329, 3, 513–530.
- Domínguez A., Siana B., Henry A.L. et al., 2013. *Dust extinction from Balmer decrements of star-forming galaxies at $0.75 \leq z \leq 1.5$ with Hubble Space Telescope / Wide-Field-Camera 3 spectroscopy from the WFC3 Infrared Spectroscopic Parallel Survey*. ApJ, 763, 2, 145.
- Draine B., 1989. *On the Interpretation of the λ 2175 Å Feature*. IAUSymp, 135, 313.
- Draine B.T. & Lee H.M., 1984. *Optical properties of interstellar graphite and silicate grains*. ApJ, 285, 89.
- Draine B.T. & Anderson N., 1985. *Temperature fluctuations and infrared emission from interstellar grains*. ApJ, 292, 494.
- Driver S.P., Popescu C.C., Tuffs R.J. et al., 2007. *The Millennium Galaxy Catalogue: the B-band attenuation of bulge and disc light and the implied cosmic dust and stellar mass densities*. MNRAS, 379, 3, 1022–1036.
- Drory N., MacDonald N., Bershadsky M.A. et al., 2015. *The MaNGA integral field unit fiber feed system for the Sloan 2.5 m telescope*. AJ, 149, 2, 77.

- Easton C., 1913. *A Photographic Chart of the Milky way and the Spiral Theory of the Galactic System*. ApJ, 37, 105.
- Egusa F., Sofue Y. & Nakanishi H., 2004. *Offsets between H-alpha and CO arms of a spiral galaxy NGC 4254: A New Method for Determining the Pattern Speed of Spiral Galaxies*. PASJ, 56, 6, L45–L48.
- Egusa F., Kohno K., Sofue Y. et al., 2009. *Determining Star Formation Timescale and Pattern Speed in Nearby Spiral Galaxies*. ApJ, 697, 2, 1870–1891.
- Elbaz D., Daddi E., Le Borgne D. et al., 2007. *The reversal of the star formation-density relation in the distant universe*. A&A, 468, 1, 33–48.
- Ellison S.L., Patton D.R., Simard L. et al., 2008. *Clues to the Origin of the Mass-Metallicity Relation: Dependence on Star Formation Rate and Galaxy Size*. ApJ, 672, 2, L107–L110.
- Elmegreen D.M. & Elmegreen B.G., 1987. *Arm classifications for spiral galaxies*. ApJ, 314, 3.
- Escala I., Wetzel A., Kirby E.N. et al., 2018. *Modelling chemical abundance distributions for dwarf galaxies in the Local Group: The impact of turbulent metal diffusion*. MNRAS, 474, 2, 2194–2211.
- Falcón-Barroso J., Sánchez-Blázquez P., Vazdekis A. et al., 2011. *An updated MILES stellar library and stellar population models*. A&A, 532, 95.
- Fanelli M.N., O’Connell R.W. & Thuan T.X., 1988. *Spectral synthesis in the ultraviolet. II – Stellar populations and star formation in blue compact galaxies*. ApJ, 334, 665.
- Feltzing S., Bowers J.B. & Agertz O., 2020. *Constraining churning and blurring in the Milky Way using large spectroscopic surveys – an exploratory study*. MNRAS, 493, 1, 1419–1433.
- Ferrière K.M., 2001. *The interstellar environment of our galaxy*. Rev. Mod. Phys., 73, 4, 1031–1066.
- Finlator K. & Davé R., 2008. *The origin of the galaxy mass-metallicity relation and implications for galactic outflows*. MNRAS, 385, 4, 2181–2204.
- Fitzpatrick E.L., 1999. *Correcting for the Effects of Interstellar Extinction*. PASP, 111, 755, 63–75.
- Fontanot F., Calabrò A., Talia M. et al., 2021. *The evolution of the mass-metallicity relations from the VANDELS survey and the GAEA semi-analytic model*. MNRAS, 504, 3, 4481–4492.

- Förster Schreiber N.M. & Wuyts S., 2020. *Star-Forming Galaxies at Cosmic Noon*. ARA&A, 58, 661–725.
- Foyle K., Wilson C.D., Mentuch E. et al., 2012. *The Dust and Gas Properties of M83*. MNRAS, 421, 4, 2917–2929.
- Frankel N., Rix H.W., Ting Y.S. et al., 2018. *Measuring Radial Orbit Migration in the Milky Way Disk*. ApJ, 865, 2, 96.
- Fraser-McKelvie A., Merrifield M. & Aragón-Salamanca A., 2019. *From the Outside Looking in: What can Milky Way Analogues Tell us About the Star Formation Rate of Our Own Galaxy?* MNRAS, 489, 4, 5030–5036.
- Fraser-McKelvie A., Aragón-Salamanca A., Merrifield M. et al., 2020a. *SDSS-IV MaNGA: spatially resolved star formation in barred galaxies*. MNRAS, 495, 4, 4158–4169.
- Fraser-McKelvie A., Merrifield M., Aragón-Salamanca A. et al., 2020b. *SDSS-IV MaNGA: The link between bars and the early cessation of star formation in spiral galaxies*. MNRAS, 499, 1, 1116–1125.
- Fraser-McKelvie A., Cortese L., Groves B. et al., 2022. *The SAMI Galaxy Survey: the drivers of gas and stellar metallicity differences in galaxies*. MNRAS, 510, 1, 320–333.
- Fu J., Kauffmann G., Li C. et al., 2012. *The effect of star formation on the redshift evolution of interstellar metals, atomic and molecular gas in galaxies*. MNRAS, 424, 4, 2701–2714.
- Gallazzi A., Charlot S., Brinchmann J. et al., 2005. *The ages and metallicities of galaxies in the local universe*. MNRAS, 362, 1, 41–58.
- Galliano F., Galametz M. & Jones A.P., 2017. *The interstellar dust properties of nearby galaxies*. ARA&A, 56, 1, 673–713.
- García-Benito R., González Delgado R.M., Pérez E. et al., 2019. *Spatially resolved mass-to-light from the CALIFA survey: Mass-to-light ratio vs. color relations*. A&A, 621, 120.
- Garn T. & Best P., 2010. *Predicting dust extinction from the stellar mass of a galaxy*. MNRAS, 409, 1, 421–432.
- Ge J., Yan R., Cappellari M. et al., 2018. *Recovering stellar population parameters via two full-spectrum fitting algorithms in the absence of model uncertainties*. MNRAS, 478, 2, 2633–2649.
- Gilbank D.G., Baldry I.K., Balogh M.L. et al., 2010. *The local star formation rate density: assessing calibrations using [O II], H and UV luminosities*. MNRAS, 405, 4, 2594–2614.

- Gilbert K.M., Kirby E.N., Escala I. et al., 2019. *Elemental Abundances in M31: First Alpha and Iron Abundance Measurements in M31's Giant Stellar Stream*. ApJ, 883, 2, 128.
- Giovanelli R., Haynes M.P., Salzer J.J. et al., 1995. *Dependence on Luminosity of Photometric Properties of Disk Galaxies: Surface Brightness, Size, and Internal Extinction*. AJ, 110, 1059.
- Girardi L., Bressan A., Bertelli G. et al., 2000. *Evolutionary tracks and isochrones for low- and intermediate-mass stars: from 0.15 to 7 solar masses, and from $z = 0.0004$ to 0.03*. A&AS, 141, 3, 371–383.
- Glazebrook K., Blake C., Economou F. et al., 1999. *Measurement of the star formation rate from H α in field galaxies at $z = 1$* . MNRAS, 306, 4, 843–856.
- Gliese W., 1969. *Catalogue of Nearby Stars. Edition 1969*. Veroeff. Astron. Rechen-Inst., 22, 1.
- Goddard D., Thomas D., Maraston C. et al., 2016. *SDSS-IV MaNGA: Spatially resolved star formation histories in galaxies as a function of galaxy mass and type*. MNRAS, 466, 4731–4758.
- Gonzalez O.A., Mucciarelli A., Origlia L. et al., 2020. *MOONS Surveys of the Milky Way and its Satellites*. Messenger, 180, 18–25.
- González Delgado R.M., Cid Fernandes R., García-Benito R. et al., 2014. *Insights on the stellar mass-metallicity relation from the califa survey*. ApJ, 791, 1, 16.
- González Delgado R.M., García-Benito R., Pérez E. et al., 2015. *The CALIFA survey across the Hubble sequence*. A&A, 581, A103.
- González Delgado R.M., Cid Fernandes R., Pérez E. et al., 2016. *Star formation along the Hubble sequence: Radial structure of the star formation of CALIFA galaxies*. A&A, 590, A44.
- González Delgado R.M., Pérez E., Cid Fernandes R. et al., 2017. *Spatially-resolved star formation histories of CALIFA galaxies: Implications for galaxy formation*. A&A, 607, 128.
- Gordon K.D. & Clayton G.C., 1998. *Starburst-like Dust Extinction in the Small Magellanic Cloud*. ApJ, 500, 2, 816–824.
- Gratton R., Carretta E., Matteucci F. et al., 1996. *The [Fe/O] Ratio in Field Stars and the History of Star Formation of the Solar Neighbourhood*. ASPC, 92, 307.
- Greener M.J., Aragón-Salamanca A., Merrifield M.R. et al., 2020. *SDSS-IV MaNGA: spatially resolved dust attenuation in spiral galaxies*. MNRAS, 495, 2, 2305–2320.

- Greener M.J., Merrifield M., Aragón-Salamanca A. et al., 2021. *SDSS-IV MaNGA: The ‘G-dwarf problem’ revisited*. MNRAS, 502, 1, L95–L98.
- Greener M.J., Merrifield M., Aragón-Salamanca A. et al., 2022. *SDSS-IV MaNGA: the chemical co-evolution of gas and stars in spiral galaxies*. MNRAS.
- Grootes M.W., Tuffs R.J., Popescu C.C. et al., 2017. *Galaxy And Mass Assembly (GAMA): Gas Fueling of Spiral Galaxies in the Local Universe. I. The Effect of the Group Environment on Star Formation in Spiral Galaxies*. AJ, 153, 3, 111.
- Groves B., Brinchmann J. & Walcher C.J., 2012. *The Balmer decrement of Sloan Digital Sky Survey galaxies*. MNRAS, 419, 2, 1402–1412.
- Gunn J.E., Carr M., Rockosi C. et al., 1998. *The Sloan Digital Sky Survey Photometric Camera*. AJ, 116, 6, 3040–3081.
- Gunn J.E., Siegmund W.A., Mannery E.J. et al., 2006. *The 2.5 m Telescope of the Sloan Digital Sky Survey*. AJ, 131, 4, 2332–2359.
- Guo K., Zheng X.Z., Wang T. et al., 2015. *The star formation main sequence: The dependence of specific star formation rate and its dispersion on galaxy stellar mass*. ApJ, 808, 2, L49.
- Hägele G.F., Díaz Á.I., Terlevich E. et al., 2008. *Precision abundance analysis of bright H II galaxies*. MNRAS, 383, 1, 209–229.
- Hart R.E., Bamford S.P., Willett K.W. et al., 2016. *Galaxy Zoo: comparing the demographics of spiral arm number and a new method for correcting redshift bias*. MNRAS, 461, 4, 3663–3682.
- Hart R.E., Bamford S.P., Hayes W.B. et al., 2017a. *Galaxy Zoo and SPARCFIRE: Constraints on spiral arm formation mechanisms from spiral arm number and pitch angles*. MNRAS, 472, 2, 2263–2279.
- Hart R.E., Bamford S.P., Casteels K.R.V. et al., 2017b. *Galaxy Zoo: star formation versus spiral arm number*. MNRAS, 468, 2, 1850–1863.
- Hart R.E., Bamford S.P., Keel W.C. et al., 2018. *Galaxy Zoo: Constraining the origin of spiral arms*. MNRAS, 478, 1, 932–949.
- Hartwick F.D.A., 1976. *The Chemical Evolution of the Galactic Halo*. ApJ, 209, 418.
- Hayden M.R., Bovy J., Holtzman J.A. et al., 2015. *Chemical Cartography with APOGEE: Metallicity Distribution Functions and the Chemical Structure of the Milky Way Disk*. ApJ, 808, 2, 132.
- Heckman T.M., 1980. *Star formation and activity in the nuclei of barred galaxies*. A&A, 88, 3, 365.

- Heckman T.M., Robert C., Leitherer C. et al., 1998. *The Ultraviolet Spectroscopic Properties of Local Starbursts: Implications at High-Redshift*. ApJ, 503, 2, 646–661.
- Helou G., 1986. *The IRAS colors of normal galaxies*. ApJ, 311, L33.
- Henry L.C. & Greenstein J.L., 1941. *Diffuse radiation in the Galaxy*. ApJ, 93, 70.
- Herbst E., 1995. *Chemistry in the Interstellar Medium*. ARPC, 46, 1, 27–54.
- Herschel J., 1876. *Memoir and correspondence of Caroline Herschel*. John Murray, London.
- Herschel W., 1785. *On the Construction of the Heavens*. Philos. Trans. R. Soc. Lond., 75, 213–266.
- Hippelein H., Haas M., Tuffs R.J. et al., 2003. *The spiral galaxy M33 mapped in the FIR by ISOPHOT: A spatially resolved study of the warm and cold dust*. A&A, 407, 1, 137–146.
- Holmberg J., Nordstrom B. & Andersen J., 2007. *The Geneva-Copenhagen Survey of the Solar neighbourhood II. New uvby calibrations and rediscussion of stellar ages, the G dwarf problem, age-metallicity diagram, and heating mechanisms of the disk*. A&A, 475, 2, 519–537.
- Holwerda B.W., Gonzalez R.A., Allen R.J. et al., 2005. *The Opacity of Spiral Galaxy Disks IV: Radial Extinction Profiles from Counts of Distant Galaxies seen through Foreground Disks*. AJ, 129, 3, 1396–1411.
- Holwerda B.W., Bianchi S., Baes M. et al., 2012. *New HERSchel Multi-wavelength Extragalactic Survey of Edge-on Spirals (NHEMESIS)*. IAUSymp, 284, 128–131.
- Holwerda B.W., Kelvin L., Baldry I. et al., 2019. *The frequency of dust lanes in edge-on spiral galaxies identified by Galaxy Zoo in KiDS imaging of GAMA targets*. AJ, 158, 3, 103.
- Hou L.G. & Han J.L., 2015. *Offset between stellar spiral arms and gas arms of the Milky Way*. MNRAS, 454, 1, 626–636.
- Hubble E., 1926. *Extra-galactic nebulae*. ApJ, 64, 321.
- Hubble E.P., 1925. *Cepheids in spiral nebulae*. Observatory, 48, 139.
- Hubble E.P., 1936. *Realm of the Nebulae*. Yale University Press. ISBN 9780300025002.

- Huggins W. & Miller W.A., 1864. *On the Spectra of Some of the Nebulae*. Philos. Trans. R. Soc. Lond., 154, 437–444.
- Humphreys R.M. & Sandage A., 1980. *On the stellar content and structure of the spiral Galaxy M33*. ApJS, 44, 319.
- Israel F.P., Goss W.M. & Allen R.J., 1975. *The giant spiral galaxy M101: radio observations of H II regions in external galaxies. II. Radio continuum emission from the H II regions and the nonthermal disc of M101*. A&A, 40, 421.
- Jafariyazani M., Mobasher B., Hemmati S. et al., 2019. *Spatially resolved properties of galaxies from CANDELS+MUSE: Radial extinction profile and insights on quenching*. ApJ, 887, 2, 204.
- Kashino D., Renzini A., Silverman J.D. et al., 2016. *Hide-and-seek with the fundamental metallicity relation*. ApJ, 823, 2, L24.
- Kashino D., Silverman J.D., Sanders D. et al., 2017. *The FMOS-COSMOS survey of star-forming galaxies at $z \sim 1.6$. IV. Excitation state and chemical enrichment of the interstellar medium*. ApJ, 835, 1, 88.
- Kashino D., Lilly S.J., Renzini A. et al., 2022. *The stellar mass versus stellar metallicity relation of star-forming galaxies at $1.6 < z < 3.0$ and implications for the evolution of the alpha-enhancement*. ApJ, 925, 1, 82.
- Kauffmann G., Heckman T.M., Tremonti C. et al., 2003. *The host galaxies of active galactic nuclei*. MNRAS, 346, 4, 1055–1077.
- Keel W.C., 1993. *Obscuration Effects in Starburst Galactic Nuclei*. ASPC, 35, 498.
- Kennicutt R.C., 1998. *The Global Schmidt Law in Star-forming Galaxies*. ApJ, 498, 2, 541–552.
- Kennicutt R.C., Calzetti D., Walter F. et al., 2007. *Star Formation in NGC 5194 (M51a). II. The Spatially-Resolved Star Formation Law*. ApJ, 671, 1, 333–348.
- Kennicutt R.C. & Evans N.J., 2012. *Star formation in the Milky Way and nearby galaxies*. ARA&A, 50, 531–608.
- Kewley L.J., Dopita M.A., Sutherland R.S. et al., 2001. *Theoretical Modeling of Starburst Galaxies*. ApJ, 556, 1, 121–140.
- Kewley L.J. & Dopita M.A., 2002. *Using Strong Lines to Estimate Abundances in Extragalactic H II Regions and Starburst Galaxies*. ApJS, 142, 1, 35–52.
- Kewley L.J., Geller M.J. & Barton E.J., 2006. *Metallicity and Nuclear Star Formation in Nearby Galaxy Pairs: Evidence for Tidally Induced Gas Flows*. AJ, 131, 4, 2004–2017.

- Kewley L.J. & Ellison S.L., 2008. *Metallicity Calibrations and the Mass-Metallicity Relation for Star-forming Galaxies*. *ApJ*, 681, 2, 1183–1204.
- Kewley L.J., Nicholls D.C. & Sutherland R.S., 2019. *Understanding Galaxy Evolution Through Emission Lines*. *ARA&A*, 57, 1, 511–570.
- Knapen J.H., Beckman J.E., Heller C.H. et al., 1995. *The Central Region in M100: Observations and Modeling*. *ApJ*, 454, 623.
- Kobulnicky H.A. & Zaritsky D., 1999. *Chemical Properties of Star-Forming Emission Line Galaxies at $z = 0.1 - 0.5$* . *ApJ*, 511, 1, 118–135.
- Kollmeier J.A., Zasowski G., Rix H.W. et al., 2017. *SDSS-V: Pioneering Panoptic Spectroscopy*. eprint (arXiv:1711.03234).
- Konidaris N.P., Drory N., Froning C.S. et al., 2020. *SDSS-V local volume mapper instrument: overview and status*. *SPIE*, 11447, 237.
- Kormendy J. & Bender R., 1996. *A Proposed Revision of the Hubble Sequence for Elliptical Galaxies*. *ApJ*, 464, 2, L119–L122.
- Kormendy J. & Kennicutt R.C., 2004. *Secular evolution and the formation of pseudobulges in disk galaxies*. *ARA&A*, 42, 1, 603–683.
- Kormendy J. & Bender R., 2012. *A revised parallel-sequence morphological classification of galaxies: Structure and formation of S0 and spheroidal galaxies*. *ApJS*, 198, 1, 2.
- Kreckel K., Groves B., Schinnerer E. et al., 2013. *Mapping dust through emission and absorption in nearby galaxies*. *ApJ*, 771, 1, A62.
- Krishnarao D., Tremonti C., Fraser-McKelvie A. et al., 2020. *The Effect of Bars on the Ionized ISM: Optical Emission Lines from Milky Way Analogs*. *ApJ*, 898, 2, 116.
- Kroupa P., 2001. *On the variation of the initial mass function*. *MNRAS*, 322, 2, 231–246.
- Kroupa P., 2002. *The initial mass, function of stars: Evidence for uniformity in variable systems*.
- Lacerda E.A.D., Sánchez S.F., Fernandes R.C. et al., 2019. *Galaxies hosting an AGN: a view from the CALIFA survey*. *MNRAS*, 492, 3, 3073–3090.
- Lara-López M.A., Cepa J., Bongiovanni A. et al., 2010. *A fundamental plane for field star-forming galaxies*. *A&A*, 521, 2, 53.
- Larson R.B., 1972. *Effect of Infalling Matter on the Heavy Element Content of a Galaxy*. *Nature Phys. Sci.*, 236, 62, 7–8.

- Larson R.B., 1976. *Models for the Formation of Disc Galaxies*. MNRAS, 176, 1, 31–52.
- Laurent F., Boudon D., Loupiau M. et al., 2018. *ELT HARMONI: image slicer preliminary design*. SPIE, 10702, 335.
- Law D.R., Yan R., Bershady M.A. et al., 2015. *Observing strategy for the SDSS-IV/MaNGA IFU galaxy survey*. AJ, 150, 1, 19.
- Law D.R., Cherinka B., Yan R. et al., 2016. *The Data Reduction Pipeline for the SDSS-IV MaNGA IFU Galaxy Survey*. AJ, 152, 4, 83.
- Law D.R., Westfall K.B., Bershady M.A. et al., 2021. *SDSS-IV MaNGA: Modeling the Spectral Line-spread Function to Subpercent Accuracy*. AJ, 161, 2, 52.
- Leavitt H.S., 1908. *28 New Variable Stars in Harvard Map, Nos. 30 and 33*. Harvard Coll. Obs. Circular, 142, 1.
- Leavitt H.S., 1912. *Periods of 25 Variable Stars in the Small Magellanic Cloud*. Harvard Coll. Obs. Circular, 173, 1.
- Lee S.K., Idzi R., Ferguson H.C. et al., 2009. *Biases and uncertainties in physical parameter estimates of Lyman break galaxies from broadband photometry*. ApJS, 184, 1, 100–132.
- Lee S.K., Ferguson H.C., Somerville R.S. et al., 2010. *Improving the Estimation of Star formation Rates and Stellar Population Ages of High-redshift Galaxies from Broadband Photometry*. ApJ, 725, 2, 1644–1651.
- Lequeux J., Peimbert M., Rayo J.F. et al., 1979. *Chemical composition and evolution of irregular and blue compact galaxies*. A&A, 80, 155L.
- Leroy A.K., Walter F., Sandstrom K. et al., 2013. *Molecular gas and star formation in nearby disk galaxies*. AJ, 146, 2, 19.
- Levi M., Allen L.E., Raichoor A. et al., 2019. *The Dark Energy Spectroscopic Instrument (DESI)*. BAAS, 51, 7, 57.
- Li H., Ge J., Mao S. et al., 2017. *SDSS-IV MaNGA: Variation of the Stellar Initial Mass Function in Spiral and Early-type Galaxies*. ApJ, 838, 2, 77.
- Li H., Wuyts S., Lei H. et al., 2019. *Interpreting the Star Formation–Extinction Relation with MaNGA*. ApJ, 872, 1, 63.
- Lian J., Thomas D. & Maraston C., 2018a. *Modelling the mass-metallicity relation of star-forming galaxies from $z \sim 3.5$ to $z \sim 0$* . MNRAS, 481, 3, 4000–4008.

- Lian J., Thomas D., Maraston C. et al., 2018b. *The mass-metallicity relations for gas and stars in star-forming galaxies: Strong outflow versus variable IMF*. MNRAS, 474, 1, 1143–1164.
- Lilly S.J., Carollo C.M., Pipino A. et al., 2013. *Gas-regulation of galaxies: the evolution of the cosmic sSFR, the metallicity-mass-SFR relation and the stellar content of haloes*. ApJ, 772, 2, 119.
- Lin L., Belfiore F., Pan H.A. et al., 2017. *Resolved star formation and molecular gas properties of green valley galaxies: a first look with ALMA and MaNGA*. ApJ, 851, 1, 18.
- Lintott C., Schawinski K., Bamford S. et al., 2011. *Galaxy Zoo 1: Data release of morphological classifications for nearly 900 000 galaxies*. MNRAS, 410, 1, 166–178.
- Lintott C.J., Schawinski K., Slosar A. et al., 2008. *Galaxy Zoo: Morphologies derived from visual inspection of galaxies from the Sloan Digital Sky Survey*. MNRAS, 389, 3, 1179–1189.
- Loebman S.R., Roskar R., Debattista V.P. et al., 2010. *The Genesis of the Milky Way's Thick Disk via Stellar Migration*. ApJ, 737, 1, 8.
- Lonsdale Persson C.J. & Helou G., 1987. *On the origin of the 40-120 micron emission of galaxy disks: A comparison with H-alpha fluxes*. ApJ, 314, 513.
- López-Sánchez Á.R., 2010. *Massive star formation in Wolf-Rayet galaxies. V: Star formation rates, masses and the importance of galaxy interactions*. A&A, 521, 7, A63.
- Lundmark K., 1926. *A preliminary classification of nebulae*. Arkiv for Matematik, Astronomi och Fysik, 19, 8, 1–5.
- Madau P., Ferguson H.C., Dickinson M.E. et al., 1996. *High-redshift galaxies in the Hubble Deep Field: colour selection and star formation history to $z \sim 4$* . MNRAS, 283, 4, 1388–1404.
- Madau P., Pozzetti L. & Dickinson M., 1998. *The Star Formation History of Field Galaxies*. ApJ, 498, 1, 106–116.
- Madau P. & Dickinson M., 2014. *Cosmic Star-Formation History*. ARA&A, 52, 1, 415–486.
- Maiolino R., Nagao T., Grazian A. et al., 2008. *AMAZE: I. The evolution of the mass-metallicity relation at $z > 3$* . A&A, 488, 2, 463–479.
- Maiolino R. & Mannucci F., 2019. *De Re Metallica: The cosmic chemical evolution of galaxies*. A&A Rev., 27, 1, 187.

- Maiolino R., Cirasuolo M., Afonso J. et al., 2020. *MOONRISE: The Main MOONS GTO Extragalactic Survey*. *Messenger*, 180, 24–29.
- Majewski S.R. & The APOGEE and APOGEE-2 Teams, 2016. *The Apache Point Observatory Galactic Evolution Experiment (APOGEE) and its successor, APOGEE-2*. *Astron. Nachr.*, 337, 8-9, 863–870.
- Mallmann N.D., Riffel R., Storchi-Bergmann T. et al., 2018. *The first 62 AGN observed with SDSS-IV MaNGA - II. Resolved stellar populations*. *MNRAS*, 478, 4, 5491–5504.
- Manning E.M. & Cole A.A., 2018. *From K giants to G dwarfs: Stellar lifetime effects on metallicity distributions derived from red giants*. *MNRAS*, 471, 4, 4194–4205.
- Mannucci F., Cresci G., Maiolino R. et al., 2010. *A fundamental relation between mass, SFR and metallicity in local and high redshift galaxies*. *MNRAS*, 408, 4, 2115–2127.
- Maraston C., Pforr J., Renzini A. et al., 2010. *Star formation rates and masses of $z \sim 2$ galaxies from multicolour photometry*. *MNRAS*, 407, 2, 830–845.
- Martel H., Carles C., Robichaud F. et al., 2018. *Chemical enrichment in isolated barred spiral galaxies*. *MNRAS*, 477, 4, 5367–5381.
- Masters K.L., Nichol R.C., Hoyle B. et al., 2011. *Galaxy Zoo: Bars in disc galaxies*. *MNRAS*, 411, 3, 2026–2034.
- Masters K.L., Lintott C.J., Hart R.E. et al., 2019. *Galaxy Zoo: Unwinding the winding problem - Observations of spiral bulge prominence and arm pitch angles suggest local spiral galaxies are winding*. *MNRAS*, 487, 2, 1808–1820.
- Masters K.L., Krawczyk C., Shamsi S. et al., 2021. *Galaxy Zoo: 3D – Crowdsourced bar, spiral, and foreground star masks for MaNGA target galaxies*. *MNRAS*, 507, 3, 3923–3935.
- Mathewson D.S., van der Kruit P.C. & Brouw W.N., 1972. *A High Resolution Radio Continuum Survey of M51 and NGC 5195 at 1415 MHz*. *A&A*, 17, 468.
- Mathis J.S., Rumpl W. & Nordsieck K.H., 1977. *The size distribution of interstellar grains*. *ApJ*, 217, 425.
- Mathis J.S., 1996. *Dust Models with Tight Abundance Constraints*. *ApJ*, 472, 2, 643–655.
- Matthee J. & Schaye J., 2018. *Star-forming galaxies are predicted to lie on a fundamental plane of mass, star formation rate, and α -enhancement*. *MNRAS*, 479, 1, L34–L39.

- McMillan P.J., 2017. *The mass distribution and gravitational potential of the Milky Way*. MNRAS, 465, 1, 76–94.
- Medling A.M., Cortese L., Croom S.M. et al., 2018. *The SAMI Galaxy Survey: Spatially Resolving the Main Sequence of Star Formation*. MNRAS, 475, 4, 5194–5214.
- Mejía-Narváez A., Sánchez S.F., Lacerda E.A.D. et al., 2020. *The stellar metallicity distribution function of galaxies in the CALIFA survey*. MNRAS, 499, 4, 4838–4853.
- Messier C., 1781. *Catalogue des Nébuleuses et des Amas d’Étoiles*. Connaissance des Temps ou des Mouvements Célestes, page 227.
- Mihalas D. & Binney J., 1981. *Galactic Astronomy*. San Francisco: Freeman, 2nd edition.
- Miller G.E. & Scalo J.M., 1979. *The initial mass function and stellar birthrate in the solar neighborhood*. ApJS, 41, 513.
- Minchev I. & Famaey B., 2010. *A New Mechanism for Radial Migration in Galactic Disks: Spiral-Bar Resonance Overlap*. ApJ, 722, 1, 112–121.
- Minchev I., Anders F., Recio-Blanco A. et al., 2018. *Estimating stellar birth radii and the time evolution of Milky Way’s ISM metallicity gradient*. MNRAS, 481, 2, 1645–1657.
- Minniti D. & Zoccali M., 2008. *The Galactic bulge: A review*. Proc. IAU, 3, S245, 323–332.
- Misselt K.A., Clayton G.C. & Gordon K.D., 1999. *A Reanalysis of the Ultraviolet Extinction from Interstellar Dust in the Large Magellanic Cloud*. ApJ, 515, 1, 128–139.
- Momcheva I., Lee J.C., Ly C. et al., 2013. *Nebular Attenuation in H alpha-selected Star-forming Galaxies at $z=0.8$ from the New H alpha Survey*. AJ, 145, 2, 47.
- Mould J.R., 1978. *Infrared spectroscopy of M dwarfs*. ApJ, 226, 923.
- Moustakas J., Zaritsky D., Brown M. et al., 2011. *Evolution of the Stellar Mass-Metallicity Relation Since $z = 0.75$* . eprint (arXiv:1112.3300).
- Muñoz-Mateos J.C., Gil de Paz A., Boissier S. et al., 2009. *Radial distribution of stars, gas, and dust in SINGS galaxies. II. Derived dust properties*. ApJ, 701, 2, 1965–1991.
- Naab T. & Ostriker J.P., 2017. *Theoretical Challenges in Galaxy Formation*. ARA&A, 55, 1, 59–109.

- Nagao T., Maiolino R. & Marconi A., 2006. *Gas metallicity diagnostics in star-forming galaxies*. *A&A*, 459, 1, 85–101.
- Naim A., Lahav O., Buta R.J. et al., 1995. *A comparative study of morphological classifications of APM galaxies*. *MNRAS*, 274, 4, 1107.
- Nelson E.J., van Dokkum P.G., Momcheva I.G. et al., 2016a. *Spatially-resolved dust maps from Balmer decrements in galaxies at $z \sim 1.4$* . *ApJ*, 817, 1, L9.
- Nelson E.J., van Dokkum P.G., Schreiber N.M.F. et al., 2016b. *Where stars form: inside-out growth and coherent star formation from HST H α maps of 2676 galaxies across the main sequence at $z \sim 1$* . *ApJ*, 828, 1, 27.
- Nicholls D.C., Sutherland R.S., Dopita M.A. et al., 2017. *Abundance scaling in stars, nebulae and galaxies*. *MNRAS*, 466, 6, 4403–4422.
- Noeske K.G., Weiner B.J., Faber S.M. et al., 2007. *Star Formation in AEGIS Field Galaxies since $z = 1.1$: The Dominance of Gradually Declining Star Formation, and the Main Sequence of Star-forming Galaxies*. *ApJ*, 660, 1, L43–L46.
- O’Donnell J.E., 1994. *R_v dependent optical and near-ultraviolet extinction*. *ApJ*, 422, 158.
- Ondrechen M.P., 1985. *Radio continuum observations of the bar and disk of M83*. *AJ*, 90, 1474.
- Onodera M., Carollo C.M., Renzini A. et al., 2015. *The ages, metallicities, and element abundance ratios of massive quenched galaxies at $z \simeq 1.6$* . *ApJ*, 808, 2, 161.
- Oort J.H., Kerr F.J. & Westerhout G., 1958. *Reports on the Progress of Astronomy the Galactic System as a Spiral Nebula*. *MNRAS*, 118, 4, 379–389.
- Osterbrock D.E. & Ferland G.J., 2005. *Astrophysics of Gaseous Nebulae and Active Galactic Nuclei*. University Science Books. ISBN 0935702229.
- Paalvast M. & Brinchmann J., 2017. *Metallicity calibrations of low star-forming galaxies: the influence of a stochastic IMF*. *MNRAS*, 470, 2, 1612–1625.
- Pace Z.J., Tremonti C., Chen Y. et al., 2019. *Resolved and Integrated Stellar Masses in the SDSS-iv/MaNGA Survey. I. PCA Spectral Fitting and Stellar Mass-to-light Ratio Estimates*. *ApJ*, 883, 1, 82.
- Pagel B.E.J. & Patchett B.E., 1975. *Metal Abundances in Nearby Stars and the Chemical History of the Solar Neighbourhood*. *MNRAS*, 172, 1, 13–40.
- Pagel B.E.J., 1989. *The G-Dwarf Problem and Radio-Active Cosmochronology*. In J. E. Beckman & B. E. J. Pagel, editors, *Evolutionary Phenomena in Galaxies*, page 201. Cambridge University Press, Cambridge. ISBN 0521371937.

- Pagel B.E.J., 2009. *Nucleosynthesis and Chemical Evolution of Galaxies*, 2nd ed. Cambridge University Press, Cambridge, 2nd edition. ISBN 0521550610.
- Pannella M., Carilli C.L., Daddi E. et al., 2009. *Star formation and dust obscuration at $z \sim 2$: galaxies at the dawn of downsizing*. *ApJ*, 698, 2, L116–L120.
- Pannella M., Elbaz D., Daddi E. et al., 2015. *GOODS-HERSCHEL: Star formation, dust attenuation, and the FIR-radio correlation on the main sequence of star-forming galaxies up to $z \simeq 4$* . *ApJ*, 807, 2, 141.
- Panther B., Jimenez R., Heavens A.F. et al., 2008. *The Cosmic Evolution of Metallicity from the SDSS Fossil Record*. *MNRAS*, 391, 3, 1117–1126.
- Parsons W., 1850. *Observations on the Nebulae*. *Philosophical Transactions of the Royal Society of London*, 140, 499.
- Peebles M.S., Pogge R.W. & Stanek K.Z., 2009. *Outliers from the Mass–Metallicity Relation II: A Sample of Massive Metal-Poor Galaxies from SDSS*. *ApJ*, 695, 1, 259–267.
- Peimbert M., 1975. *Chemical Composition of Extragalactic Gaseous Nebulae*. *ARA&A*, 13, 1, 113–131.
- Peletier R.F., Valentijn E.A., Moorwood A.F.M. et al., 1995. *The extinction by dust in the outer parts of spiral galaxies*. *A&A*, 300, L1–L4.
- Peng Y.J., Lilly S.J., Kovač K. et al., 2010. *Mass and environment as drivers of galaxy evolution in SDSS and zCOSMOS and the origin of the Schechter function*. *ApJ*, 721, 1, 193–221.
- Pérez E., Cid Fernandes R., González Delgado R.M. et al., 2013. *The evolution of galaxies resolved in space and time: A view of inside-out growth from the califa survey*. *ApJ*, 764, 1, 1.
- Peterken T., Fraser-McKelvie A., Aragón-Salamanca A. et al., 2019a. *Time-slicing spiral galaxies with SDSS-IV MaNGA*. *MNRAS*, 489, 1, 1338–1343.
- Peterken T., Merrifield M., Aragón-Salamanca A. et al., 2020. *SDSS-IV MaNGA: Excavating the fossil record of stellar populations in spiral galaxies*. *MNRAS*, 495, 3, 3387–3402.
- Peterken T., Merrifield M., Aragón-Salamanca A. et al., 2021a. *SDSS-IV MaNGA: When is morphology imprinted on galaxies?* *MNRAS*, 500, 1, L42–L46.
- Peterken T., Aragón-Salamanca A., Merrifield M. et al., 2021b. *Size, shade, or shape? The contribution of galaxies of different types to the star formation history of the Universe from SDSS-IV MaNGA*. *MNRAS*, 502, 3, 3128–3143.

- Peterken T.G., Merrifield M.R., Aragón-Salamanca A. et al., 2019b. *A direct test of density wave theory in a grand-design spiral galaxy*. *Nature*, 3, 2, 178–182.
- Pforr J., Maraston C. & Tonini C., 2012. *Recovering galaxy stellar population properties from broad-band spectral energy distribution fitting*. *MNRAS*, 422, 4, 3285–3326.
- Price S.H., Kriek M., Brammer G.B. et al., 2014. *Direct measurements of dust attenuation in $z \sim 1.5$ star-forming galaxies from 3D-HST: Implications for dust geometry and star formation rates*. *ApJ*, 788, 1, 86.
- Rana N.C. & Basu S., 1990. *Distribution of metals in dwarfs stars in the solar neighbourhood*. *Ap&SS*, 168, 2, 317–330.
- Reid N. & Gilmore G., 1982. *New light on faint stars - II. A photometric study of the low luminosity main sequence*. *MNRAS*, 201, 1, 73–94.
- Rémy-Ruyer A., Madden S.C., Galliano F. et al., 2015. *Linking dust emission to fundamental properties in galaxies: The low-metallicity picture*. *A&A*, 582, A121.
- Renzini A., 1999. *Origin of Bulges*. In R. W. C.M. Carollo, H.C. Ferguson, editor, *The formation of galactic bulges*, page 9. Cambridge University Press, Cambridge.
- Rix H.W. & Rieke M.J., 1993. *Tracing the Stellar Mass in M51*. *ApJ*, 418, 123.
- Roberts W.W., 1969. *Large-Scale Shock Formation in Spiral Galaxies and its Implications on Star Formation*. *ApJ*, 158, 123.
- Rocha-Pinto H.J. & Maciel W.J., 1996. *The metallicity distribution of G dwarfs in the solar neighbourhood*. *MNRAS*, 279, 2, 447–458.
- Rodríguez del Pino B., Aragón-Salamanca A., Chies-Santos A.L. et al., 2017. *OMEGA – OSIRIS Mapping of Emission-line Galaxies in A901/2: II. – Environmental influence on integrated star formation properties and AGN activity*. *MNRAS*, 467, 4, 4200–4217.
- Roškar R., Debattista V.P., Quinn T.R. et al., 2008. *Riding the Spiral Waves: Implications of Stellar Migration for the Properties of Galactic Disks*. *ApJ*, 684, 2, L79–L82.
- Rots H.A., 1975. *Distribution and kinematics of neutral hydrogen in the spiral galaxy M81. II. Analysis*. *A&A*, 45, 43.
- Rowan-Robinson M. & Crawford J., 1989. *Models for infrared emission from IRAS galaxies*. *MNRAS*, 238, 2, 523–558.

- Rowlands K., Dunne L., Dye S. et al., 2014. *Herschel-ATLAS: Properties of dusty massive galaxies at low and high redshifts*. MNRAS, 441, 2, 1017–1039.
- Salim S., Lee J.C., Ly C. et al., 2014. *A Critical Look at the Mass-Metallicity-SFR Relation in the Local Universe. I. An Improved Analysis Framework and Confounding Systematics*. ApJ, 797, 2, 126.
- Salim S., Lee J.C., Davé R. et al., 2015. *On the mass-metallicity-star formation rate relation for galaxies at $z \sim 2$* . ApJ, 808, 1, 25.
- Salim S., Boquien M. & Lee J.C., 2018. *Dust Attenuation Curves in the Local Universe: Demographics and New Laws for Star-forming Galaxies and High-redshift Analogs*. ApJ, 859, 1, 11.
- Salim S. & Narayanan D., 2020. *The Dust Attenuation Law in Galaxies*. ARA&A, 58, 529–575.
- Salpeter E.E., 1955. *The Luminosity Function and Stellar Evolution*. ApJ, 121, 161.
- Sánchez S.F., Kennicutt R.C., Gil de Paz A. et al., 2012. *CALIFA, the Calar Alto Legacy Integral Field Area survey*. A&A, 538, A8.
- Sánchez S.F., Perez E., Sánchez-Blázquez P. et al., 2016a. *Pipe3D, a pipeline to analyze integral field spectroscopy data: I. New fitting philosophy of FIT3D*. Rev. Mex. AA, 52, 1, 21–53.
- Sánchez S.F., Pérez E., Sánchez-Blázquez P. et al., 2016b. *Pipe3D, a pipeline to analyze integral field spectroscopy data: II. Analysis sequence and CALIFA dataproducts*. Rev. Mex. AA, 52, 1, 171–220.
- Sánchez S.F., Avila-Reese V., Hernandez-Toledo H. et al., 2018. *SDSS-IV MaNGA: properties of AGN host galaxies*. Rev. Mex. AA, 54, 1, 217–260.
- Sánchez S.F., 2020. *Spatially-Resolved Spectroscopic Properties of Low-Redshift Star-Forming Galaxies*. ARA&A, 58, 99–155.
- Sánchez Almeida J., 2017. *Gas Accretion and Star Formation Rates*. ASSL, 430, 67–94.
- Sánchez-Blázquez P., Peletier R., Jiménez-Vicente J. et al., 2006. *MILES: A Medium resolution INT Library of Empirical Spectra*. MNRAS, 371, 2, 703–718.
- Sánchez-Menguiano L., Almeida J.S., Muñoz-Tuñón C. et al., 2019. *Characterizing the Local Relation between Star Formation Rate and Gas-phase Metallicity in MaNGA Spiral Galaxies*. ApJ, 882, 1, 9.

- Sandage A., 1961. *The Hubble Atlas of Galaxies*. Carnegie Institute of Washington, Washington.
- Sanders R.L., Shapley A.E., Kriek M. et al., 2018. *The MOSDEF Survey: A Stellar Mass–SFR–Metallicity Relation Exists at $z \sim 2.3$* . ApJ, 858, 2, 99.
- Sanders R.L., Shapley A.E., Jones T. et al., 2021. *The MOSDEF Survey: The Evolution of the Mass–Metallicity Relation from $z = 0$ to $z \sim 3.3$* . ApJ, 914, 1, 19.
- Santini P., Maiolino R., Magnelli B. et al., 2014. *The evolution of the dust and gas content in galaxies*. A&A, 562, 30.
- Schaefer A.L., Croom S.M., Allen J.T. et al., 2017. *The SAMI Galaxy Survey: spatially resolving the environmental quenching of star formation in GAMA galaxies*. MNRAS, 464, 1, 121–142.
- Schaefer A.L., Croom S.M., Scott N. et al., 2019. *The SAMI Galaxy Survey: Observing the environmental quenching of star formation in GAMA groups*. MNRAS, 483, 3, 2851–2870.
- Schlegel D., White M. & Eisenstein D., 2009. *The Baryon Oscillation Spectroscopic Survey: Precision measurements of the absolute cosmic distance scale*. Astro2010: The Astronomy and Astrophysics Decadal Survey, Science White Papers, 314.
- Schmidt M., 1959. *The Rate of Star Formation*. ApJ, 129, 243.
- Schmidt M., 1963. *The Rate of Star Formation. II. The Rate of Formation of Stars of Different Mass*. ApJ, 137, 758.
- Schönrich R. & Binney J., 2009. *Chemical evolution with radial mixing*. MNRAS, 396, 1, 203–222.
- Scudder J.M., Ellison S.L., El Meddah El Idrissi L. et al., 2021. *Conversions between gas-phase metallicities in MaNGA*. MNRAS, 507, 2, 2468–2487.
- Sellgren K., 1984. *The near-infrared continuum emission of visual reflection nebulae*. ApJ, 277, 623.
- Sellwood J.A. & Wilkinson A., 1993. *Dynamics of barred galaxies*. RPPh, 56, 2, 173–256.
- Sellwood J.A. & Binney J.J., 2002. *Radial Mixing in Galactic Discs*. MNRAS, 336, 3, 785–796.
- Shabani F., Grebel E.K., Pasquali A. et al., 2018. *Search For Star Cluster Age Gradients Across Spiral Arms of Three LEGUS Disk Galaxies*. MNRAS, 478, 3, 3590–3604.

- Shepard D., 1968. *A two-dimensional interpolation function for irregularly-spaced data*. Proc. 1968 23rd ACM National Conf., pages 517–524.
- Shields G.A., 1990. *Extragalactic H II regions*. ARA&A, 28, 1, 525–560.
- Shull J.M. & Beckwith S., 1982. *Interstellar Molecular Hydrogen*. ARA&A, 20, 1, 163–190.
- Simard L., Mendel J.T., Patton D.R. et al., 2011. *A Catalog of Bulge+Disk Decompositions and Updated Photometry for 1.12 Million Galaxies in the Sloan Digital Sky Survey*. ApJS, 196, 1, 11.
- Simmons B., Lintott C., Schawinski K. et al., 2013. *Galaxy zoo: Bulgeless galaxies with growing black holes*. MNRAS, 429, 3, 2199–2211.
- Slipher V.M., 1913. *The radial velocity of the Andromeda Nebula*. Lowell Obs. Bull., 1, 56–57.
- Smee S.A., Gunn J.E., Uomoto A. et al., 2013. *The multi-object, fiber-fed spectrographs for the Sloan Digital Sky Survey and the Baryon Oscillation Spectroscopic Survey*. AJ, 146, 2, 32.
- Smethurst R.J., Merrifield M., Lintott C.J. et al., 2019. *Snitch: Seeking a simple, informative star formation history inference tool*. MNRAS, 484, 3, 3590–3603.
- Somerville R.S., Popping G. & Trager S.C., 2015. *Star formation in semi-analytic galaxy formation models with multiphase gas*. MNRAS, 453, 4, 4337–4367.
- Speagle J.S., Steinhardt C.L., Capak P.L. et al., 2014. *A highly consistent framework for the evolution of the star-forming "main sequence" from $z \sim 0-6$* . ApJS, 214, 2, 15.
- Spindler A., Wake D., Belfiore F. et al., 2018. *SDSS-IV MaNGA: The Spatial Distribution of Star Formation and its Dependence on Mass, Structure and Environment*. MNRAS, 476, 1, 580–600.
- Stasińska G., 2002. *The electron temperature in ionized nebulae*. Rev. Mex. AA conf. Ser., 12, 62.
- Stasińska G., 2005. *Biases in abundance derivations for metal-rich nebulae*. A&A, 434, 2, 507–520.
- Steidel C.C., Adelberger K.L., Giavalisco M. et al., 1999. *Lyman Break Galaxies at $z > 4$ and the Evolution of the UV Luminosity Density at High Redshift*. ApJ, 519, 1, 1–17.
- Storchi-Bergmann T., Calzetti D. & Kinney A.L., 1994. *Ultraviolet to near-infrared spectral distributions of star-forming galaxies: Metallicity and age effects*. ApJ, 429, 572.

- Sullivan M., Treyer M.A., Ellis R.S. et al., 2000. *An ultraviolet-selected galaxy redshift survey – II. The physical nature of star formation in an enlarged sample.* MNRAS, 312, 2, 442–464.
- Suzuki T., Kaneda H., Nakagawa T. et al., 2007. *Spatial Distributions of Cold and Warm Interstellar Dust in M101 Resolved with AKARI/Far-Infrared Surveyor (FIS).* PASJ, 59, sp2, S473–S481.
- Tabor M., Merrifield M., Aragón-Salamanca A. et al., 2019. *SDSS-IV MANGA: Full spectroscopic bulge-disc decomposition of MANGA early-type galaxies.* MNRAS, 485, 2, 1546–1558.
- Talbot R.J. & Arnett W.D., 1971. *The Evolution of Galaxies. I. Formulation and Mathematical Behavior of the One-Zone Model.* ApJ, 170, 409.
- Tamburro D., Rix H.W., Walter F. et al., 2008. *Geometrically Derived Timescales for Star Formation in Spiral Galaxies.* AJ, 136, 6, 2872–2885.
- Telford O.G., Dalcanton J.J., Skillman E.D. et al., 2016. *Exploring systematic effects in the relation between stellar mass, gas phase metallicity, and star formation rate.* ApJ, 827, 1, 35.
- Tempel E., Tamm A. & Tenjes P., 2009. *Dust-corrected surface photometry of M31 from the Spitzer far infrared observations.* A&A, 509, A91.
- Thatte N., Tecza M., Schnetler H. et al., 2021. *HARMONI: the ELT’s First-Light Near-infrared and Visible Integral Field Spectrograph.* Messenger, 182, 7–12.
- Tinsley B.M., 1974. *Constraints on models for chemical evolution in the solar neighborhood.* ApJ, 192, 629.
- Tinsley B.M., 1975. *Interpretation of the Stellar Metallicity Distribution.* ApJ, 197, 159.
- Tinsley B.M. & Larson R.B., 1978. *Chemical evolution and the formation of galactic disks.* ApJ, 221, 554.
- Tinsley B.M., 1980. *Evolution of the Stars and Gas in Galaxies.* Fund. Cosmic Phys., 5, 287–388.
- Toomre A., 1977. *Theories of Spiral Structure.* ARA&A, 15, 1, 437–478.
- Tremonti C.A., Heckman T.M., Kauffmann G. et al., 2004. *The Origin of the Mass–Metallicity Relation: Insights from 53,000 Star-Forming Galaxies in the SDSS.* ApJ, 613, 2, 898–913.
- Tress M., Marmol-Queraltó E., Ferreras I. et al., 2018. *SHARDS: Constraints on the dust attenuation law of star-forming galaxies at $z \sim 2$.* MNRAS, 475, 2, 2363–2374.

- Trimble V., 1975. *The origin and abundances of the chemical elements*. *Rev. Mod. Phys.*, 47, 4, 877–976.
- Troncoso P., Maiolino R., Sommariva V. et al., 2014. *Metallicity evolution, metallicity gradients, and gas fractions at $z \sim 3.4$* . *A&A*, 563, 58.
- Trumpler R.J., 1930. *Preliminary results on the distances, dimensions and space distribution of open star clusters*. *LOB*, 420, 154–188.
- Uomoto A., Smee S., Rockosi C. et al., 1999. *The Sloan Digital Sky Survey Spectrographs*. *BAAS*, 195, 8701.
- Urrutia T., Wisotzki L., Kerutt J. et al., 2019. *The MUSE-Wide Survey: Survey description and first data release*. *A&A*, 624, A141.
- Vale Asari N., Cid Fernandes R., Stasińska G. et al., 2007. *The history of star-forming galaxies in the Sloan Digital Sky Survey*. *MNRAS*, 381, 1, 263–279.
- Vale Asari N., Stasinska G., Fernandes R.C. et al., 2009. *The evolution of the mass-metallicity relation in SDSS galaxies uncovered by astropaleontology*. *MNRAS*, 396, 1, 71–75.
- Vallée J.P., 2020. *Statistics on 24 spiral galaxies having different observed arm locations using different arm tracers*. *NewA*, 76.
- van den Bergh S., 1960. *A Preliminary Luminosity Classification of Late-Type Galaxies*. *ApJ*, 131, 215.
- van den Bergh S., 1962. *The frequency of stars with different metal abundances*. *AJ*, 67, 486.
- van den Bergh S., 1976. *A new classification system for galaxies*. *ApJ*, 206, 883.
- Vazdekis A., Sánchez-Blázquez P., Falcón-Barroso J. et al., 2010. *Evolutionary Stellar Population Synthesis with MILES. Part I: The Base Models and a New Line Index System*. *MNRAS*, 404, 1639.
- Vazdekis A., Koleva M., Ricciardelli E. et al., 2016. *UV-extended E-MILES stellar population models: young components in massive early-type galaxies*. *MNRAS*, 463, 4, 3409–3436.
- Veilleux S. & Osterbrock D.E., 1987. *Spectral classification of emission-line galaxies*. *ApJS*, 63, 295–310.
- Wake D.A., Bundy K., Diamond-Stanic A.M. et al., 2017. *The SDSS-IV MaNGA Sample: Design, Optimization, and Usage Considerations*. *AJ*, 154, 3, 86.

- Walborn N.R., Barbá R.H., Brandner W. et al., 1999. *Some Characteristics of Current Star Formation in the 30 Doradus Nebula Revealed by HST/NICMOS*. AJ, 117, 1, 225–237.
- Walterbos R.A.M. & Kennicutt R. C. J., 1988. *An optical study of stars and dust in the Andromeda galaxy*. A&A, 198, 61.
- Weiler K.W. & Sramek R.A., 1988. *Supernovae and Supernova Remnants*. ARA&A, 26, 1, 295–341.
- Weingartner J.C. & Draine B.T., 2001. *Dust Grain Size Distributions and Extinction in the Milky Way, LMC, and SMC*. ApJ, 548, 1, 296–309.
- Westfall K.B., Cappellari M., Bershady M.A. et al., 2019. *The Data Analysis Pipeline for the SDSS-IV MaNGA IFU Galaxy Survey: Overview*. AJ, 158, 6, 231.
- Wheeler J.C., Sneden C. & Truran J.W., 1989. *Abundance Ratios as a Function of Metallicity*. ARA&A, 27, 1, 279–349.
- Whitaker K.E., van Dokkum P.G., Brammer G. et al., 2012. *The star formation mass sequence out to $z = 2.5$* . ApJ, 754, 2, L29.
- White R.E. & Keel W.C., 1992. *Direct measurement of the optical depth in a spiral galaxy*. Nature, 359, 6391, 129–131.
- White R.E., Keel W.C. & Conselice C.J., 2000. *Seeing Galaxies through Thick and Thin. I. Optical Opacity Measures in Overlapping Galaxies*. ApJ, 542, 2, 761–778.
- Wild V., Charlot S., Brinchmann J. et al., 2011. *Empirical determination of the shape of dust attenuation curves in star-forming galaxies*. MNRAS, 417, 3, 1760–1786.
- Wilkinson D.M., Maraston C., Thomas D. et al., 2015. *P-MaNGA: Full spectral fitting and stellar population maps from prototype observations*. MNRAS, 449, 1, 328–360.
- Wilkinson D.M., Maraston C., Goddard D. et al., 2017. *FIREFLY (Fitting Iteratively For Likelihood analysis): A full spectral fitting code*. MNRAS, 472, 4, 4297–4326.
- Willett K.W., Lintott C.J., Bamford S.P. et al., 2013. *Galaxy Zoo 2: detailed morphological classifications for 304,122 galaxies from the Sloan Digital Sky Survey*. MNRAS, 435, 4, 2835–2860.
- Willett K.W., Schawinski K., Simmons B.D. et al., 2015. *Galaxy Zoo: The dependence of the star formation-stellar mass relation on spiral disc morphology*. MNRAS, 449, 1, 820–827.

- Wolf M., 1908. *Die Klassifizierung der kleinen Nebelflecken*. Publikationen des Astrophysikalischen Instituts Koenigstuhl-Heidelberg, 3, 109–112.
- Woolf V.M. & West A.A., 2012. *The M Dwarf Problem in the Galaxy*. MNRAS, 422, 2, 1489–1494.
- Woolf V.M. & Wallerstein G., 2020. *The M dwarf problem: Fe and Ti abundances in a volume-limited sample of M dwarf stars*. MNRAS, 494, 2, 2718–2726.
- Wright E.L., 2006. *A Cosmology Calculator for the World Wide Web*. PASP, 118, 850, 1711–1715.
- Wuyts E., Kurk J., Förster Schreiber N.M. et al., 2014. *A consistent study of metallicity evolution at $0.8 < z < 2.6$* . ApJ, 789, 2, 40.
- Wuyts S., Förster Schreiber N.M., Nelson E.J. et al., 2013. *A candels-3D-hst synergy: Resolved star formation patterns at $0.7 < z < 1.5$* . ApJ, 779, 2, 135.
- Xilouris E.M., Byun Y.I., Kylafis N.D. et al., 1999. *Are spiral galaxies optically thin or thick?* A&A, 344, 868–878.
- Xilouris E.M., Tabatabaei F.S., Boquien M. et al., 2012. *Cool and warm dust emission from M33 (HerM33es)*. A&A, 543, A74.
- Yan R., Bundy K., Law D.R. et al., 2016a. *SDSS-IV MaNGA IFS Galaxy Survey — Survey Design, Execution, and Initial Data Quality*. AJ, 152, 6, 197.
- Yan R., Tremonti C., Bershady M.A. et al., 2016b. *SDSS-IV/MaNGA: Spectrophotometric calibration technique*. AJ, 151, 1, 8.
- Yates R.M., Kauffmann G. & Guo Q., 2012. *The relation between metallicity, stellar mass and star formation in galaxies: an analysis of observational and model data*. MNRAS, 422, 1, 215–231.
- Yates R.M., Henriques B.M.B., Fu J. et al., 2021. *L-GALAXIES 2020: The evolution of radial metallicity profiles and global metallicities in disc galaxies*. MNRAS, 503, 3, 4474–4495.
- Yi S.K., 2008. *The Current Understanding on the UV Upturn*. ASP Conference Series, 392, 3.
- York D.G., Adelman J., Anderson Jr. J.E. et al., 2000. *The Sloan Digital Sky Survey: Technical Summary*. AJ, 120, 3, 1579–1587.
- Zahid H.J., Geller M.J., Kewley L.J. et al., 2013a. *The chemical evolution of star-forming galaxies over the last 11 billion years*. ApJ, 771, 2, 19.

- Zahid H.J., Yates R.M., Kewley L.J. et al., 2013b. *The Observed Relation between Stellar Mass, Dust Extinction and Star Formation Rate in Local Galaxies*. ApJ, 763, 2, 92.
- Zahid H.J., Kashino D., Silverman J.D. et al., 2014a. *The FMOS-COSMOS survey of star-forming galaxies at $z \sim 1.6$. II. The mass-metallicity relation and the dependence on star formation rate and dust extinction*. ApJ, 792, 1, 75.
- Zahid H.J., Dima G.I., Kudritzki R.P. et al., 2014b. *The universal relation of galactic chemical evolution: The origin of the mass-metallicity relation*. ApJ, 791, 2, 130.
- Zahid H.J., Kudritzki R.P., Conroy C. et al., 2017. *Stellar Absorption Line Analysis of Local Star-Forming Galaxies: The Relation Between Stellar Mass, Metallicity, Dust Attenuation and Star Formation Rate*. ApJ, 847, 1, 18.
- Zhang K., Yan R., Bundy K. et al., 2017. *SDSS-IV MaNGA: The impact of diffuse ionized gas on emission-line ratios, interpretation of diagnostic diagrams and gas metallicity measurements*. MNRAS, 466, 3, 3217–3243.
- Zhou S., Li C., Hao C.N. et al., 2021. *Star Formation Histories of Massive Red Spiral Galaxies in the Local Universe*. ApJ, 916, 1, 38.
- Zhou S., Merrifield M. & Aragón-Salamanca A., 2022. *Semi-analytic spectral fitting: simultaneously modelling the mass accumulation and chemical evolution in MaNGA spiral galaxies*. MNRAS, 513, 4, 5446–5464.